The Dissertation Committee for Guanghua Wang Certifies that this is the approved version of the following dissertation:

Two-Point High Repetition Rate Measurement of Temperature and Thermal Dissipation in a Turbulent Non-premixed Jet Flame

Committee:

Noel T. Clemens, Supervisor

Philip L. Varghese, Co-Supervisor

David S. Dolling

Laxminarayan L. Raja

Ofodike A. Ezekoye

Two-Point High Repetition Rate Measurement of Temperature and Thermal Dissipation in a Turbulent Non-premixed Jet Flame

by

Guanghua Wang, B.S; M.S.

Dissertation

Presented to the Faculty of the Graduate School of
The University of Texas at Austin
in Partial Fulfillment
of the Requirements
for the Degree of

Doctor of Philosophy

The University of Texas at Austin
December, 2004

Dedication

To my lovely wife and family

Acknowledgements

It is my pleasure to acknowledge the advice, help, encouragement and contributions of all those talented individuals who made this work possible. I would like to thank my advisors, Dr. Noel Clemens and Dr. Philip Varghese, who patiently supported me through every detail, challenged me more than I can imagine, and inspired me to excellence in research. I would also like to thank Drs. David Dolling, Laxminarayan Raja and Ofodike Ezekoye, for serving on my dissertation committee and challenging me through their classes. The funding from the National Science Foundation is also gratefully acknowledged.

I also thank my (current and former) fellow graduate students Michael Tsurikov, Yongxi Hou, Cherian Idichera, Issac Box, Pablo Bueno, Michael Ryan and Prashanth Kothnur for their numerous insights, suggestions and moral support. Special thanks to Ms. Donna Soward for helping navigate through the university bureaucracy and purchasing all equipments for this project. I thank Mr. Edward Zihlman Jr. for his inputs during the design and fabrication of some of the experimental facility. Many thanks to my lovely wife and my family for all their supports during the journey to pursue the Ph.D degree.

Thanks.

Two-Point High Repetition Rate Measurement of Temperature and Thermal Dissipation in a Turbulent Non-premixed Jet Flame

Publication No._____________

Guanghua Wang, Ph.D.
The University of Texas at Austin, 2004

Supervisors: Noel T. Clemens and Philip L. Varghese

A high-repetition rate (10 kHz) laser Rayleigh scattering facility was developed and used to study the temperature fluctuations, power spectra, gradients and thermal dissipation rate characteristics of a nonpremixed turbulent jet flame at a Reynolds number of 15,200. The flame studied here is similar to the Turbulent Nonpremixed Flame Workshop simple jet flame (DLR_A flame). The radial temperature gradient was measured by a two-point technique, whereas the axial gradient was inferred from temperature time-series measurements combined with Taylor's hypothesis.

Resolution and noise can greatly affect such measurements, and thus a model is proposed to account for the effects of resolution, noise, filtering and data processing on the measured dissipation. The model clearly shows the interplay between resolution and noise, and that noise will create an apparent dissipation (or bias), which will be more significant at high spatial resolution. Techniques to correct the measured mean dissipation for this bias are discussed for the two-point time-series thermal dissipation measurements reported here. A general technique to estimate the noise level for scalar dissipation measurements is also proposed.

The resulting two-point time-resolved measurements in a turbulent flame show that the temperature power spectra along the jet centerline exhibit only a small inertial subrange due to the low local Reynolds number of the flow ($Re_{\delta} \sim 2{,}500$), although a larger inertial subrange is present in the spectra at off-centerline locations. Furthermore, the power spectra collapse in the dissipation range when the frequencies are normalized by the Batchelor frequency. Probability density functions of the thermal dissipation are shown to deviate from lognormal in the low-dissipation portion of the distribution when only one component of the gradient is used; however, nearly lognormal distributions are obtained along the centerline when both axial and radial components are included. A procedure is developed for correcting the thermal dissipation for the apparent dissipation introduced by noise. This procedure uses redundant measurements, either temporally or spatially, to quantify the noise contribution on the mean dissipation. This analysis shows that noise has a dominating effect on the dissipation as the apparent dissipation can be as large as five times the actual dissipation on centerline. The corrected dissipation measurements show that the radial profile of the mean thermal dissipation exhibits a peak off centerline at all downstream locations. These results indicate that the underlying turbulence, as inferred from the temperature fluctuations, is in large part similar to that of

nonreacting jet flows, provided the Reynolds number is properly modified to account for heat release.

Table of Contents

List of Tables xii

List of Figures xiii

Nomenclature xxi

Chapter 1 Introduction 1
  1.1 Motivations 1
  1.2 Mixture fraction and its dissipation 3
  1.3 Experimental measurements of mixture fraction dissipation 5
    1.3.1 Multiscalar line imaging 6
    1.3.2 Two-Dimensional imaging 9
  1.4 Thermal dissipation 14
  1.5 Issues to resolve 16
    1.5.1 Scales of turbulence 17
    1.5.2 Noise effects 27
  1.6 Scope of the current investigation 31

Chapter 2 Experimental setup and data reduction 34
  2.1 Experimental setup 34
    2.1.1 Particle-free co-flowing jet flame facility 36
    2.1.2 Laser system 45
    2.1.3 Low f-number optical collection system 51
    2.1.4 Photo-detectors 59
    2.1.5 Multi-channel data acquisition (DAQ) system 63
    2.1.6 LabVIEW programs 64
  2.2 Data reduction 69
    2.2.1 Laser Rayleigh thermometry 69
    2.2.2 Gradient and dissipation calculation 71

Chapter 3. Scalar dissipation measurement model 73
  3.1 Introduction 73
  3.2 Theoretical modeling 76
    3.2.1 Measurement sub-model 78
    3.2.2 Post-Processing filters 80
    3.2.3 Combined effects of resolution and noise 82
    3.2.4 Gradient calculation 84
  3.3 Apparent dissipation (Noise-bias) 87
    3.3.1 Case 1 90
    3.3.2 Case 2 91
    3.3.3 Case 3 91
    3.3.4 Error relations for current study 92
  3.4 Apparent dissipation correction techniques 93
    3.4.1 Redundant measurement 93
    3.4.2 Pixel-Binning 94
    3.4.3 Power Spectra Density (PSD) correction technique 96
  3.5 Apparent dissipation estimation techniques 101
    3.5.1 Apparent noise estimation for mixture fraction measurement by Rayleigh scattering in non-reacting flows 102
    3.5.2 Thermal dissipation measurement by shot-noise limited Rayleigh scattering in reacting flows 105
  3.6 Summary 107

Chapter 4. Time-series temperature and thermal dissipation measurement in a non-premixed turbulent jet flame 109
  4.1 Introduction 109
  4.2 Thermal diffusivity 110
  4.3 Resolution estimation 113
  4.4 Single point results 119
    4.4.1 Mean and fluctuation temperature 119

4.4.2 Temperature autocorrelation function and turbulent time scales 122
4.4.3 Outer-scale estimates of the Batchelor scale 126
4.4.4 Higher order moments 128
4.4.5 Temperature Probability Density Function (PDF) 131
4.4.6 Temperature Power Spectral Density (PSD) 132
4.5 Two-point results 138
4.5.1 Joint PDF of T_1 and T_2 140
4.5.2 PDF of temperature gradients 142
4.5.3 PDF of thermal dissipation 143
4.5.4 Joint PDF of temperature and thermal dissipation 145
4.5.5 Correction for the apparent dissipation 148
4.5.6 Effects of the thermal diffusivity 160
4.6 Summary 164

Chapter 5 Conclusions 168
5.1 Development of the high repetition rate laser Rayleigh system 168
5.2 Scalar dissipation measurement model 168
5.3 Two-point high repetition temperature and thermal dissipation measurement in a non-premixed turbulent jet flame 171
5.4 Future work 174

References 177

Vita 186

List of Tables

Table 1.1. Summary of C_1 for $\lambda_K = L\, C_1(U,L) \left[Re(U,L)\right]^{-3/4}$ in nonreacting jet flow. $r_{1/2}$ is the half width half maximum (HWHM) width of the jet and l is the integral length scale 20

Table 1.2. Summary of C_1 used in the nonreacting circular jet flow experiments. 20

Table 1.3. Summary of Λ used in the nonreacting jet flow experiments. 22

Table 2.1 Fuel meter summary 44

Table 2.2 Component lenses of the detection system (Model # from Melles-Griot) 51

Table 2.3 Summary of R636-10 and H7422-40 PMT characteristics 61

Table 2.4 Specifications for NI-PCI-MIO-16E-1 A/D card 64

Table 3.1 Comparison of differentiation stencils 85

Table 4.1 Jet flame conditions and estimates of resolution requirements. (Velocity data from Schneider et al. (2003), U_{C0} = 51.6 m/s is the mean jet exit centerline velocity which is different from the mean jet exit velocity U_0; temperature data from TNF workshop database) 117

List of Figures

Figure 1.1 Round jet with coflow coordinates 19

Figure 1.2 Power spectra of velocity fluctuations in high Reynolds number turbulent flows. $\kappa_{v,1}$ is the wavenumber for $\lambda_{v,1}$(the *inner viscous scale*, Dimotakis, 2000), κ_η is the wavenumber for Kolmogorov scale λ_η 23

Figure 1.3 Effect of probe spatial resolution on measurements of scalar dissipation in the far field of a turbulent circular jet. θ is the measured scalar. (Fig. 2 in Mi and Nathan, 2003) 25

Figure 1.4 The local Reynolds number as a function of axial distance (*x/d*) for nonreacting and reacting jets with Re_d = 10,000. (Fig. 5 in Muniz and Mungal, 2001) 26

Figure 1.5 Comparing of the measured and corrected radial profiles of scalar dissipation of local CO_2 mass fraction (Fig. 6 in Ferrao et al., 2000).. 30

Figure 2.1 Experimental setup (a) experimental setup illustration, (b) experimental instruments and hardware illustration 35

Figure 2.2 Experimental instruments and system picture 36

Figure 2.3 Particle-free coflow jet flow facility.. 37

Figure 2.4 Scanning of the hot film across the test section exit plane 38

Figure 2.5 Hot film calibration diagram... 39

Figure 2.6 Hot film calibration result.. 41

Figure 2.7 Mean axial velocity of the jet coflow facility...................................... 42

Figure 2.8 Turbulence intensity (%) of the jet coflow velocity 43

Figure 2.9 Coflow velocity PDF 43

Figure 2.10 Fuel supply and metering system.. 44

Figure 2.11 Beam focal spot diameter and Rayleigh range calculation for M^2 = 25 46

Figure 2.12 (a) Illustration of imaging Corona laser beam, (b) Experimental setup for imaging Corona laser beam... 47

Figure 2.13 Images of Corrona laser beam by Cryocam camera, from top to bottom (a) f/2.8, (b)f/5.6 and (c) f/11 48

Figure 2.14 Corona laser beam thickness (a) e^2 (b) FWHM................................ 49

Figure 2.15 Corona laser beam thickness (a) e^2 (b) FWHM................................ 50

Figure 2.16 Ideal objects array and corresponding images (units are in mm) for the designed collection optical system 52

Figure 2.17 Spot diagrams (a) before, and (b) after, spherical aberration correction.. 53

Figure 2.18 Two-point setup using 50/50 beam cube splitter.............................. 56

Figure 2.19 Setup of the collection optics... 57

Figure 2.20 Verification of two-point resolution by the scanning wire technique 57

Figure 2.21 Two-point setup using two separate channels 58

Figure 2.22 Multi-channel PMT power supply implementation.......................... 62

Figure 2.23 LabVIEW VI for data acquisition (DAQ), motion control, flow rate monitoring programs 65

Figure 2.24 LabVIEW GUI for multi-channel PMT power supply control program 67

Figure 2.25 LabView GUI for data analysis 68

Figure 3.1 System model from scalar field $o(x)$ to the calculated dissipation $\chi(x)$ 76

Figure 3.2 Dissipation system resolution and noise modeling............................. 78

Figure 3.3 Modeling of the post-processing filter.. 80

Figure 3.4 Simplified model for post-processing filter that uses the “apparent LSF” to account for noise effects.. 81

Figure 3.5 Model of $h_p[n]$ for the pixel binning effect 81

Figure 3.6 Illustration of correlated effects of resolution and noise in the scalar dissipation measurement 83

Figure 3.7 Effect of gradient stencil on the computation of the temperature gradient *PSD*. $PSD_T(f)$ and $PSD_{\partial T/\partial t}(f)$ are the *PSD*s of the temperature and temperature gradient respectively. The black curve was computed without differentiation of the data, whereas the red and blue curves were differenced. Data were acquired in a turbulent nonpremixed jet flame, Re_d=15,200, *x*/*d*=80................. 86

Figure 3.8 Illustration of the differentiation stencil 88

Figure 3.9 Illustration of the pixel-binning in 1-D imaging experiments. (*i, j*) is the pixel index, *i* is the binned or super pixel index and *j* is the index of the physical pixel within the super-pixel *i* 94

Figure 3.10 Comparing measured and corrected PSDs.. 98

Figure 3.11 Comparing measured and corrected autocorrelation functions 99

Figure 3.12 Centerline absolute error ratio $\varepsilon_{a,\xi_C} / \varepsilon_{a,\xi_{air}}$ in non-reacting ethylene jet. 104

Figure 4.1 Thermal diffusivity $\alpha_C = \alpha_{C0}(T_C/T_0)^{1.723}$, where α_{C0} is the thermal diffusivity at T_0 of the mixture composition at T_C. (a) fuel rich and fuel lean sides, (b) in mixture fraction space.......................... 111

Figure 4.2 Thermal diffusivity $\alpha_C = \alpha_0(T_C/T_0)^{1.42}$, where α_0 is the thermal diffusivity of the fuel combination at T_0 112

Figure 4.3 Scaling laws for DLA A flame from Schneider et al. (2003), (a) mean centerline velocity, (b) FWHM of velocity profile.............. 116

Figure 4.4 Variation of estimated local Reynolds number along jet flame centerline 118

Figure 4.5 Variation of estimated local Batchelor length and time scales along the jet flame centerline 118

Figure 4.6 Radial profiles of (a) mean and (b) rms temperature at three different axial stations (*x/d* = 40, 60, 80). Data from TNF workshop data base (SANDIA and DLR datasets) were shown for comparison.. 120

Figure 4.7 Axial profiles of (a) mean and (b) *rms* temperature at three different axial stations (*x/d* = 40, 60, 80). Data from TNF workshop data base (SANDIA and DLR datasets) were shown for comparison.. 121

Figure 4.8 Auto-correlation functions at the jet flame centerline 122

Figure 4.9 Integral time scale for at the jet flame centerline 123

Figure 4.10 Comparison of the outer, integral and Batchelor time scales along the jet flame centerline 124

Figure 4.11 Ratio of outer to integral length scale along the jet flame centerline 125

Figure 4.12 Comparison of the Batchelor scale estimated from the integral length scale and from non-reacting jet scaling laws in section 4.3 127

Figure 4.13 Radial profiles of skewness at *x/d* = 40, 60 and 80. The dotted line indicates the skewness value for a Gaussian distribution which is 0. 128

Figure 4.14 Radial profiles of kurtosis at *x/d* = 40, 60 and 80. The dotted line indicates the kurtosis value for a Gaussian distribution which is 3. 129

Figure 4.15 Centerline Skewness and Kurtosis for *x/d* = 40 to 80. The dotted line indicates the skewness and kurtosis values for a Gaussian distribution which are 0 and 3 respectively. 130

Figure 4.16 Possibility density functions of temperature at the jet flame centerline 131

Figure 4.17 Normalized fluctuating temperature power spectra at the jet flame centerline (a) without noise floor correction; (b) after noise floor correction (except for *x/d* < 55) 132

Figure 4.18 Normalized fluctuating temperature power spectra at the jet flame centerline (noise effects were corrected except for *x/d* < 55) (a) normalized by the integral time scale τ_I ; (b) normalized by the outer time scale τ_δ 135

Figure 4.19 Fluctuating temperature power spectra along ray r/δ = 0.4 (corrected except at *x/d* = 40) 136

Figure 4.20 Fluctuating temperature power spectra at *x/d* = 80 and different radial locations, all corrected. 137

Figure 4.21 Representative two-channel temperature and radial thermal dissipation rate time-series at the jet flame centerline at *x/d* = 40, 60 and 80. Dash-lines are mean values of temperature and radial thermal dissipation rate. 139

Figure 4.22 Joint PDF(T_1, T_2) at the jet flame centerline 141

Figure 4.23 Probability density functions (PDFs) of the normalized radial temperature gradients along the jet centerline............................... 142

Figure 4.24 Probability density functions of thermal dissipation. (a) log-log plot showing effect of using radial and axial components to compute dissipation, (b) variation with radial location at *x/d* = 80, (c) variation with radial location at *x/d* = 40. 144

Figure 4.25 Joint PDF of temperature and radial thermal dissipation rate at the jet flame centerline 146

Figure 4.26 Effects of varying laser energy on the measured mean-squared gradient 149

Figure 4.27 Variation of the measured mean-squared gradient, apparent mean-squared gradient by two-point redundant technique, apparent mean-squared gradient by power spectra technique and corrected mean-squared gradient (radial component only) along the jet flame centerline. 150

Figure 4.28 Variation of the measured mean squared gradient, apparent mean-squared gradient by two-point redundant technique, apparent mean-squared gradient by power spectra technique and corrected mean-squared gradient (radial component only) at (a) *x/d* = 60 and (b) *x/d* = 80 151

Figure 4.29 Comparing the estimated apparent mean-squared gradient from shot-noise limited noise assumptions with measured ones from the two-point redundant technique along the jet flame centerline. 152

Figure 4.30 Comparing radial profiles of estimated apparent mean-squared gradient from shot-noise limited noise assumptions with measured ones from the two-point redundant technique and power spectra technique at (a) *x/d* = 40, (b) *x/d* = 60 and (b) *x/d* = 80 154

Figure 4.31 Comparing radial profiles of (a) measured (uncorrected) mean-squared gradient; (b) corrected mean-squared gradient at *x/d* = 40, 60 and 80 156

Figure 4.32 Radial profiles of the (a) measured, (b) corrected mean-squared gradient terms normalized by the $\left(T_{rms}/\lambda_B\right)^2$ at x/d = 40, 60 and 80 160
Figure 4.33 Effects of the thermal diffusivity on the measured radial mean scalar dissipation rate 162

Nomenclature

Roman symbols

A	Constant for $\sigma_f / \sigma_{air} - 1$
B	Background scattering and luminosity
C_1	Constant of proportionality for Kolmogorov scale
C_2	Constant of proportionality for mean centerline velocity
C_3	Constant of proportionality for FWHM of velocity profile
C_{R1}	Constant of proportionality for Rayleigh scattering signal
C_{R2}	Constant of proportionality for Rayleigh scattering signal
d	Jet exit diameter
d_b	Laser beam diameter
$d*$	Round jet source diameter
e	Electron charge
D	Mass diffusivity
f_s	Sampling frequency
f_c	Cut-off frequency
G	PMT gain
g	Gradient
I_d	Dark current of PMT
I_k	Total current of PMT photo cathode
I_R	Rayleigh scattering light intensity
Is	Signal current of PMT
h_g	Digital filter for $d()/dx$
h_p	Post processing filter
i	Image / blurred image / pixel index / species
j	Pixel index

k	Boatman constant / Calibration constant
l	Integral length scale
L	Characteristic length scale of flow / Linear operator
m	Number of photons
M^2	Multi-mode property of laser beam
n	noise / number density
N_0	Loschmidt's number
o	Object / Scalar concentration profile
p	Pressure
Q	Volume flow rate
Q_0	Jet source volume flow rate
r	Jet radial coordinate
R	Auto-correlation function
R_L	Load resistor
Re_d	Jet Reynolds number based on exit conditions
Re_δ	Jet Reynolds number based on velocity FWHM
Re_l	Fluctuation Reynolds number
S	Signal
Sc	Schmidt number
S_R	Measured Rayleigh scattering signal
T	Temperature
t	Time
u	Velocity in x direction
u_{rms}	*rms* of velocity fluctuations in x direction
$\overline{U}\ or\ \langle U \rangle$	Mean velocity in x direction
$\overline{U}_C\ or\ \langle U_C \rangle$	Mean speed on the centerline of a jet in x direction
U_o	Bulk jet exit speed

U_∞	Coflow speed
v	Velocity in y direction
$\vec{V}$	Velocity vector
$\dot{w}_i$	Rate of production by chemical reaction of species i
x_o	Virtual origin of axisymmetric jet
x_i	Mole fraction of species i
Y_i	Mass fraction of species i

Greek symbols

α	Thermal diffusivity
β	Conserved scalar based on total enthalpy
χ	Instantaneous scalar / mixture fraction dissipation
$\bar{\chi}\ or \left\langle \chi \right\rangle$	Mean scalar / mixture fraction dissipation
χ_T	Instantaneous thermal dissipation
$\bar{\chi}_T\ or \left\langle \chi_T \right\rangle$	Mean thermal dissipation
Δf	Detection bandwidth
Δx	Probe separation in x direction
Δr	Probe separation in r direction
δ	Characteristic outer scale / Velocity FWHM of axisymmetric turbulent jet / secondary emission ratio of PMT
$\delta_{0.05}$	5% velocity full width of axisymmetric turbulent jet
ε	Instantaneous kinetic energy dissipation
$\bar{\varepsilon}\ or \left\langle \varepsilon \right\rangle$	Mean kinetic energy dissipation rate
ε_a	Absolute error
ε_r	Relative error

η	Collection optics efficiency
η_{det}	Quantum efficiency of PMT
κ	Wavenumber
λ	Laser wavelength
λ_K	Kolmogorov scale
λ_B	Batchelor scale
λ_D	Strain-limited mass diffusion scale
λ_ν	Strain-limited vorticity diffusion scale
λ_T	Taylor microscale
Λ	Constant of proportionality for diffusion scales
μ	Mean number of photons
μ_0	Index of refraction of the gas at STP
ν	Kinematic viscosity
ρ	Density
ρ_∞	Coflow density
ρ_0	Jet exit density
σ	Rayleigh scattering cross section / Standard deviation
σ_{eff}	Effective Rayleigh scattering cross section
τ_B	Batchelor time scale
τ_δ	Outer time scale
τ_I	Integral time scale
Ω	Solid angle
ξ	Conserved scalar / mixture fraction

Abbreviations

CMC	Conditional Moment Closure
DAQ	Data-Acquisition
DC	Dark count
DSNR	Difference Signal to Noise Ratio
FWHM	Full Width Half Maximum
HEPA	High Efficiency Particulate Arrestor
LSA	Longitudinal Spherical Aberration
LSF	Line Spread Function
LSF_a	Apparent Line Spread Function
MW	Molecular Weight of species
NF	Noise Floor
PDF	Possibility Density Function
PMT	Photo-Multiplier Tube
PSF	Point Spread Function
PSD	Power Spectra Density
SNR	Signal to Noise Ratio
TNR	Turbulence to Noise Ratio
VI	Virtual Interface of LabVIEW

Superscripts and Subscripts

0	Jet exit condition
i	Blurred image / quantity
m	Measured quantity
*	Normalized quantity
∞	Coflow quantities

Chapter 1 Introduction

1.1 MOTIVATIONS

Turbulent combustion, which is one of the most important topics in combustion science, has been investigated for centuries. Research in this area is partly motivated by the fact that virtually all combustion takes place in systems that exhibit substantial turbulence. Turbulence itself is undoubtedly one of the most difficult problems in nonlinear physics, and combustion brings complex chemical kinetics and strong non-linear coupling of the turbulence and chemistry, which makes the problem even harder. With advances in turbulence research, improved laser diagnostics techniques and computational capabilities, our understanding of turbulent combustion is improving all the time. However, the problem of turbulence is still the most serious bottleneck between combustion science and its application (Bray, 1996). Realizing such difficulties, combustion technology development has traditionally resorted to empirical methods. As noted by Williams (1992), the technology often forges ahead by trial and error or makes progress fortuitously by application of scientific misconception. In recent years advanced computational modeling techniques are playing a larger role in combustor design but these models are still limited by a lack of understanding of fundamental physics and limited experimental data that are of sufficient quality for validation.

A particularly challenging issue for modelers is the turbulence-chemistry interaction in non-premixed combustion. Turbulence-chemistry interactions arise from the fact that in the non-premixed flame, fuel and oxidizer have to be mixed at the molecular level before they can react and the flame is mainly controlled by turbulent mixing occurring between the fuel and oxidizer. In most combustion systems, chemical reaction rates cannot be evaluated from spatial or temporal mean values and are strongly coupled to molecular diffusion at the smallest scales of turbulence. Furthermore, the heat release associated with combustion affects the turbulent flow, both from variations in the viscosity, density and from the effects of local dilatation (Bilger, 2000).

Detailed measurements of mean and fluctuating scalars, such as species mass fractions and temperature have been critical to developing an improved understanding of the physics of turbulent nonpremixed flames as discussed by Peters (1984), Bilger (1976, 1988), Dibble et al. (1987), Masri et al. (1996) and Stricker (2002). Bilger (1976) identified the scalar dissipation rate as one of the most important governing parameters in turbulent premixed flames. The scalar dissipation rate, which is defined more rigorously below, is a measure of the rate at which scalar gradients are removed by diffusion, and is often called the "mixing rate" because it describes how rapidly fuel and oxidizer can be intertwined on a molecular level. The scalar dissipation rate is a key concept of turbulent combustion and it appears, directly or indirectly, in most tools used to model turbulent flames. As will be shown below, the reaction rate is directly proportional to the scalar dissipation rate in the fast-chemistry limit and Peters (1984) showed that it is an important parameter that describes the degree of non-equilibrium for finite-rate chemistry conditions.

1.2 MIXTURE FRACTION AND ITS DISSIPATION

In order to see the importance of the scalar dissipation to turbulent combustion, it is instructive to consider the development of the equations for reaction rate as first formulated by Bilger (1976) for the special case of infinitely fast chemistry. Based on the Shvab-Zeldovich assumptions, Bilger (1976) showed that the transport equation of species *i* is

$$\rho \frac{\partial Y_i}{\partial t} + \rho \vec{V} \cdot \nabla Y_i - \nabla \cdot \left(\rho D \nabla Y_i \right) = \dot{w}_i , \qquad (1.1)$$

where Y_i and $\dot{w}_i$ are the mass fraction and rate of production by chemical reaction of species *i*, ρ is the mass density, $\vec{V}$ is the velocity vector and *D* is the mass diffusivity.

Under the assumption of fast chemistry and equal diffusivities, the species composition can be assumed to be a function of the mixture fraction only, i.e., there exists a state relationship between the mass fraction Y_i and the mixture fraction ξ, as follows:

$$Y_i = Y_i(\xi) . \qquad (1.2)$$

The mixture fraction is an important conserved scalar, which can be interpreted as

$$\xi = \frac{Mass\ of\ material\ originating\ in\ the\ fuel\ stream}{Mass\ of\ mixture} . \qquad (1.3)$$

Based on the state relationship (1.2), the spatial and temporal derivatives of the mass fraction can be related to the corresponding mixture fraction derivatives as

$$\nabla Y_i = \frac{dY_i}{d\xi} \nabla \xi , \qquad (1.4)$$

$$\frac{\partial Y_i}{\partial t} = \frac{dY_i}{d\xi}\frac{\partial \xi}{\partial t}, \tag{1.5}$$

Substituting Eqn. (1.4) and (1.5) into (1.1),

$$\rho\frac{dY_i}{d\xi}\frac{\partial \xi}{\partial t} + \rho\vec{V}\cdot\frac{dY_i}{d\xi}\nabla\xi - \nabla\cdot\left(\rho D\frac{dY_i}{d\xi}\nabla\xi\right) = \dot{w}_i\,. \tag{1.6}$$

After rearranging Eqn. (1.6), it can be shown that

$$\frac{dY_i}{d\xi}\left[\rho\frac{\partial \xi}{\partial t} + \rho\vec{V}\cdot\nabla\xi - \nabla\cdot\left(\rho D\nabla\xi\right)\right] - \rho D\nabla\xi\cdot\nabla\left(\frac{dY_i}{d\xi}\right) = \dot{w}_i\,. \tag{1.7}$$

Since the mixture fraction is a conserved scalar quantity, and it obeys the conserved scalar transport equation

$$L(\xi) = 0\,, \tag{1.8}$$

where L is a linear operator given by

$$L = \rho\frac{\partial}{\partial t} + \rho\vec{V}\cdot\nabla - \nabla\cdot\left(\rho D\nabla\right). \tag{1.9}$$

Therefore, the bracketed term in (1.7) is zero and thus it reduces to

$$\dot{w}_i = -\rho D\nabla\xi\cdot\nabla\left(\frac{dY_i}{d\xi}\right). \tag{1.10}$$

Using the state relationship (1.2) again, Eqn (1.10) can be written as

$$\dot{w}_i = -\rho\frac{d^2Y_i}{d\xi^2}D\left(\nabla\xi\cdot\nabla\xi\right). \tag{1.11}$$

Eqn. (1.11) can be alternatively written as

$$\dot{w}_i = -\rho\frac{d^2Y_i}{d\xi^2}\frac{\chi}{2}\,. \tag{1.12}$$

where χ is the scalar dissipation rate defined as

$$\chi = 2D(\nabla\xi \cdot \nabla\xi) = 2D|\nabla\xi|^2 . \qquad (1.13)$$

Equation (1.12) is an important result because it shows that the mean reaction rate is proportional to the scalar dissipation rate in the fast chemistry limit. This gives an example of the importance of the scalar dissipation rate for fast-chemistry combustion; however, the scalar dissipation is even more important for finite-rate chemistry conditions because it quantifies the degree of non-equilibrium of the chemical reactions. More specifically, for finite-rate chemistry, a state relationship can be defined, but it is a function of both mixture fraction and its dissipation, e.g. $Y_i = Y_i(\xi, \chi)$ (Vervisch and Poinsot, 1998). Most combustion models, such as laminar flamelet theory and conditional moment closure (CMC) methods, use this state relationship.

In flamelet theory, the turbulent flame is modeled as being composed of a large number of unsteady laminar flames that are thinner than the characteristic vortical scales in the flow. Such a model is argued to occur when the width of the flame in mixture fraction space is thinner than the characteristic mixture fraction fluctuations in the flow. In the flamelet model the flame structure is fundamentally related to the value of mixture fraction ξ at stoichiometric conditions and the rate of its dissipation. For the CMC approach, information on the mean scalar dissipation conditioned on the mixture fraction is vital.

1.3 EXPERIMENTAL MEASUREMENTS OF MIXTURE FRACTION DISSIPATION

Owing to its importance in turbulence modeling, turbulent combustion theory and numerical modeling, measurements of mixture fraction dissipation in turbulent nonpremixed flames have received a lot of attention in recent years.

Barlow and Karpetis (2002) reviewed recent mixture fraction dissipation measurements. They divided these measurements into three categories: (1) line Raman/Rayleigh measurements in hydrogen flames, e.g. Nandula et al. (1994), Brockhinke et al. (1996, 2000), Chen and Mansour (1997); (2) line Raman/Rayleigh measurements in methane flames, e.g. Karpetis and Barlow (2002); (3) 2-D imaging experiments in jet flames, e.g. Starner et al. (1997), Kelman and Masri (1997), Fielding et al. (1998), Frank et al. (2002) and Sutton and Driscoll (2002). In the following section, the above work will be reviewed in more detail and some recent experimental measurements in reacting flows will also be included.

1.3.1 Multiscalar line imaging

Multiscalar line imaging, e.g. simultaneous Raman, Rayleigh, and LIF techniques, has been applied to obtain single-shot measurements of the 1-D component of the scalar dissipation in turbulent hydrogen jet flames by Nandula et al. (1994), Brockhinke et al. (1996, 2000) and Chen and Mansour (1997). Hydrogen flames were used because of their relatively simple chemistry and low interference from flame luminosity.

Nandula et al. (1994) used Raman scattering induced by a pulsed KrF excimer laser to obtain spatially and temporally resolved, simultaneous multiple point measurements of species concentrations and temperatures in turbulent nonpremixed H_2-air flames. The spatial resolution they estimated for x/d = 33 and Re = 15,600, is about 5.4 - 9.8 λ_K (λ_K is the Batchelor scale which will be defined later). They concluded that 75 - 90% of the total dissipation in the radial direction could be captured. The radial profiles (averaged over 200 shots) of mean scalar dissipation at x/d = 10 and 33 for Re = 5,000 and 10,000 scaled approximately as ξ_{rms}^3, which is close to the assumptions used in the $k-\varepsilon$ model. The PDFs of scalar dissipation were log-normally distributed and negatively skewed. When compared to laminar flamelet model calculations, the measured scalar dissipation agreed well near stoichiometric conditions and was smaller in the fuel rich region. However, the estimated strain rates of 50 - 1000s^{-1} were significantly lower than the corresponding extinction value of 12,000s^{-1}.

Brockhinke et al. (1996, 2000) used single- and double-pulse 1-D Raman/Rayleigh imaging to measure quantitative profiles of major species concentrations and temperature in the upstream region of a turbulent H_2/air jet diffusion flame near the lift-off position. In the double pulse quasi-2D experiments, adjacent one-dimensional traces (0.3mm in diameter and separated by 1mm) were monitored. Temperature gradients and scalar dissipation rates were determined simultaneously in two perpendicular directions. The measurement was mainly for the near field of the flame, i.e. x/d = 2 to 30. They used Nandula et al's (1994) resolution criterion: *a resolution of 10 times the Kolmogorov scale is enough to capture the scalar dissipation*. The estimated Kolmogorov scale was about 0.05 mm, and the separation of the two beams corresponded to about 20 times the Kolmogorov scale. The mean scalar dissipation rate at x/d = 11 was calculated from 120 quasi-2D images. The scalar dissipation at the lift-off height was one order of magnitude lower than the critical value for flame extinction which is similar to the results of Nandula et al. (1994). The maximum scalar dissipation rate is not correlated to temperature gradients or to the position of the instantaneous flame front. They concluded that scalar dissipation is of minor influence in flame stabilization compared to the formation of appropriate mixtures.

Chen and Mansour (1997) used a 1-D line-Raman/Rayleigh/PLIF-OH technique to measure simultaneously the species mass fractions of O_2, H_2, H_2O, N_2, OH and temperature in nonpremixed hydrogen jet flames. They found that joint correlations between a reactive scalar T with χ and the conserved scalar Z with χ were different from those reported in nonreacting flows. The observed distinct features can be explained based on the flamelet concept so that statistical independence is argued to be a good approximation. They also argued that large-scale turbulent motion dominates scalar transport in the connected reaction zone regime where the flamelet model is favored.

Multiscalar line imaging techniques have also been used recently in methane jet flames by Karpetis and Barlow (2002). They used Raman scattering, Rayleigh scattering, and CO-LIF to obtain simultaneous single-shot line measurements of major species, temperature and mixture fraction. The radial component of scalar dissipation was obtained in partially premixed methane/air jet flames (25% CH_4, 75% air, by volume). Both laminar and turbulent flames showed a local minimum in the conditional averaged scalar dissipation near the stoichiometric mixture fraction. In the turbulent flame, the radial component of the instantaneous scalar dissipation near the stoichiometric condition displayed a log-normal distribution at high values and an exponential distribution at low values. This was attributed to variation in the orientation of the 3-D mixture fraction gradient relative to the 1-D measurement. The length scale of fluctuations in mixture fraction in the turbulent reaction zone was derived from the measured single-shot radial profiles at each stream-wise location and was of the order of 1 mm.

1.3.2 Two-Dimensional imaging

Accurate point- and line-wise multi-species measurements can provide valuable statistical and partial spatial information at a given flame position at the expense of instantaneous spatial structures. Significant improvements have been made in the planar imaging techniques for measuring scalar dissipation. Successful 2-D imaging techniques, e.g. PLIF, Rayleigh and Raman imaging, to measure conserved scalars and scalar dissipation rate in flames have been demonstrated by using two-scalar (Kelman and Masri, 1997), three-scalar (Fielding et al., 1998) and four-scalar approaches (Kaiser et al. TNF7, 2004).

Assuming *unity Lewis number* and *one-step reaction*, a conserved scalar based on total enthalpy (*with radiation neglected*) can be defined as

$$\beta = Y_{fu} + c_p T / Q \, , \tag{1.14}$$

where Y_{fu} is the fuel mass fraction, c_p is the specific heat at constant pressure, T is the temperature, and Q is the lower heat of combustion. The mixture fraction can then be defined as

$$\xi = \frac{\beta - \beta_2}{\beta_1 - \beta_2} = \frac{Y_{fu} + c_p\left(T - T_2\right)/Q}{Y_{fu,1} + c_{p,1}\left(T_1 - T_2\right)/Q} \, , \tag{1.15}$$

where subscripts 1 and 2 define the fuel and air streams, respectively. The variable $Y_{fu,1}$ is the fuel mass fraction in the fuel stream. This is not the same as the fuel mass fraction if the fuel stream has been diluted. Simultaneous measurements of temperature and fuel concentration enable the measurement of β, and hence ξ.

Simultaneous 2-D Rayleigh and fuel Raman techniques were used by Starner et al. (1997) to measure the temperature and fuel mass fraction in air-diluted nonpremixed methane and hydrogen jet flames. Two components of the scalar dissipation rate were calculated. To increase the Raman signal, the measurements were made inside the cavity of a flash lamp-pumped dye laser. The Raman SNR was further improved by a contour-aligned image smoothing technique which used the high correlation between the Rayleigh and Raman signals. Results for the CH_4 flames indicated that the mean mixture fraction dissipation is nearly independent of the Reynolds number. In the H_2 flame, mean values for the axial and radial components of the scalar dissipation rate are nearly the same which shows a more isotropic structure than in the CH_4 flames. For both fuels, the PDF of χ on the axis was not lognormal. The profiles of conditional mean scalar dissipation showed a nonlinear dependence on mixture fraction and exhibited no clear resemblance to the skewed, mono-modal shapes seen in nonreacting flows. In the H_2 flame there was a strong correlation between the instantaneous, local values of scalar dissipation and the departure from equilibrium.

Two-dimensional Rayleigh and fuel Raman scattering measurements were also made by Kelman and Masri (1997) in piloted, nonpremixed flames over a range of jet velocities. Detailed calibration and correction for quenching and population distribution effects based on the simultaneous mixture fraction and temperature images were used to quantify the OH PLIF images. The measured mixture fraction, temperature, and OH concentrations were compared with earlier measurements in similar flames using the single-point Raman/Rayleigh/LIF technique and showed good agreement.

The two-scalar technique suffers from decreased sensitivity around the stoichiometric condition due to parent fuel loss and biases, i.e., very weak fuel-Raman signals. To get good signal both in the fuel-lean and fuel-rich region, N_2-Raman scattering was also added to the standard two-scalar approach by Fielding et al. (1998). This is the so-called three-scalar technique. To increase the Raman signal level, a single laser (532 nm) in a high-power intra-cavity configuration was also used. Mixture-fraction profiles calculated using independent fuel-temperature and nitrogen-temperature two-scalar approaches show excellent agreement in the laminar flame. For the turbulent flame, a 100-shot average of mixture fraction also showed reasonable agreement between the two approaches. Discrepancies were most evident in single-shot images in regions of large mixture fraction where the nitrogen Raman signal was noise dominated. The location of the stoichiometric contour was determined by both two-scalar approaches.

The combined polarized/depolarized Rayleigh scattering technique, which is also called *difference Rayleigh scattering*, was developed by Fielding et al. 2002. In difference Rayleigh scattering, temperature and fuel measurements are taken by simultaneously recording polarized and depolarized components of Rayleigh scattering. The depolarized Rayleigh scattering is a function of the effective depolarization ratio for the local composition. Spherically symmetric molecules, such as methane, have an extremely small depolarization ratio, and therefore in a methane/air flame, regions containing methane have a reduced depolarization ratio. When normalized to the signal in air, the difference between the polarized and depolarized signals provides a measure of fuel concentration. Simultaneous reaction-rate, mixture-fraction, and temperature imaging was demonstrated in laminar (Re = 1100) and turbulent (Re = 22,400) CH_4/air (1/3 by volume) jet flames.

Polarized/depolarized Rayleigh scattering and CO-PLIF was also used by Frank et al. (2002) in turbulent partially premixed methane/air jet flames. CO was used as the third scalar because it is a relatively strong function of mixture fraction near stoichiometric conditions and provides improved sensitivity for determining the mixture fraction. Its function is similar to that of N_2-Raman signal used by Fielding et al. (1998).

Sutton and Driscoll (2002) extended the two-scalar method by adding NO to the jet fluid to mark the fuel replacing previous fuel markers such as acetone. NO PLIF is combined with temperature images from Rayleigh scattering to measure mixture fraction and scalar dissipation rate with greatly improved SNR and spatial resolution. Their method has some advantages. First, differential diffusion problems are eliminated, since the diffusivity of NO is nearly equal to that of the methane/nitrogen fuel mixture. Second, NO is an excellent marker of the fuel (unlike acetone) since it properly disappears from centerline to the flame boundary due to rapid reactions with H and CH radicals. A small correction (typically 5% of the centerline value) must be applied to account for slight leakage of NO through the CH layer, but this correction can be made entirely from the experimental data. Finally, NO can be added in relatively large amounts to achieve exceptional SNR values (> 150) when the spatial resolution equals a typical Taylor scale of 400 μm. Radial profiles of mixture fraction and scalar dissipation rate in the calibration laminar flame compare favorably with previous measurements.

Planar imaging can provide information on the spatial structure of the scalar gradients, but this is usually at the expense of the number of scalars that can be instantaneously measured. Ideally, the mixture fraction should be determined by measuring all major species; however, this is impractical for 2-D imaging techniques, and a subset of these species is usually used to infer the mixture-fraction. There are limitations to how well such a subset of scalars represents the mixture fraction as effects such as differential diffusion, local extinction, Damköhler number, etc., will degrade the accuracy of the inferred mixture fraction. Therefore, these data must be viewed with caution. Furthermore, for most imaging techniques in flames, the SNR is usually lower than that can be obtained in equivalent point measurements and so some type of spatial averaging or filtering is used to improve the SNR. The need to improve the SNR is at odds with the need to obtain high spatial resolution to resolve the finest scales of turbulence.

1.4 THERMAL DISSIPATION

It can be argued that temperature does not play as fundamental a role as mixture fraction in determining the flame characteristics, but its fluctuations and gradients do provide important information about the underlying mixture fraction structure. This can be seen by considering the thermal dissipation rate

$$\chi_T = 2\alpha(\nabla T \cdot \nabla T) = 2\alpha|\nabla T|^2, \tag{1.16}$$

where T is temperature and α is the thermal diffusivity. χ_T is related to the rate of thermal mixing, or alternatively to the rate at which thermal inhomogeneities are removed by diffusion. Importantly, under the assumption of the state relationship $T = T(\xi)$, the scalar and thermal dissipation rates are related as

$$\chi_T = Le \cdot (dT/d\xi)^2 \chi, \tag{1.17}$$

Further, assuming *unit* Lewis number, the relation becomes

$$\chi_T = (dT/d\xi)^2 \chi. \tag{1.18}$$

In some regions of the flame, $dT/d\xi$ is approximately constant, in which case the thermal dissipation rate is proportional to the scalar dissipation rate.

Thermal mixing is also important because it affects high-temperature chemical reaction processes and can be important in the development and validation of turbulent flame models. For these reasons temperature fluctuations and thermal dissipation rates have been measured in a number of studies. Boyer and Queiroz (1991) measured characteristics of the thermal dissipation rate in a lifted turbulent non-premixed propane flame by using a dual-thermocouple technique. Probability density functions (PDFs) of χ_T were found to be lognormal, and the gradients were found to be nearly isotropic in regions close to the centerline, but anisotropic off the centerline.

One problem with thermocouples is that their resolution, both spatial and temporal is limited, and so this has driven the development of techniques that employ laser Rayleigh scattering to enable either continuous point measurements, e.g. Dibble and Hollenbach (1981), or 2-D imaging of temperature, e.g. Everest et al. (1995) and Fourguette et al. (1986), from which temperature gradients can be derived. In these techniques a specialized fuel (with approximately constant Rayleigh scattering cross-section with mixture fraction) is used, and so the Rayleigh scattering signal is inversely proportional to fluid temperature. For example, Gladnick et al. (1990) used a two-point laser Rayleigh technique to study the near field anisotropy in a turbulent diffusion flame. Auto- and cross-correlations and variance of temperature gradients were presented.

Effelsberg and Peters (1988) used two-point laser Rayleigh scattering and laser Doppler in non-reacting round propane-air jets and in the stabilization region of a lifted propane-air diffusion flame. The two points were geometrically determined by two rectangular slits of 0.4 × 0.34 mm separated by 0.6 mm. A 5W nominal Argon-ion laser was used but only 2W available at 488 nm. A multi-pass cell was used to increase the signal intensity by a factor of three. The mixture fraction was determined from the mapping of the measured Rayleigh scattering intensity to the mixture fraction. For the propane-air flame, this relation is non-monotonic and the time history of the Rayleigh signal was used to decide whether an instantaneous mixture fraction was larger or smaller than a specific mixture fraction value corresponding to the minimum Rayleigh signal. Once the mixture fraction was determined, the scalar dissipation rate was calculated from the two-point measurement. They concluded that the PDF of the scalar dissipation rate is close to a lognormal distribution.

Everest et al. (1995) used planar Rayleigh scattering to measure temperature fields in a turbulent jet flame with a fuel composed of 38% CH_4 and 62% H_2 at downstream locations of $x/d = 6$ to 42 and for Reynolds numbers of 4,000, 8,000 and 16,000. Broad and thin thermal mixing layers and flame-vortex interactions were observed in the thermal dissipation rate images. They further claimed that the mean normalized thermal dissipation profiles were similar to those of nonreacting jets, but values differed by a factor of two.

1.5 ISSUES TO RESOLVE

The mixture fraction in scalar dissipation measurements is usually calculated by using Bilger's formula (1988):

$$\xi = \frac{\dfrac{2(Y_C - Y_{C,O})}{W_C} + \dfrac{2(Y_H - Y_{H,O})}{W_H} - \dfrac{2(Y_O - Y_{O,O})}{W_O}}{\dfrac{2(Y_{C,F} - Y_{C,O})}{W_C} + \dfrac{2(Y_{H,F} - Y_{H,O})}{W_H} - \dfrac{2(Y_{O,F} - Y_{O,O})}{W_O}}. \tag{1.19}$$

From this definition, it can be clearly seen that scalar dissipation measurements require instantaneous (single laser pulse) spatially resolved measurements of multiple species in 3-D, so as to enable computation of the spatial derivatives of the mixture fraction in 3-D. To measure scalar dissipation accurately, the measurement must have sufficient spatial and temporal resolution. Ideally, the probe volume and response time should be smaller than the smallest scales of spatial and temporal fluctuations in the scalar field. Barlow et al. (TNF 6, 2002) summarized the difficulties in scalar dissipation measurements in turbulent nonpremixed flames. Two big issues remaining are (1) how to determine when the resolution is good enough to resolve the small-scale behavior; and (2) how to quantify the absolute accuracy of a scalar dissipation measurement. At TNF 7, the noise effects were further addressed by Barlow and Geyer et al. (TNF 7, 2004). The expected turbulent scales and the requirements for their resolution will be reviewed briefly in Sec. 1.5.1, and a discussion of noise issues will be given in Sec. 1.5.2.

1.5.1 Scales of turbulence

An important issue with scalar dissipation measurements is the need to obtain fully spatially- and temporally-resolved measurements of the finest scales of turbulence. This stringent requirement makes dissipation measurements particularly challenging. Batchelor (1959) argued that the finest scalar scale is set by the balance between the thinning effect of inner-scale strain and the thickening effect of diffusion. He proposed that at high Schmidt number, this finest scale (termed the *Batchelor scale*) will be

$$\lambda_B = \left(\nu D^2 / \bar{\varepsilon}\right)^{1/4}, \tag{1.20}$$

where ν is the kinematic viscosity, $\bar{\varepsilon}$ is the mean dissipation rate of turbulent energy, and D is the molecular diffusivity. In turbulent flows, the Batchelor scale is related to the Kolmogorov scale

$$\lambda_B = \lambda_K Sc^{-1/2}, \tag{1.21}$$

where *Sc* is the Schmidt number, $Sc = \nu / D$, and λ_K is the Kolmogorov scale

$$\lambda_K = \left(\nu^3/\bar{\varepsilon}\right)^{1/4}. \tag{1.22}$$

For high-Reynolds number flows, rate of turbulent kinetic energy dissipation is considered to be equal to the supply rate of the turbulent energy generated by the large scales, which is on the order of U^3/L (Tennekes and Lumley 1972), i.e.,

$$\bar{\varepsilon} = CU^3/L, \tag{1.23}$$

where U and L are the local characteristic velocity and length scales, and C is an empirical constant which is not universal and depends on the choice of U and L and also changes from flow to flow. Combining (1.22) and (1.23), the Kolmogorov scale is given by

$$\lambda_K/L = C_1 Re_L^{-3/4}, \tag{1.24}$$

where Re_L is a Reynolds number defined as

$$Re_L = UL/\nu, \tag{1.25}$$

and with $C_1 = C^{-1/4}$. The Batchelor scale can then be expressed as

$$\lambda_B/L = C_1 Re_L^{-3/4} Sc^{-1/2}. \tag{1.26}$$

In flames, the characteristic scales λ_B and λ_K are usually estimated from the outer-scale formulations (1.24, 1.26) owing to difficulties in the direct measurement of the dissipation rate ε.

Figure 1.1. shows a schematic diagram of a jet issuing into a co-flow. When the coflow velocity $U_\infty = 0$, the jet is called a *pure jet*. Pure jet flow is self-similar and its scaling laws are summarized by Chen and Rodi (1980):

$$\delta_{1/2} = 0.17\,(x - x_0), \tag{1.27}$$

$$\delta_{0.05} = 0.43\,(x - x_0), \tag{1.28}$$

$$U_c / U_0 = 6.2\, d / (x - x_0)\,, \tag{1.29}$$

where $\delta_{1/2}$ and $\delta_{0.05}$ are the FWHM and 5% jet widths respectively, and x_0 is the virtual origin of the far field turbulent flow as illustrated in Fig. 1.1.

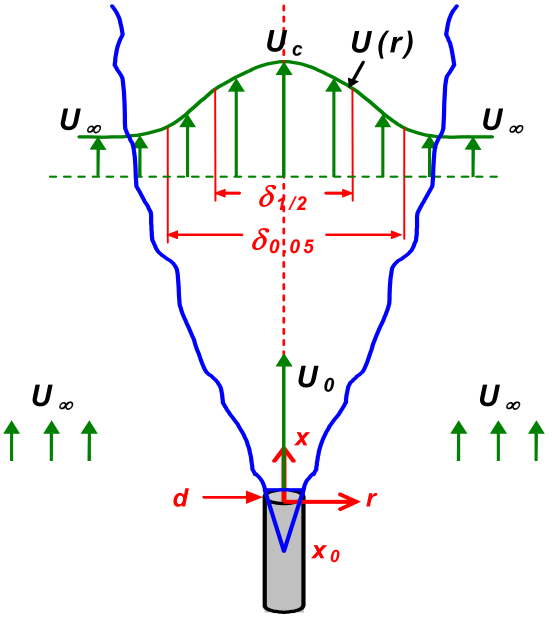

Figure 1.1 Round jet with coflow coordinates

The mean turbulent energy dissipation rate on the jet axis was measured by Friehe, Van Atta and Gibson (1971) to follow the relation

$$\bar{\varepsilon} = 48 \frac{U_0^3}{d} \left(\frac{d}{x - x_0} \right)^4 , \tag{1.30}$$

where U_0 is the jet-nozzle velocity, d the jet-nozzle diameter. The jet-nozzle Reynolds number can be defined as

$$Re(U_0, d) \equiv d U_0 / \nu\,, \tag{1.31}$$

In the far field, the centerline stream-wise velocity fluctuation on the jet axis is (Pope, 2000)

$$u_{rms}/U_c \approx 0.28\,. \tag{1.32}$$

From the above relations, one obtains:

$$\mathrm{Re}(U_0,d) = \frac{1}{1.054}\mathrm{Re}(U_C,\delta_{1/2}) = \frac{1}{2.666}\mathrm{Re}(U_C,\delta_{0.05})\,, \tag{1.33}$$

$$\lambda_K = L\, C_1(U,L)\, \left[Re(U,L)\right]^{-3/4}. \tag{1.34}$$

Table 1.1. Summary of C_1 for $\lambda_K = L\, C_1(U,L)\, \left[Re(U,L)\right]^{-3/4}$ in nonreacting jet flow. $r_{1/2}$ is the half width half maximum (HWHM) width of the jet and l is the integral length scale

C_1	$C_1(U, L)$	λ_K
0.38	$C(U_0, d)$	$0.38\left[Re(U_0,d)\right]^{-3/4}(x-x_0)$
2.3	$C(U_C, \delta_{1/2})$	$2.3\left[Re(U_C,\delta_{1/2})\right]^{-3/4}\delta_{1/2}$
1.8	$C(U_C, \delta_{0.05})$	$1.8\left[Re(U_C,\delta_{0.05})\right]^{-3/4}\delta_{0.05}$
0.9	$C(u_{rms}, \delta_{1/2})$	$0.90\left[Re(U_{rms},\delta_{1/2})\right]^{-3/4}\delta_{1/2}$
1.05	$C(u_{rms}, r_{1/2})$	$1.05\left[Re(U_{rms},r_{1/2})\right]^{-3/4}r_{1/2}$
1.2	$C(u_{rms}, l)$	$1.2\left[Re(U_{rms},l)\right]^{-3/4}l$

Table 1.2. Summary of C_1 used in the nonreacting circular jet flow experiments.

C_1	$C_1(U, L)$	Reference
2.4	$C(U_C, \delta_{1/2})$	Friehe et al., 1980 Antonia et al., 1980
2.3	$C(U_C, \delta_{1/2})$	Dowling et al., 1991
1.0	$C(u_{rms}, \delta_{1/2})$	Pitts et al., 1999
0.85	$C(u_{rms}, \delta_{1/2})$	Antonia et al., 1980

For example, using the jet exit Reynolds number $Re(U_0, d)$ and the stream-wise distance $(x - x_0)$, the Kolmogorov scale is

$$\lambda_K = 0.38 \cdot \mathrm{Re}^{-3/4}(U_0, d)(x - x_0)\,, \tag{1.35}$$

Tables 1.1 and 1.2 summarize C_1 values used in different experiments. In some papers, the $Re(U_0, d)$ and $Re(U_C, \delta_{1/2})$ were also expressed as Re_d and Re_δ respectively.

Several studies have imaged the scalar dissipation rate field in non-reacting turbulent jets (Buch and Dahm, 1996, 1998; Pitts et al., 1999; Su and Clemens, 1999, 2003; Dimotakis, 2002). These studies have shown that regions of high scalar dissipation are organized in intermittent sheet-like structures whose characteristic width is several times larger than the Batchelor scale as defined in (1.20). Furthermore, profiles taken normal to the centerline of scalar dissipation structures shows that the scalar concentration profile is similar to an error function and thus the dissipation profile is close to Gaussian. These were found experimentally by Buch and Dahm (1996, 1998) in both liquid (Sc>>1) and gas phase (Sc≈1) flows.

To characterize the characteristic thickness of these sheet-like dissipation structures, Buch & Dahm (1996) introduced the so-called strain-limited vorticity-diffusion and mass-diffusion scales λ_v and λ_D respectively, which follow the same scaling laws as the Kolmogorov and Batchelor scales but which have a different constant of proportionality, i.e.,

$$\lambda_v = \Lambda \delta Re_\delta^{-3/4}\,, \tag{1.36}$$

$$\lambda_D = \lambda_v Sc^{-1/2}\,, \tag{1.37}$$

where δ is a characteristic flow outer scale (e.g., a jet width or thickness), Re_δ is the Reynolds number based on this scale, and Λ is an empirical constant which is analogous to C_1. Buch & Dahm (1998) found that $\Lambda = 11.2$ when δ is the 5% velocity width in a circular jet. Su & Clemens (1999) performed a similar analysis for data taken in a planar jet, but arrived at a higher value of $\Lambda = 14.9$. In a more recent study by Tsurikov (2002) in a circular jet, the value of Λ was found to be 7.0 for $Re_\delta = 4{,}200$ and 10.6 for $Re_\delta = 9{,}600$ which suggested that the value of Λ is Reynolds number dependent.

Table 1.3. Summary of Λ used in the nonreacting jet flow experiments.

Λ	$\Lambda\ (U, L)$	Flow	Ref
11.2	$C(U_C,\ \delta_{0.05})$	Circular jet	Buch and Dahm, 1998 Southeralnd and Dahm, 1994
14.9	$C(U_C,\ \delta_{0.05})$	Planar jet	Su and Clemens, 1999
7.0, 10.6	$C(U_C,\ \delta_{0.05})$	Circular jet	Tsurikov, 2002

These results show that the characteristic mean width of the scalar dissipation structures is several times larger than the classical Batchelor scale. Although it would be advantageous to use λ_D as the resolution requirement in making scalar measurements, this would not be adequate for the accurate computation of the scalar dissipation rate, as will be discussed below.

Miller and Dimotakis (1991) argued that the normalized energy spectra deviate from a constant -5/3 power-law behavior at a wave number k_ν such that $k_\nu \lambda_K \approx 1/8$. Based on this observation, they introduced the "*inner viscous scale*" λ_ν

$$\lambda_\nu \approx \pi / k_\nu \approx 25 \lambda_K . \qquad (1.38)$$

This is the scale at which the action of viscosity becomes important. They also defined the so-called "*smallest expected scalar diffusion scale*"

$$\lambda_D = \lambda_\nu Sc^{-1/2} \approx 25\lambda_K Sc^{-1/2}. \tag{1.39}$$

In the recent work of Dimotakis (2000), he doubled the scale and defined it as

$$\lambda_\nu \approx 2\pi/k_\nu \approx 50\lambda_K \tag{1.40}$$

$$\lambda_D \approx 50\lambda_K Sc^{-1/2} \tag{1.41}$$

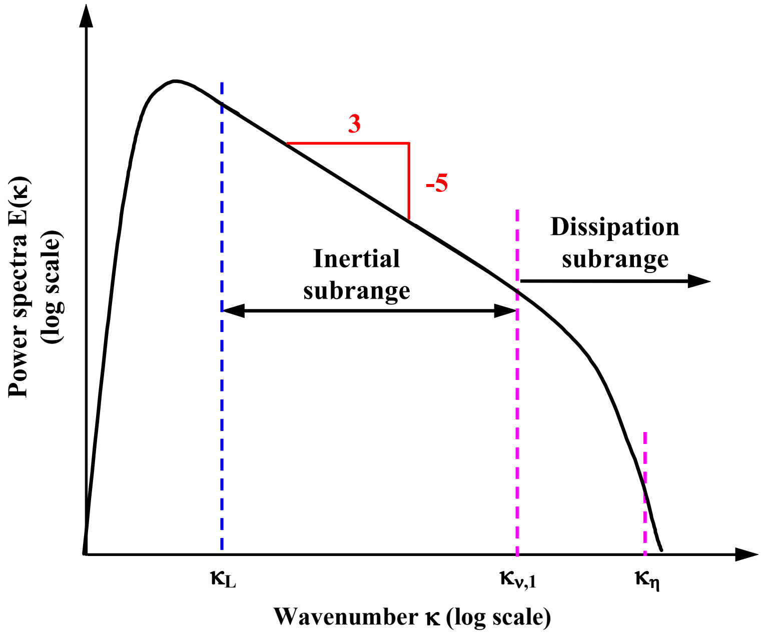

Figure 1.2 Power spectra of velocity fluctuations in high Reynolds number turbulent flows. $\kappa_{\nu,1}$ is the wavenumber for $\lambda_{\nu,1}$(the *inner viscous scale*, Dimotakis, 2000), κ_η is the wavenumber for Kolmogorov scale λ_η

These scales are different from the stain-limited vorticity- and mass-diffusion scales defined by Buch and Dahm (1996), though they used the same symbols. Clearly, the scales defined by Dimotakis (2000) are larger than the corresponding scales by Buch and Dahm (1996). Figure 1.2 shows the relative positions of these scales in the power spectra.

The resolution requirement for making accurate probe measurements of the scalar gradients has been specifically addressed in a few studies. For example, the influence of the effective probe resolution on the spectra and variances of the streamwise velocity and temperature fluctuations and their streamwise gradients were investigated analytically by Wyngaard (1968, 1969, 1971). The isotropic forms for the 3-D energy and scalar spectra were used in the analysis. His results suggested that both $\overline{(\partial u/\partial x)^2}$ and $\overline{(\partial T/\partial x)^2}$ decrease dramatically with increasing probe length. It was also found in Wyngaard (1971) that the 1-D spectrum of temperature was attenuated significantly when the wire length was sufficiently long.

Based on a review of previous studies as well as their own experimental data, Pitts (1998) and Pitts et al. (1999) concluded that the required spatial resolution for accurate measurements of scalar dissipation is on the order of the Batchelor scale and relaxing the spatial resolution requirement will result in significant volume averaging leading to large measurement errors.

Mi and Nathan (2003) employed a spectral method to study probe spatial resolution effects on the measured variances of a fluctuating scalar and its derivative at the far field of a circular jet and the near wake of a circular cylinder. They accomplished this by low-pass filtering time-series data using different cutoff frequencies. The passive scalar in both cases was the temperature of air which was a little higher than the ambient air temperature. They found that the spatial resolution required for accurate measurement of the scalar dissipation rate is close to the Batchelor scale. In addition, they also estimated the measurement errors for specific spatial resolution. For example, Fig. 1.3 shows that resolutions of $2\lambda_B$ and $10\lambda_B$ will result in the scalar dissipation rate being under-estimated by a factor of 10% and 55% respectively. For the scalar variance, the resolution requirement is not so stringent and an order of magnitude less resolution is required. Comparing the results of jet and wake flow experiments, one sees that the effect of degrading resolution is also flow-dependent.

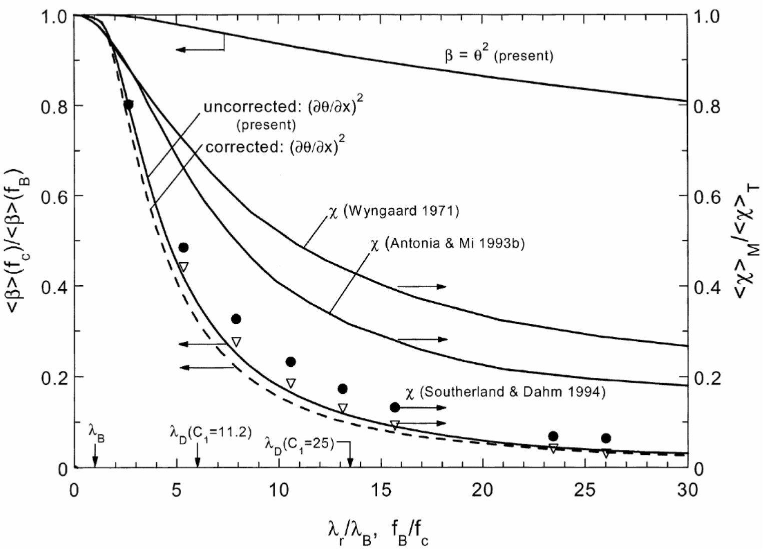

Figure 1.3 Effect of probe spatial resolution on measurements of scalar dissipation in the far field of a turbulent circular jet. θ is the measured scalar. (Fig. 2 in Mi and Nathan, 2003)

In turbulent flames, the resolution issue is relatively complicated. Effects originating from chemical reactions, i.e. heat release, buoyancy and radiation etc. must be considered in order to determine the smallest scales in a flame. To estimate the smallest scale for the mixture fraction dissipation measurement, it is not clear which Reynolds number should be used.

People tend to extend the extensive knowledge-base of non-reacting flows to flames. For example, in the study of the liftoff characteristics of turbulent jet diffusion flames, Peters and Williams (1983) used the same scaling of mixture fraction dissipation rate with downstream distance as that in the nonreacting jet flows, i.e. $\overline{\chi} \propto (x/d)^{-4}$. The obvious question is how well these relations work under flame conditions.

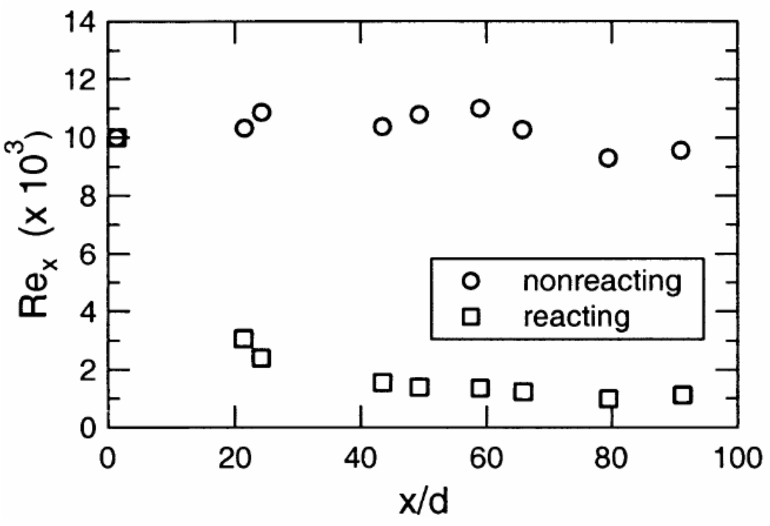

Figure 1.4 The local Reynolds number as a function of axial distance (*x/d*) for nonreacting and reacting jets with $Re_d = 10{,}000$. (Fig. 5 in Muniz and Mungal, 2001)

Muniz and Mungal (2001) studied the local Reynolds number definition in non-reacting jets to jet flames with the viscosity calculated at the elevated flame temperature. They showed that the local Reynolds number in jet flames decreases with increasing downstream distance as shown in Fig. 1.4. In non-reacting jets, the local Reynolds number does not vary with increasing downstream distance. Scaling laws of centerline velocity and mixture fraction in momentum-dominated jet flows have been extended to momentum-dominated jet flames with the modified source diameter by Peters and Donnerhack (1981), Peters (2000) and Tacina and Dahm (2001). It is not clear whether similar extensions can be used for other parameters, e.g., scalar dissipation rate, Batchelor scale and Kolmogorov scale. There remain many outstanding issues regarding the scalar dissipation rate in flames, e.g., does the Batchelor scale in flames have the same dependence on the Reynolds number as in non-reacting flows? How does one estimate this "*flame Batchelor scale*"? A careful check of mixture fraction measurements in reacting jets shows that this issue is far from being resolved. Apparently, to fully address this issue, the measurement itself must resolve scales smaller than the smallest scale predicted by possible theories. However, the low SNR that accompanies increasing resolution makes direct mixture fraction measurement techniques very difficult. This issue is reviewed in the following section.

1.5.2 Noise effects

Mi and Antonia (1994b) presented some work on the effects of noise on dissipation measurements. Based on the assumption of the independence of noise associated with different channels, they showed that the measured spatial gradient square term is

$$\overline{(\partial T/\partial x)_m^2} = \overline{(\partial T/\partial x)^2} + \left(\overline{n_1^2} + \overline{n_2^2}\right)/(\Delta x)^2 \tag{1.42}$$

It clearly shows that the measured squared gradient is always higher than its true value if there is noise in the signal. They further noted that when $\Delta x \to 0$, $\overline{(\partial T/\partial x)_m^2} \to \infty$; therefore for very high spatial resolution, i.e. small values of Δx, $\overline{(\partial T/\partial x)_m^2}$ can be significantly larger than $\overline{(\partial T/\partial x)^2}$.

Buch and Dahm (1996) used 2-D imaging technique to measure the scalar dissipation rate in a high Schmidt number (Sc = 2000) water jet at local outer scale Reynolds number of 2,000 to 10,000. To calculate the uncertainty of the scalar dissipation rate χ, an eight-point stencil (central difference scheme) was used,

$$\begin{aligned}\chi(i,j) = \; & \left[\frac{1}{4\Delta}\left(\xi_1 - \xi_2\right) + \frac{1}{8\Delta}\left(\xi_3 + \xi_4 - \xi_5 - \xi_6\right)\right]^2 + \\ & \left[\frac{1}{4\Delta}\left(\xi_7 - \xi_8\right) + \frac{1}{8\Delta}\left(\xi_3 + \xi_6 - \xi_5 - \xi_4\right)\right]^2\end{aligned} \tag{1.43}$$

They made several assumptions about the noise. First, the noise statistics in all adjacent pixels are the same, e.g. the mean ξ_i and variance $\sigma_{\xi_i}^2$ are the same. Second, noise levels in adjacent pixels are independent and all the covariances are zero. Based on these assumptions, the corresponding uncertainty in the scalar dissipation is:

$$\sigma_\chi^2 = \frac{3}{4}\chi\left(\frac{\sigma_\xi}{\Delta}\right)^2 , \tag{1.44}$$

$$\frac{\sigma_\chi}{\chi} = \frac{\sqrt{3}}{2}\frac{1}{\sqrt{\chi}}\left(\frac{\sigma_\xi}{\Delta}\right). \tag{1.45}$$

It should be noted that the measured variance σ_ξ^2 includes two contributions: one is from noise and the other is from turbulent fluctuations. Their results did not give the effect of noise alone on the scalar dissipation measurements.

Ferrao et al. (2000) did instantaneous 1-D line measurements of the CO_2 mass fraction by laser-induced Rayleigh scattering in a coaxial CO_2-air jet. The main source of uncertainty they found was the shot-noise caused by photon statistics. Their analysis showed that the shot noise of the Rayleigh scattering measurement induces a systematic error which causes an offset in the dissipation measurements. The correction to the scalar dissipation offset, which is a function of the shot noise variance, was derived. The dissipation is defined as

$$\chi = 2D(\xi_x)^2 = 2D(\partial\xi/\partial x)^2 , \tag{1.46}$$

where $\xi_x = \partial\xi/\partial x = (\xi_2 - \xi_1)/\Delta x$ is the spatial derivative, ξ_1 and ξ_2 represent the mass fraction at two adjacent points, and Δx is the distance between them. If the variance associated with the shot noise is $\sigma^2_{n,\xi}$, the corresponding variance of the spatial gradient is

$$\sigma^2_{\xi_x} = 2\sigma^2_{n,\xi}/\Delta x^2 . \tag{1.47}$$

If ξ is normally distributed, ξ_x is too, and it can be written as $\mu_{\xi_x} + \sigma_{\xi_x} Z$, where μ represents the average and Z is a unitary, Gaussian random variable with zero mean.

$$\chi = 2D(\mu_{\xi_x} + \sigma_{\xi_x} Z)^2 = 2D(\mu^2_{\xi_x} + 2\mu_{\xi_x}\sigma_{\xi_x} Z + \sigma^2_{\xi_x} Z^2) \tag{1.48}$$

$$\overline{\chi} = 2D(\mu^2_{\xi_x} + 2\mu_{\xi_x}\sigma_{\xi_x}\overline{Z} + \sigma^2_{\xi_x}\overline{Z^2}) = 2D(\mu^2_{\xi_x} + \sigma^2_{\xi_x}) \tag{1.49}$$

$$\sigma^2_{\chi} = 4D^2(4\mu^2_{\xi_x}\sigma^2_{\xi_x} + 2\sigma^4_{\xi_x}) = 8D^2\sigma^2_{\xi_x}(2\mu^2_{\xi_x} + \sigma^2_{\xi_x}) \tag{1.50}$$

An important implication is that the average of the dissipation value will suffer an offset due to shot noise effects. They called $2D\sigma^2_{\xi_x}$ the *shot-noise offset*. Figure 1.5 shows the significant shot-noise offset, which was about 40% of the measured centerline scalar dissipation, in their radial scalar dissipation profiles. However, their assumption is essentially the same as Buch and Dahm's, i.e. they neglected contributions from the turbulent fluctuations. This will work only when there is no fluctuation due to turbulence. Therefore, this analysis can only be applied to the correction of the noise offset for constant Rayleigh signal.

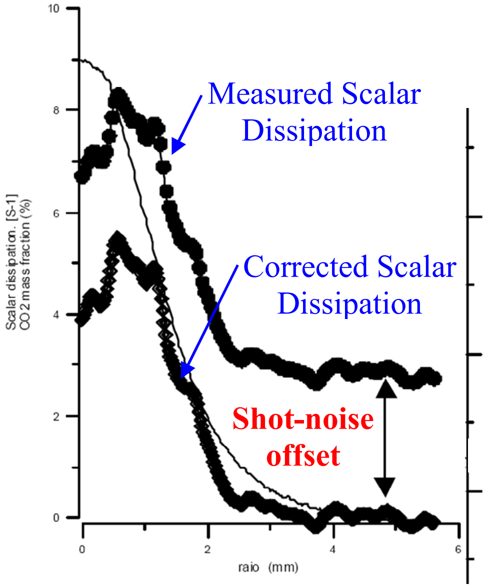

Figure 1.5 Comparing of the measured and corrected radial profiles of scalar dissipation of local CO_2 mass fraction (Fig. 6 in Ferrao et al., 2000).

In the 1-D line Raman measurement of scalar dissipation in a hydrogen jet flame, Nandula et al. (1994) defined the contribution of the scalar dissipation rate due to noise as the *apparent scalar dissipation rate* and measured it in a laminar adiabatic flame (the post-flame zone of a Hencken burner). The laminar flame is another ideal case where there are no turbulent fluctuations and then apparent scalar dissipation or noise-offset is from noise only. They also found that higher resolution results in a higher noise in the measurement.

Geyer et al. (2004) studied isothermal and reactive turbulent opposed flows by LDV and 1-D Raman/Rayleigh spectroscopy. The scalar dissipation rate across the mixing and reaction layer was determined on a single-shot basis. A large-eddy simulation with a steady flamelet model was used to estimate the influence of experimental noise upon a measured scalar dissipation. The experiments showed increased probability of low scalar dissipation rate, which deviates from log-normality and is similar to the jet flame results. They attributed this deviation from log-normality to noise, the 1D-technique, and the mixing process itself. Because experimental errors are significantly magnified in scalar dissipation measurements, they believed that the addition of noise was very important for the comparison of experimental data with results of numerical simulations. Their results did suggest that the noise effect is very important for experiments whose objective is LES validation.

In real scalar dissipation experiments, the resolution and noise effects are correlated. As discussed earlier, the effect of finite resolution always leads to under-estimation of the true scalar dissipation rate. Conversely, the effect of noise leads to an over-estimation of the true dissipation rate. Also, the increased resolution is always at the expense of lower signal intensity or SNR. These contradictory effects are hard to correct for in practical measurements.

1.6 SCOPE OF THE CURRENT INVESTIGATION

Because of these difficulties in making accurate scalar dissipation measurements in flames, it may be advantageous to make measurements of a quantity, such as temperature, which is only indirectly related to mixture fraction. The temperature may not be as fundamental to determining the reaction zone structure as the mixture fraction, but it can provide important information about the underlying turbulence. This approach is made more attractive because temperature fluctuations and gradients can be made with higher signal-to-noise ratio than equivalent measurements of the mixture fraction field. This is because temperature can be measured via Rayleigh scattering, which has higher SNR than Raman scattering.

This is the approach taken in the current study. The specific objective is to make laser Rayleigh temperature and thermal dissipation measurements in a weakly co-flowing turbulent nonpremixed jet flame with high SNR ratio and where the finest scales of turbulence are spatially and temporally resolved. The radial temperature gradients are measured by a two-point technique, whereas the axial gradient is measured from the temperature time-series combined with Taylor's hypothesis.

The first part of this work was to develop a two-point high-repetition rate laser diagnostics system which is discussed in chapter 2. For most optical diagnostics techniques in flames, changes in resolution are always accompanied by variation in the noise level. This makes the assessment of the noise and resolution issues even harder than in non-reacting flows. Resolution and noise issues inherent in the scalar dissipation measurements must be carefully quantified before using experimental results to validate numerical simulations, to develop theoretical models and to infer underlying physical phenomena. For example, how do resolution and noise interact with each other? Are there any other factors that will significantly affect the accuracy of the measured scalar dissipation? How can the accuracy be improved in scalar dissipation experiments? To answer these questions, a system model was developed to account for the effects of resolution, noise, filtering and data processing on the measured dissipation. This is discussed in Chapter 3. Noise will create an apparent dissipation (or bias), which will be more significant at small spatial resolution. For the current two-point time-series thermal dissipation measurements, techniques to correct the measured mean dissipation for this bias will also be developed in Chapter 3.

The flame studied here is similar to the TNF simple jet flame (DLR_A) which is used as a benchmark flame for the TNF Workshop (TNF website: http://www.ca.sandia.gov/TNF/). The two-point laser Rayleigh scattering data were used to study the temperature fluctuations, power spectra, gradients and thermal dissipation rate characteristics of this nonpremixed turbulent jet flame at a Reynolds number of 15,200. Two independent methods were developed for estimating the apparent dissipation resulting from noise effects. These results will be discussed in Chapter 4.

Chapter 2 Experimental setup and data reduction

2.1 EXPERIMENTAL SETUP

The first part of this work was to develop a high-repetition rate laser diagnostics system for point measurements. The system included a diode-pumped Nd:YAG laser, multiple Photomultiplier Tubes (PMTs) with a multi-channel high voltage power supply system, multi-channel data acquisition (DAQ) system, and a custom-designed low f-number optical collection system. Furthermore, a new particle-free co-flowing jet flame facility was developed, which consists of a concentric jet surrounded by a High Efficiency Particulate Air (HEPA) filtered co-flow, a two-dimensional linear translation system, and the fuel supply and metering system.

(a)

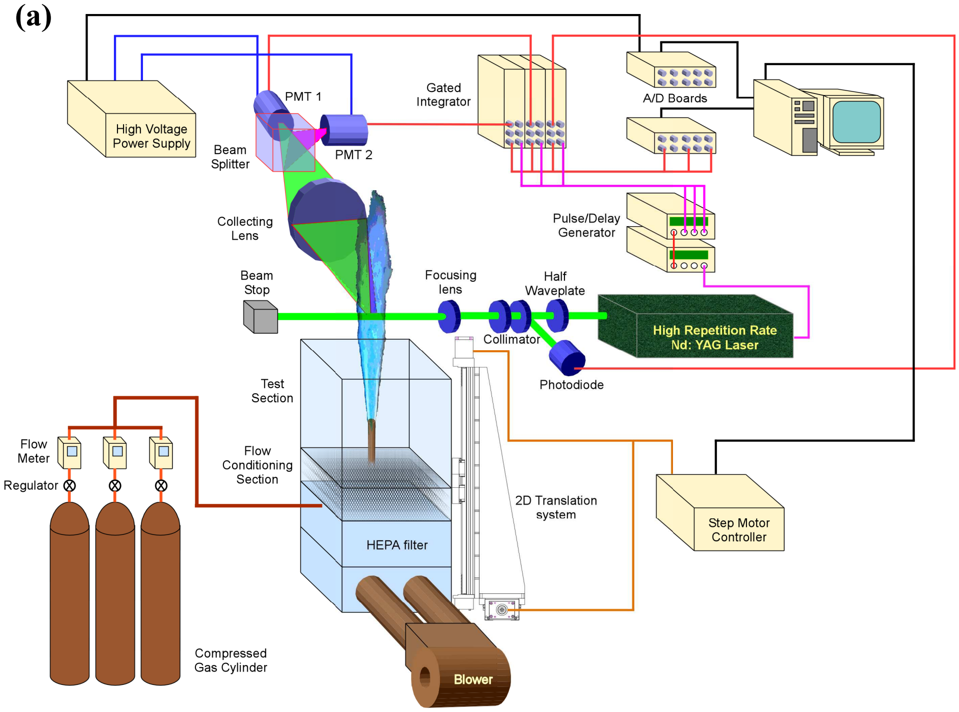

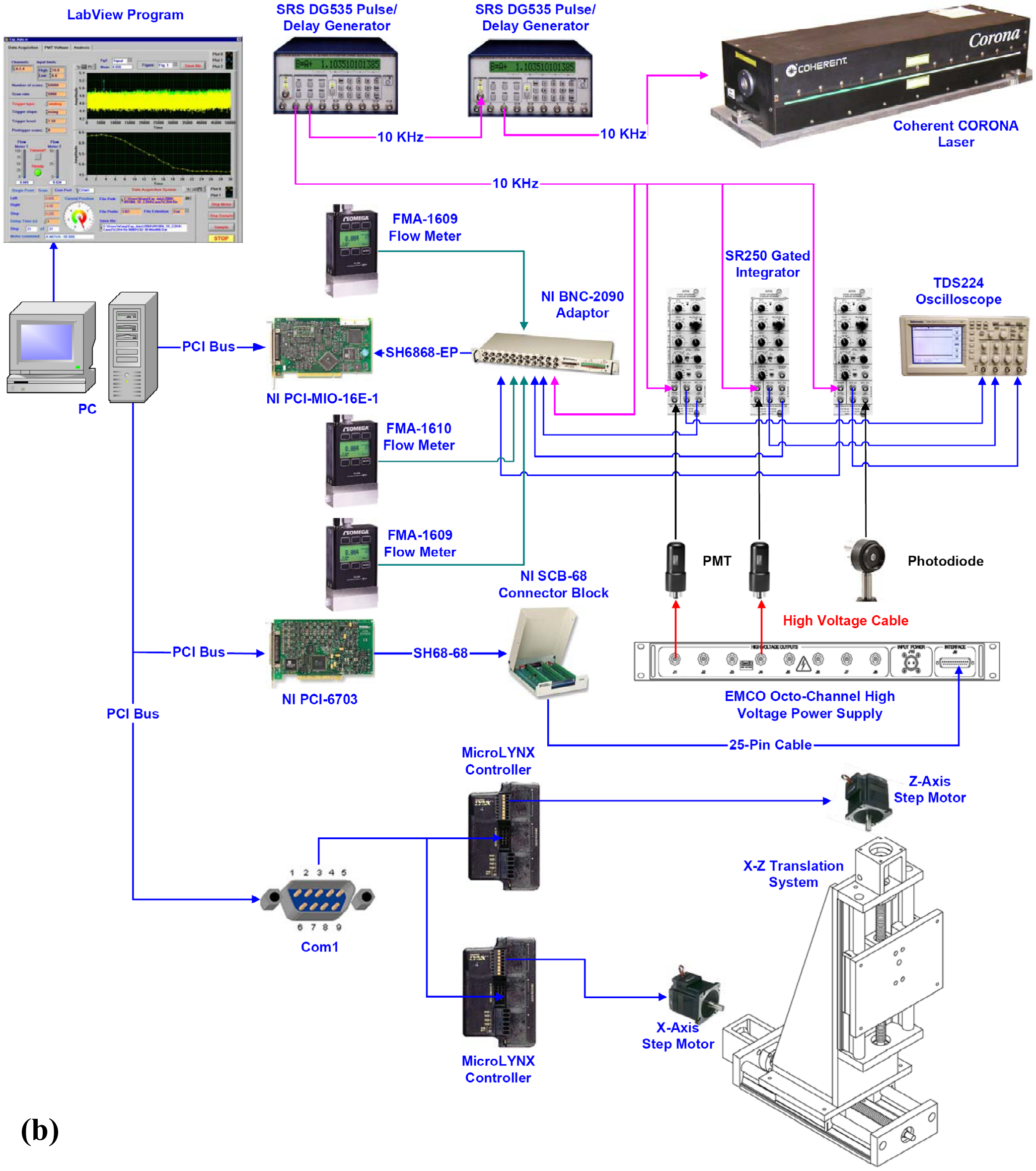

(b)

Figure 2.1 Experimental setup (a) experimental setup illustration, (b) experimental instruments and hardware illustration

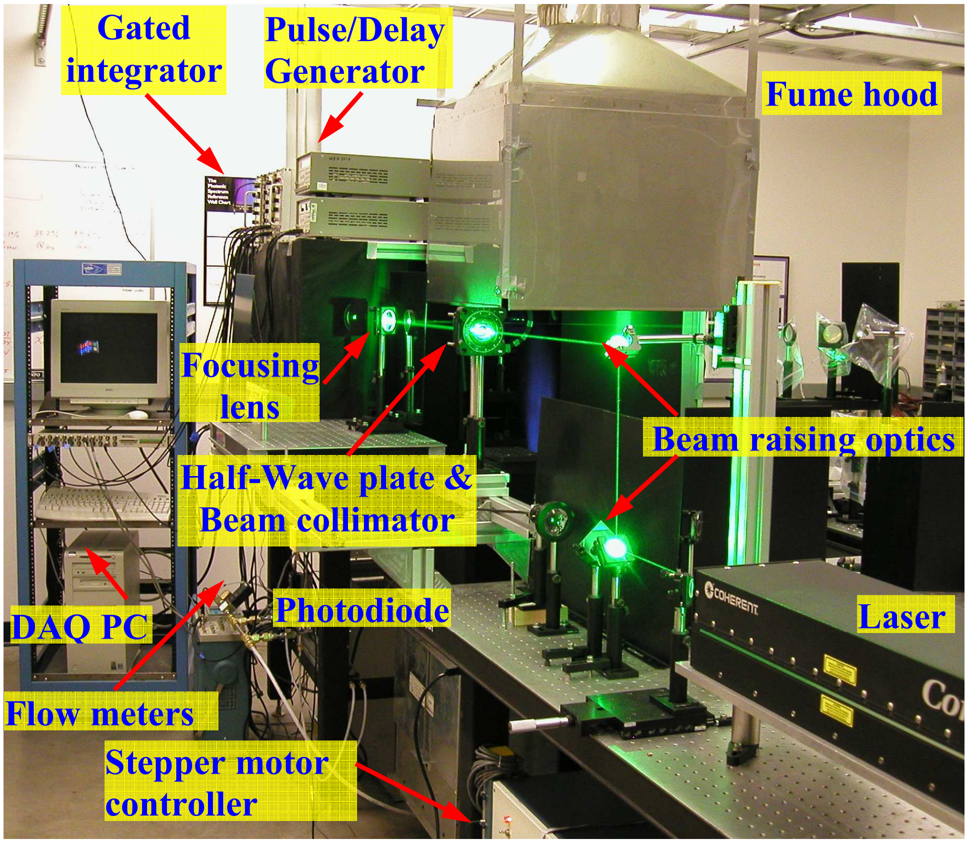

Figure 2.2 Experimental instruments and system picture

A LabVIEW program was developed to control and synchronize the whole experiment. The whole system is illustrated in Fig. 2.1(a) and (b) and the real setup is shown in Fig. 2.2.

2.1.1 Particle-free co-flowing jet flame facility

2.1.1.1 Particle-free co-flowing jet flow facility

The particle-free coflow jet facility is shown in Figure 2.3. The coflow was supplied by a 545 CFM industrial blower (Dayton model 5C508) and entered the jet facility through two 4″ PVC pipes. After passing the HEPA filter (95%

DOP efficiency), the flow was conditioned by the flow conditioning section prior to entering the test section. The flow conditioning section consisted of a layer of honeycomb, a layer of coarse screen, a perforated plate and a fine screen. This coflow conditioning section design followed that of Tsurikov (2002). The flow exited at the top of the test section and was removed from the laboratory through a fume hood. The whole system was 22″ wide by 22″ long by 45″ high. The jet issued upward from a circular straight tube located at the center of the test section. The jet exit was 45 cm above the last screen of the flow conditioning section. The whole jet flow facility was mounted in a X-Z transverse.

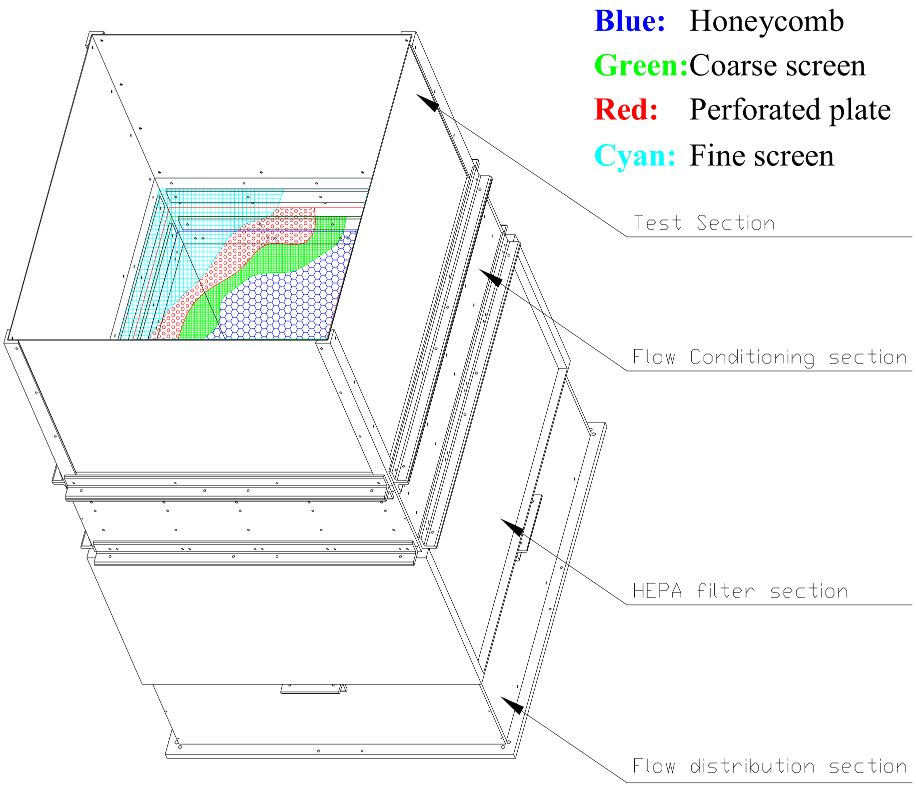

Figure 2.3 Particle-free coflow jet flow facility

The design objectives are to remove particles and deliver the coflow uniformly into the test section. The air flow exiting the blower is turbulent and non-uniform, and must be conditioned into a slow, uniform stream using as little space as possible. Flow conditioning is traditionally accomplished using screens and honeycomb to reduce turbulence level and swirl. These devices depend on stagnation pressure drop, which decreases with decreasing flow speed. In the current setup, the HEPA filter section can also reduce the turbulence level and swirl by introducing additional pressure drop.

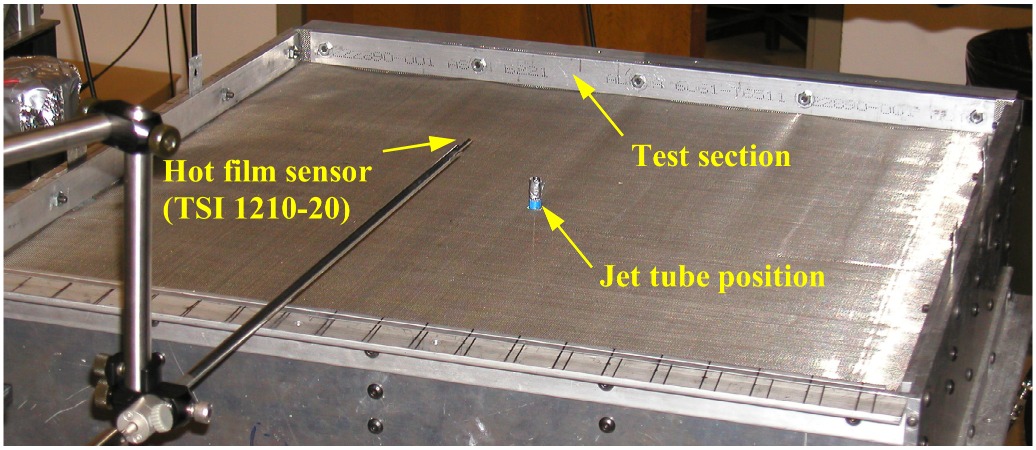

Figure 2.4 Scanning of the hot film across the test section exit plane

The jet coflow quality was measured using hot film anemometry. In the current study, a constant-temperature hot film sensor (TSI 1210-20) was operated at 250 °C by a linearized anemometer (TSI 1054B) designed to output a voltage linearly proportional to the flow speed. The sensor was scanned across the test section, and output voltage data were gathered at 19-by-19 evenly-spaced (1″ apart) stations as shown in Fig. 2.4. The voltage data were measured by sampling the hot wire output voltage using a PC equipped with a data acquisition board (National Instruments PCI-MIO-16E-1) and LabVIEW software. The sampling frequency (4000 Hz) and data acquisition time (25s) were sufficient to resolve all turbulent fluctuations and achieve converged statistics.

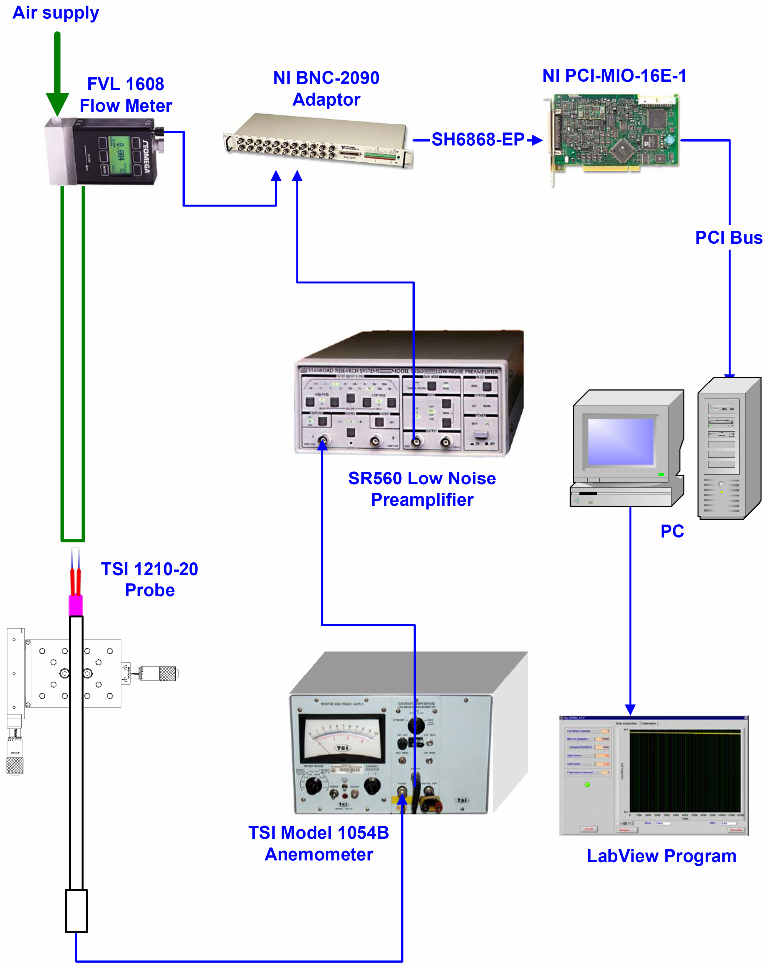

Figure 2.5 Hot film calibration diagram

One difficulty with using a hot film sensor for low speed measurement is that the sensor could not be reliably calibrated for low speeds (below 2 m/s). A plenum-nozzle calibrator is inadequate to measure the small pressure differences corresponding to such low speeds, and complex calibration techniques are required. Alternatively, fully developed laminar flow from a long tube was used to calibrate the hot film sensor in this study. To get a fully developed laminar flow, the tube Reynolds number should less than 2300 and the tube *L/d* greater than 100, where *L* and *d* are the length and diameter of the tube respectively. The tube used was 6 feet long, half-inch outer diameter, 0.43″ inner diameter (*L/d* = 167). The calibration setup is illustrated in Fig. 2.5.

The hot film sensor is placed close to the tube exit and the peak velocity location was found by placing the sensor on a 2D translation stage (1 μm resolution) and scanning in two directions. The theoretical relations for a fully developed laminar tube flow are:

$$U(r) = U_{max}(1 - r^2/r_0^2) \tag{2.1}$$

$$U_{\max} = 2U_{mean} \tag{2.2}$$

$$U_{mean} = Q/A \tag{2.3}$$

where r_0 is the tube radius, Q is the volume flow rate and $A = \pi r_0^2$ is the tube area. This leads to the relation between the tube volume flow rate measured by volume flow meter and tube exit maximum velocity measured by hot film:

$$U_{\max} = 2Q/A \tag{2.4}$$

At each flow rate, five measurements were taken and the averaged values were used to do the curve fitting. The flow rate range was from 0.86 LPM ($U_{max} = 0.31$ m/s) to 1.98 LPM ($U_{max} = 0.70$ m/s) so as to include the coflow velocity. The output voltage signal V from the linearized anemometer is related to Q by a linear formula from the calibration:

$$U_{\max}[m/s] = 0.00149 \cdot V[mV] + 0.212 \qquad (2.5)$$

where V is the hot film reading. The calibration curve is shown in Fig. 2.6.

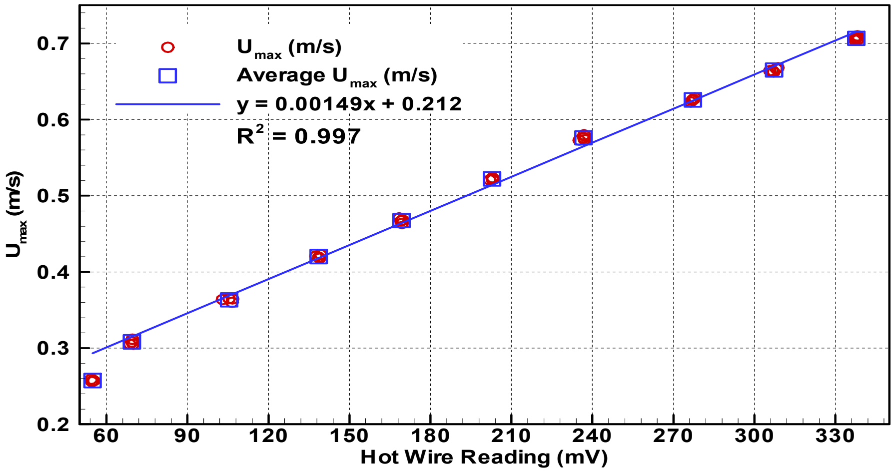

Figure 2.6 Hot film calibration result

The calibration uncertainty is mainly due to the accuracy limits of the volume flow meter. The Omega FVL 1620 flow meter has $\pm 1\%$ full scale accuracy for air which results in an uncertainty of ± 0.2 SLPM. The relative error for the velocity measurement is:

$$\sigma_U / U = \sigma_Q / Q \qquad (2.6)$$

For mean velocity $U = 0.46$ m/s, the corresponding flow rate $Q = 1.30$ SLPM. Therefore, the relative error for the measured mean velocity is $\sigma_U / U = \sigma_Q / Q = \pm 0.2/1.30 = \pm 15\%$ and the measured mean velocity is $U = 0.46 \pm 0.07$ (m/s).

The measured mean 2-D axial velocity contour is shown in Fig. 2.7 and the corresponding turbulence intensity, $TI = u_{rms}/U$ contours is shown in Fig 2.8. The statistics of the mean data is shown in Fig. 2.9. The mean axial velocity across the whole test section is 0.46 m/s. The turbulence intensity is uniform at the center of the test section. The turbulence intensity at the center of the test section is relatively higher than at neighboring points due to the presence of the jet tube. It can be seen that the flow quality at the edge of the test section is not very good. However, the jet exit is at the center of the test section and is 45 cm above the screens. Therefore, this coflow quality is considered to be good enough for the current measurements.

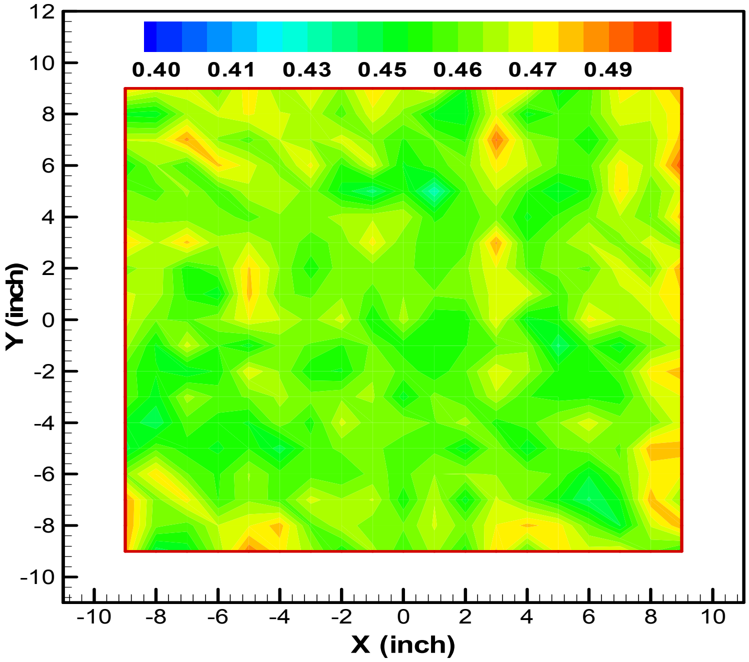

Figure 2.7 Mean axial velocity of the jet coflow facility

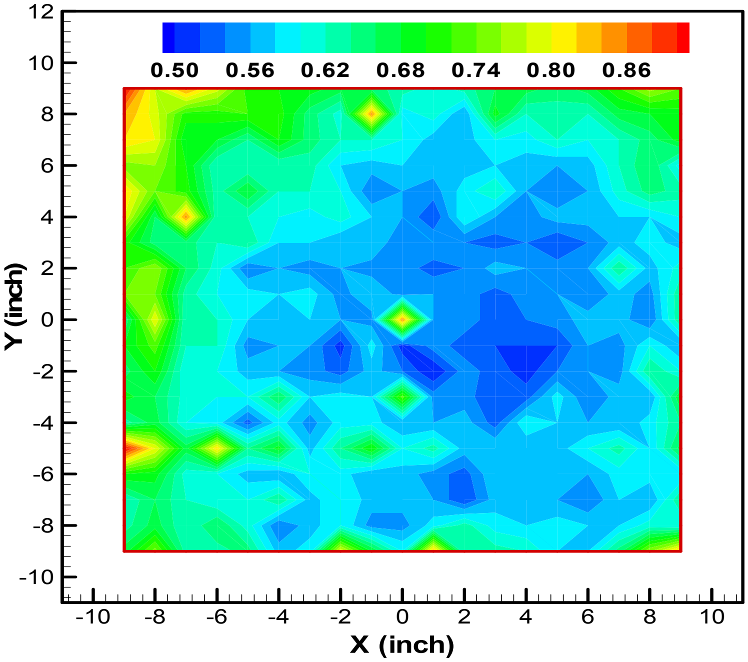

Figure 2.8 Turbulence intensity (%) of the jet coflow velocity

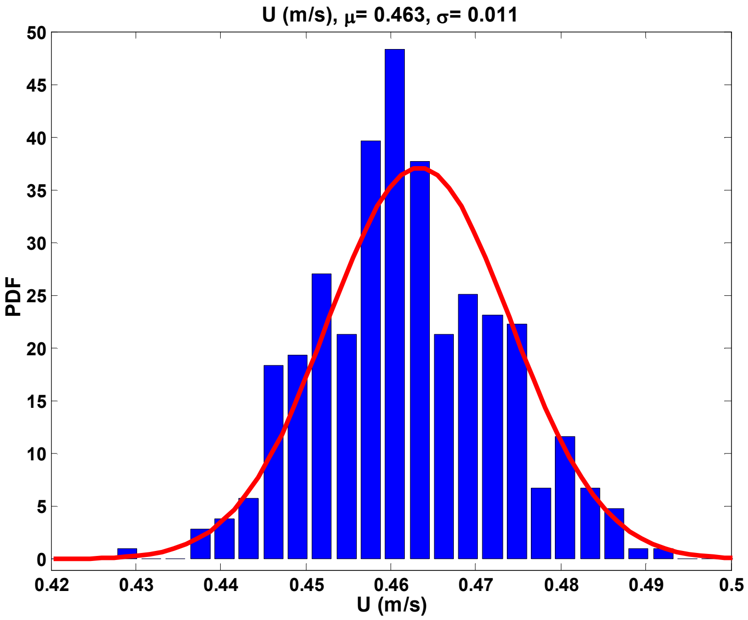

Figure 2.9 Coflow velocity PDF

2.1.1.2 Fuel supply and metering system

Three fuel meters are available to monitor the fuel flow rate and the system allows to mix up to three species at the same time. The fuel mass flow meters properties are listed in Table 2.1 (OMEGA Engineering, Inc.). There are valves and tee connectors downstream of the flow meters as shown in Fig 2.10.

Table 2.1 Fuel meter summary

Model Number	Type	Flow range	Accuracy	Repeatability
FMA-1609	Mass	50 SLPM	± 1% full scale	± 0.5% full scale
FMA-1609	Mass	50 SLPM	± 1% full scale	± 0.5% full scale
FMA-1610	Mass	100 SLPM	± 1% full scale	± 0.5% full scale

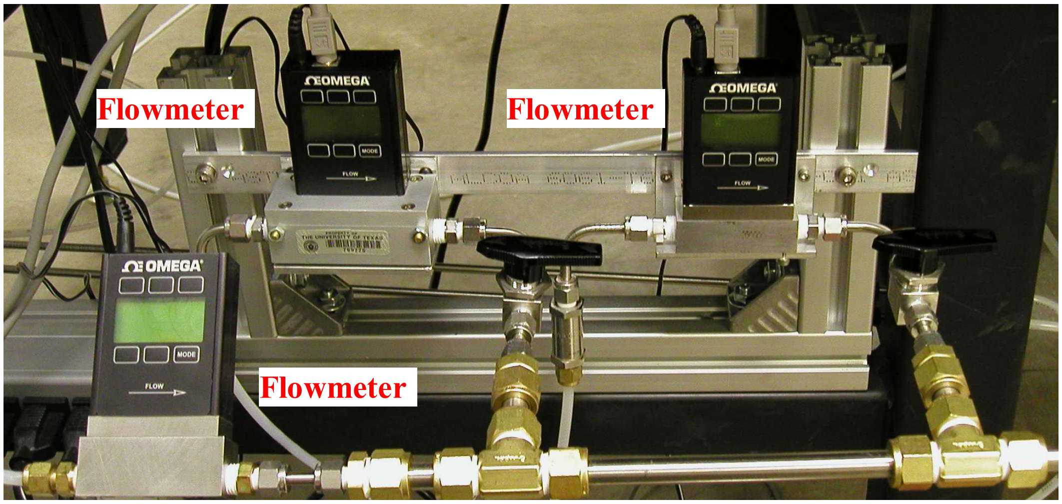

Figure 2.10 Fuel supply and metering system

The pressure drop after the volume flow meter will affect the reading, especially when multiple species are mixed. To reduce this reading error, an additional pressure gauge should be installed after the volume flow meter to measure the pressure and correct the reading of the volume flow meter. Therefore, volume flow meters are not desirable for fuel metering when more than one fuel species is used. The mass flow rate meters shown in Table 2.1 were used in the current experimental setup. These mass flow rate meters can indicate the flow rate in liter-per-minute (LPM) and standard liter-per-minute (SLPM). They can also measure the local fuel pressure and temperature. A selection of fifteen possible fuels is available for each mass flow meter.

2.1.2 Laser system

The core element of this experiment is the high-repetition rate diode-pumped Nd:YAG laser (Corona, Coherent Inc.) shown in Fig. 2.1. The laser is continuously pumped but is acousto-optically Q-switched to produce 130 ns (FWHM) pulses. The pulse repetition rate is adjustable from 5 to 25 kHz. The light is intra-cavity frequency doubled and produces 75 W of average power at 532 nm when pulsed at 10 kHz. This corresponds to about 7.5 mJ per pulse at this frequency. The pulse-to-pulse energy stability is 0.3% over half an hour. The maximum output pulse energy is 14 mJ at 2.9 kHz (Coherent Corona Manual).

The laser light is expanded and collimated with a beam diameter of 20 mm before going through the beam forming lens (330 mm focal-length and 50.8 mm in diameter). The beam waist diameter d_b (e^{-2} spot diameter) of the focus spot is limited by the multi-mode nature of the laser (M^2 factor):

$$d_b = \frac{4 f \lambda M^2}{\pi d_i} \tag{2.7}$$

where d_i is the incident beam diameter, M^2 is a factor that depends on the multimode characteristics of the laser beam, f is the focal length of the lens, and λ is the wavelength of the laser. A Gaussian (diffraction-limited) beam has $M^2=1$.

The Rayleigh range x_R is the distance along the beam from the focus to the point where the beam diameter is $\sqrt{2}$ times the diameter at the focus, and is defined as

$$x_R = \frac{\pi d_b^2}{4\lambda M^2} \tag{2.8}$$

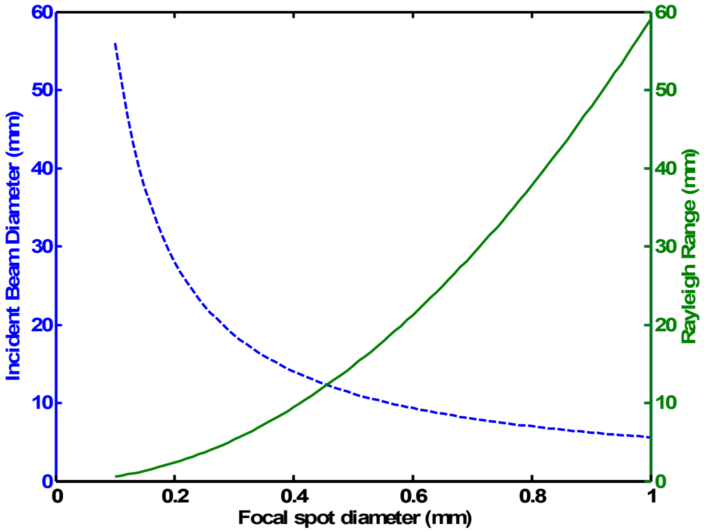

Figure 2.11 Beam focal spot diameter and Rayleigh range calculation for $M^2 = 25$

These relations show that the larger the M^2 value, the larger the focal spot diameter and the smaller the Rayleigh range. The calculation of beam focal spot diameter d_b and Rayleigh range for $M^2 = 25$, which is the M^2 value of the current laser system, is shown in Fig. 2.11. For the incident beam diameter of 20 mm the focal spot diameter is about 0.3 mm and the corresponding Rayleigh range is about 4 mm. This implies that the 0.3 mm spatial resolution can be kept within 4 mm range.

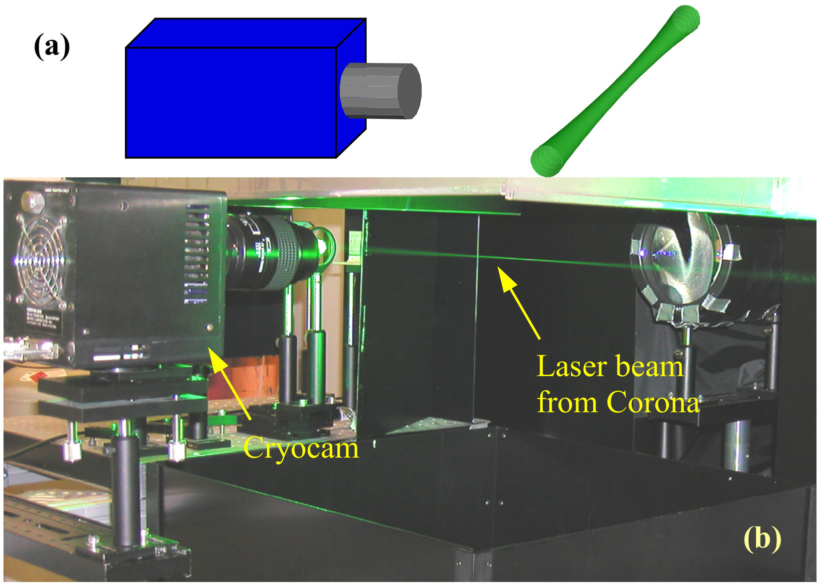

Figure 2.12 (a) Illustration of imaging Corona laser beam, (b) Experimental setup for imaging Corona laser beam

The beam size of the Corona laser was measured experimentally by imaging the Rayleigh scattering of the laser beam with a CCD camera (Cryocam S5 series) as shown in Fig. 2.12. The camera is a slow-scan camera with a thermoelectrically cooled, back-illuminated CCD (quantum efficiency 75% at 532 nm) with a resolution of 512 × 512 pixels. The camera was fitted with a Nikon 105 mm lens operated at three f-numbers: f/2.8, f/5.6 and f/11. A pixel of the camera projects to a 65 × 65 μm region of the object plane.

The pixel resolution considers only geometric relations between object and image planes. For fast optics, i.e., small f#, the actual resolution may also be affected by the camera lenses (Clemens, 2000). This blurring effect due to camera lenses can be reduced by using large f#, e.g. f# > 5. For a camera lens, the resolution is determined by the pixel resolution and/or the camera lens blurring effects. The blurring effects can be determined by using different f# to image a same object. If images of different f# show the same result, the camera lens blurring effects can be neglected.

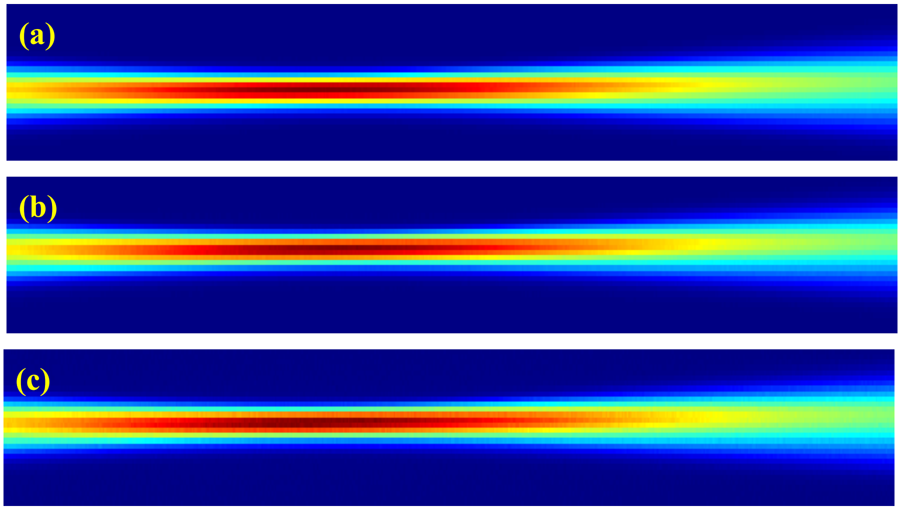

Figure 2.13 Images of Corrona laser beam by Cryocam camera, from top to bottom (a) f/2.8, (b)f/5.6 and (c) f/11

The laser was run at 10 kHz, the current was 23.5 A and the pulse energy was about 7.2 mJ/pulse. The exposure time of the camera was set to 0.08 s so that 800 pulses were accumulated per image. To increase the SNR further, 10 images were averaged, and therefore there are 8,000 laser pulses per averaged image. These images are shown in Fig. 2.14 with three different f# values. The images are cropped from 512 × 512 pixels to 20 × 512 pixels which corresponds to a 1.3 × 33.28 mm Field-of-View (FOV).

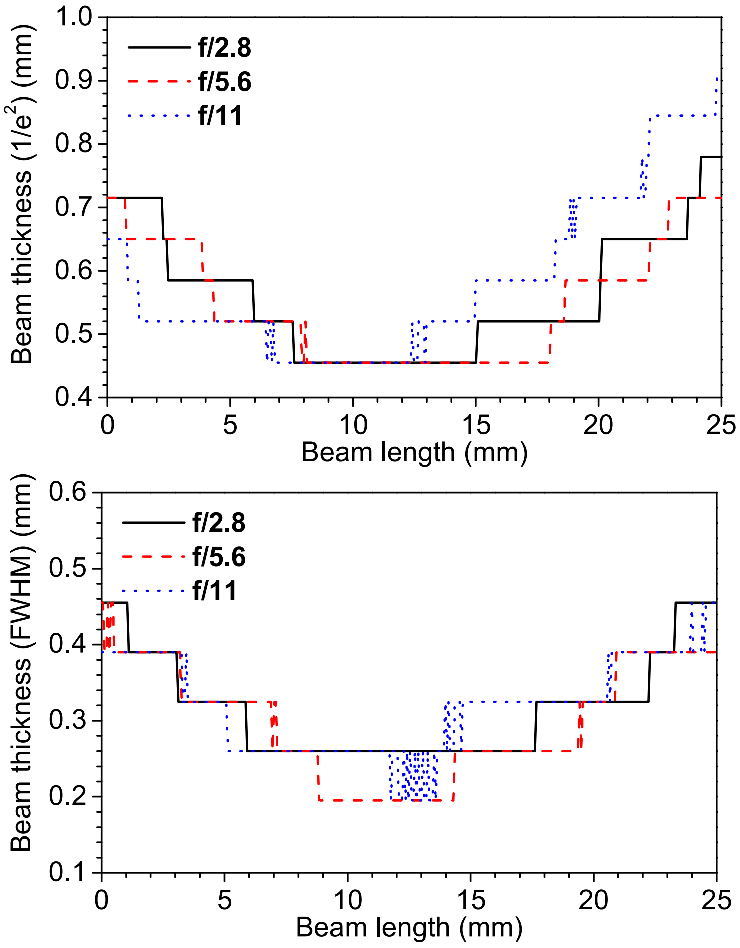

Figure 2.14 Corona laser beam thickness (a) e^2 (b) FWHM

Two beam thickness definitions are used; one is the e^2 beam thickness and the other is the Full-Width-Half-Maximum (FWHM) beam thickness. A MATLAB program was used to calculate the laser beam thickness and the results are shown in Fig. 2.14. The steps shown in the figures were due to the finite pixel resolution in the beam width direction which was 65 μm.

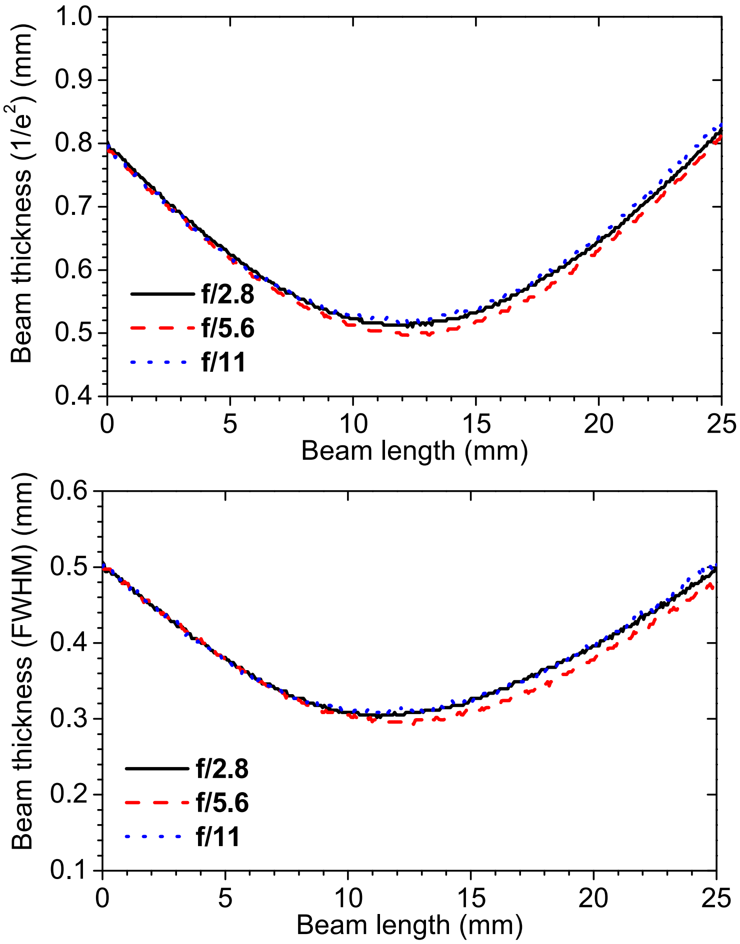

Figure 2.15 Corona laser beam thickness (a) e^2 (b) FWHM

To increase measurement accuracy, the data were interpolated to a finer grid as shown in Fig. 2.15. From these interpolated curves, the minimum e^2 beam thickness was estimated to be about 500 μm and the FWHM thickness about 300 μm. The measured value is somewhat different than the one calculated from Eqn. (2.7). The discrepancy could be due to the estimated M^2 factor and the fact that the beam is not truly collimated before entering the beam focusing lens.

2.1.3 Low f-number optical collection system

2.1.3.1 Optical design

The Rayleigh scattered light was collected at right angles to the incident beam by a custom designed 330-mm focal-length f/2.4 collection lens system. The detection system includes a pair of 145 mm diameter plano-convex lenses, one 50 mm diameter meniscus lens and one 50.8 mm diameter bi-convex lens. The working *f#* was 2.4 and the magnification was 0.685. The lenses are listed in Table 2.2 and the configuration is shown in Fig. 2.16. The ray tracing diagram from ZEMAX for three ideal points separated by 0.5 mm in the object plane is also shown in Fig. 2.16. The images of these three points are not points any more in the image plane due to the spherical aberrations. The magnification of the whole system is -0.685 which implies an inverted and minified image formed at the image plane as illustrated in Fig. 2.16 also.

Table 2.2 Component lenses of the detection system (Model # from Melles-Griot)

Lens	*d* (mm)	*f* (mm)	Type	Model #*
L1	145	300.0	Plano-Convex	01LPX311
L2	145	300.0	Plano-Convex	01LPX311
L3	50	-150.0	Meniscus	01LMN011
L4	50.8	101.6	Bi-Convex	01LDX179

The function of the meniscus and bi-convex lens can be clearly seen from Fig. 2.17. The spot radius from a pair of 150 mm diameter plano-convex lens is about 6.3 mm due to spherical aberrations.

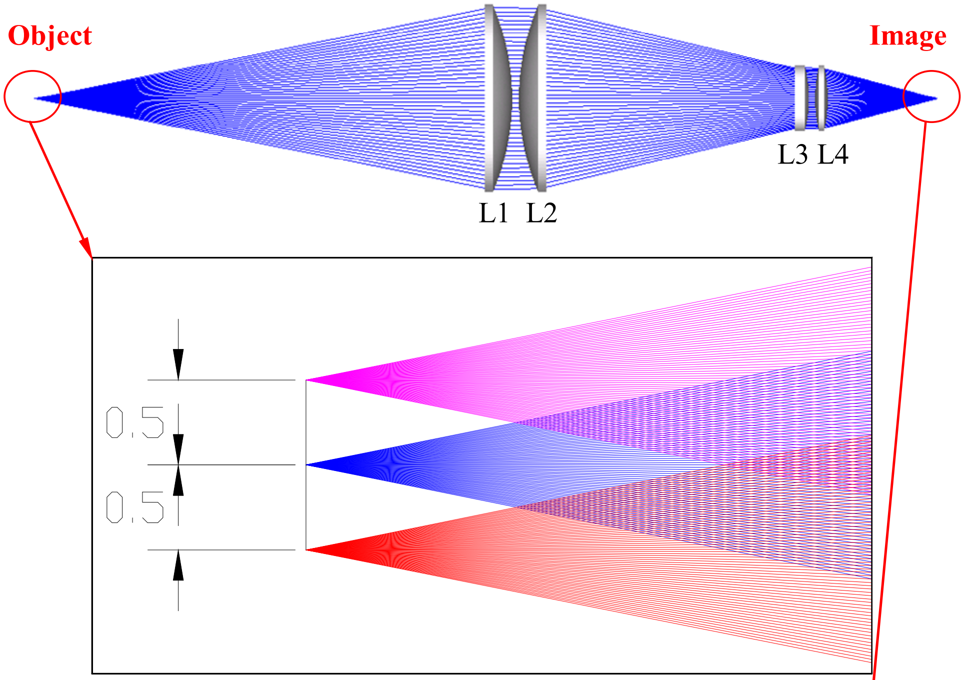

(a) Three ideal objects 0.5 mm apart

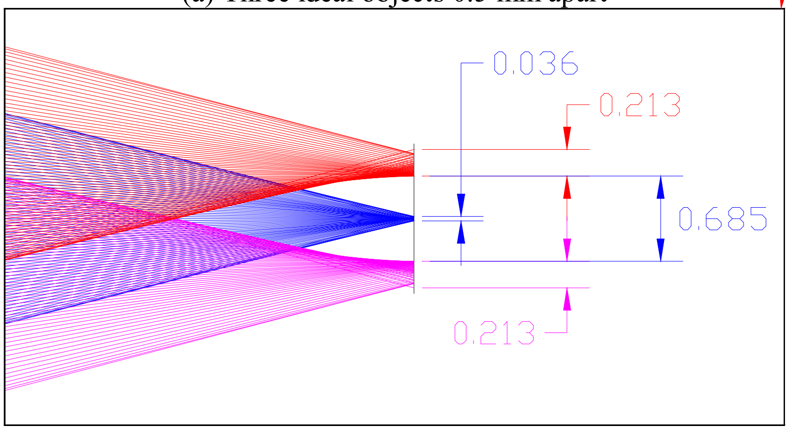

(b) Images of the three ideal objects

Figure 2.16 Ideal objects array and corresponding images (units are in mm) for the designed collection optical system

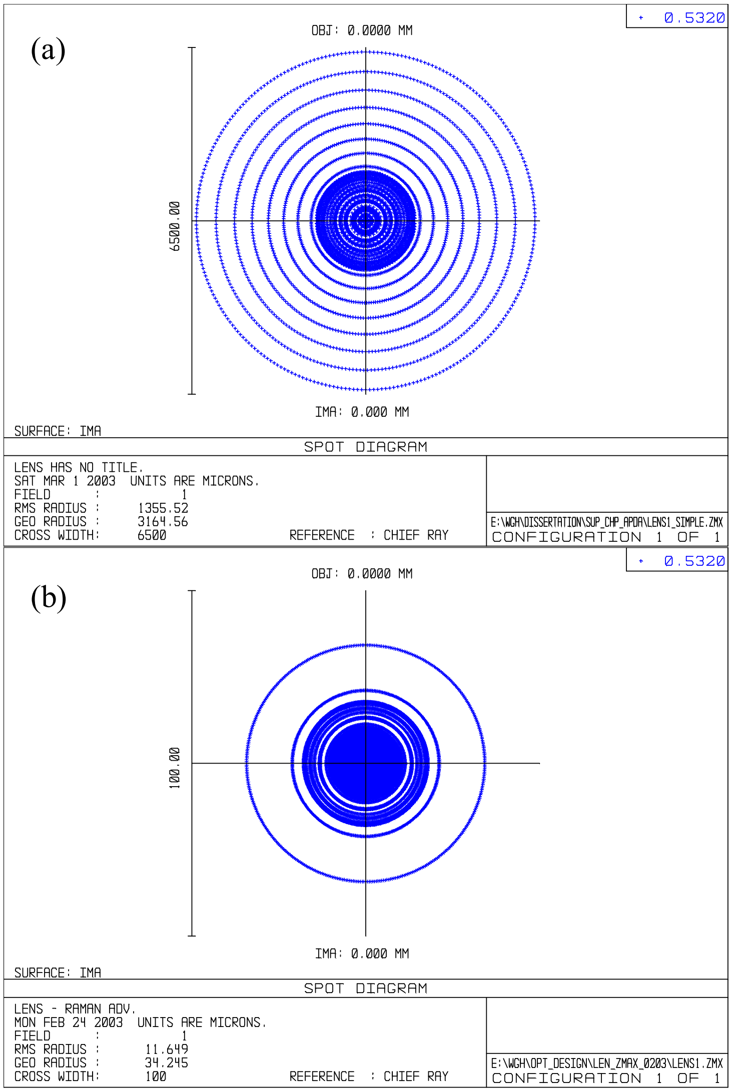

```
LENS HAS NO TITLE.
SAT MAR 1 2003  UNITS ARE MICRONS.
FIELD       :         1
RMS RADIUS  :   1355.52
GEO RADIUS  :   3164.56
CROSS WIDTH :   6500              REFERENCE  : CHIEF RAY
E:\WGH\DISSERTATION\SUP_CHP_APDA\LENS1_SIMPLE.ZMX
CONFIGURATION 1 OF 1
```

```
LENS - RAMAN ADV.
MON FEB 24 2003  UNITS ARE MICRONS.
FIELD       :         1
RMS RADIUS  :    11.649
GEO RADIUS  :    34.245
CROSS WIDTH :    100              REFERENCE  : CHIEF RAY
E:\WGH\OPT_DESIGN\LEN_ZMAX_0203\LENS1.ZMX
CONFIGURATION 1 OF 1
```

Figure 2.17 Spot diagrams (a) before, and (b) after, spherical aberration correction

The objective of the design is to get large enough collection solid angle with acceptable spatial resolution. The large solid angle is achieved by using a pair of large Plano-convex lenses (145 mm in diameter) with back to back placement. However, the resulting spherical aberration is very large so that the focal spot diameter is about 6.3 mm as shown in Figure 2.17 (a). The key in the design is to balance aberration from all surfaces such that the total aberration sums to zero or very close zero. One of the performance parameters to evaluate the total spherical aberration is the longitudinal spherical aberration (LSA) which is defined as (Smith, 2000)

$$LSA = k_{ac} f / f\#^2 \tag{2.9}$$

where k_{ac} is the aberration coefficient which depends of the shape of lens and the orientation. The total LSA of a multi-component lens system is then

$$LSA_s = \sum_i k_{ac} f / f\#^2 \tag{2.10}$$

A positive lens will generally contribute under-corrected spherical aberration, and a negative lens will contribute over-corrected spherical aberration. For a given aperture and focal length, the amount of spherical aberration in a simple lens is a function of object position and the shape of the lens. A meniscus lens has much more spherical aberration comparing to the plano-convex or bi-convex lenses. Therefore, a meniscus lens can be used to balance the under-corrected spherical aberration introduced by the first two large plano-convex lenses. Adding correction lenses, one meniscus lens and one bi-convex lens, the spherical aberrations are balanced and corrected as shown in Fig 2.17 (b) and the spot size is reduced to less than 68 μm. The whole setup is optimized at 532 nm using ZEMAX.

The effective *f#* is 2.4 and the corresponding solid angle is:

$$\Omega = 2\pi\left\{1 - \cos\left[\tan^{-1}\left(1/2f\#\right)\right]\right\} = 0.132 \tag{2.11}$$

Each lens surface has a broadband anti-reflection coating with transmission efficiency of 99.5%. For each lens, light will pass through two surfaces and lens body. The total collection efficiency for four-lens system is:

$$\eta = (T_s T_b T_s)^4 = (0.995 \times 0.995 \times 0.995)^4 = 0.94 \qquad (2.12)$$

The measurement volume, defined by the 0.2 mm entrance slit to the photomultiplier tube and the laser beam diameter, was 0.3 mm.

2.1.3.2 Two-point collection setup

In the experiments, a two-point setup is used to make gradient and dissipation measurements. In the setup shown in Fig. 2.18, a 50.8 mm, 50/50 beam cube splitter (Melles Griot model 03BSC015) was used to define the two adjacent points. There was a slit before each PMT to define the spatial resolution. The slit for PMT2 was mounted on a translational stage with 1 micron resolution (Newport model 433). The whole setup was then mounted on a precision lab jack (Edmund Industrial Optics model NT54-687) with vertical resolution of 1 mm per revolution. A 2-D mill table (Dayton model 6Z849) with movement resolution of 1 mm per revolution was used to move the whole setup in the horizontal plane as shown in Fig. 2.19.

Two-point measurements were made by imaging the scattered light onto a broadband hybrid cube beam splitter, which reflected and transmitted the split signal onto two different PMTs. Two 200 μm slits were placed in front of the PMTs to define the spatial resolution (i.e., length of the beam imaged). The slit width in the image plane corresponded to 300 μm in the object plane. These two slits were arranged such that the separation of probe volumes in the flow was 300 μm.

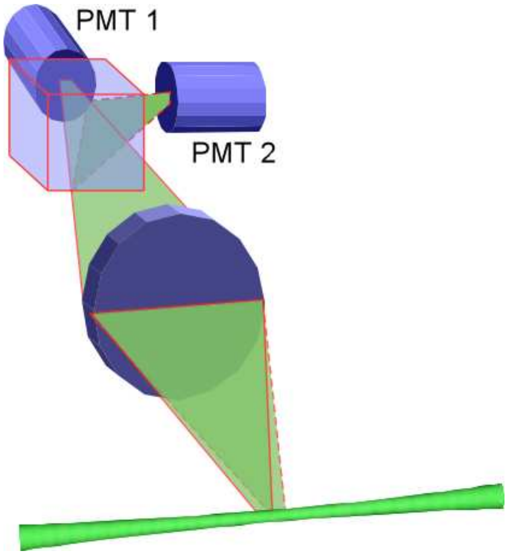

Figure 2.18 Two-point setup using 50/50 beam cube splitter

This two-point arrangement is verified by scanning a thin wire (wire diameter was 50 μm) across the field of view of the collection optics as shown in Fig. 2.20. Two curves "PMT1" and "PMT2" (solid symbols) represent two PMT readings when they were overlapped, the remaining two curves (open symbols) represent two PMT readings when they were separated by 200 μm in the image plane. Results for "PMT1" and "PMT1 Separated" were the same, which indicates the repeatability of the measurement. It can be seen from the measurement that the $\mathrm{FWHM}_{\mathrm{PMT1}}$ = 285 μm, $\mathrm{FWHM}_{\mathrm{PMT2}}$ = 300 μm and the separation between "PMT1" and "PMT2 Moved" was 320 μm.

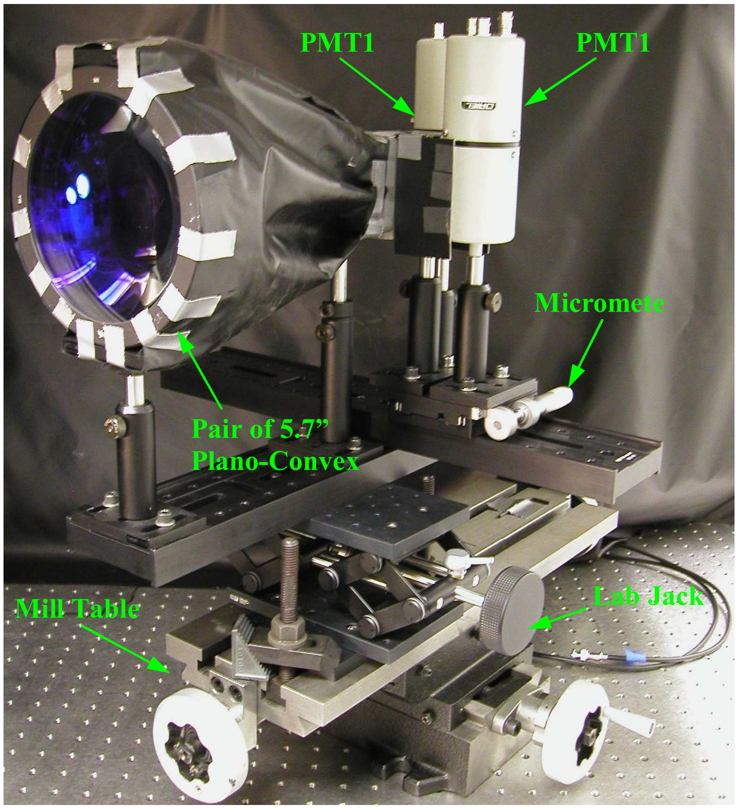

Figure 2.19 Setup of the collection optics

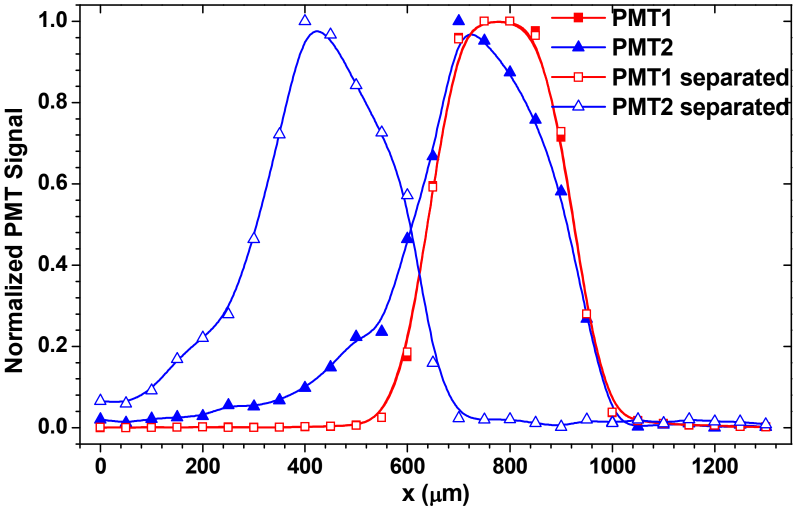

Figure 2.20 Verification of two-point resolution by the scanning wire technique

Analogous to the flow imaging experiments, the slit width corresponds to the so-called “pixel-resolution” and the separation between these two slits represents the physical resolution determined by the lens blurring effects. From the scanning wire technique, the spatial resolution was determined to be about 300 μm.

Another way to do two-point measurements is to use two separate channels instead of the beam cube splitter as shown in Fig. 2.21. This may be preferable because the beam splitter causes at least 50% light loss to each channel. Using two separated channels will increase the SNR by a factor of 1.4 for shot-noise limited experiments.

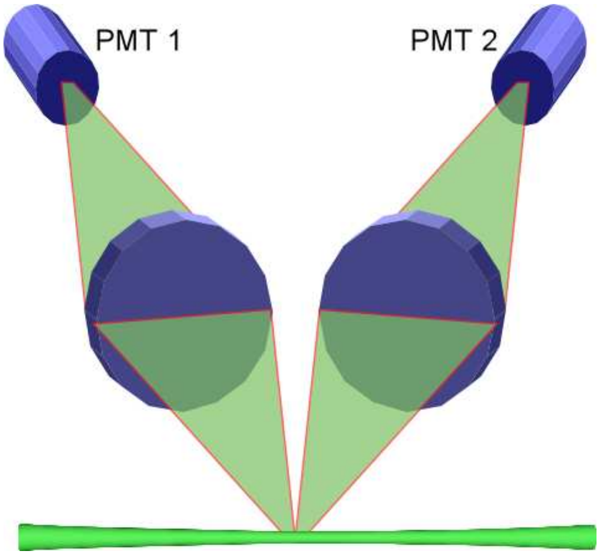

Figure 2.21 Two-point setup using two separate channels

2.1.4 Photo-detectors

2.1.4.1 Photomultiplier Tubes (PMT)

Photomultiplier tubes (PMTs) are extremely sensitive photon detectors, which under certain conditions can detect single photons. Light incident on the photo-emissive cathode (photocathode), will cause the emission of electrons from the surface if the photon energy exceeds the work function of the material. The emitted photoelectrons are then accelerated through a potential into an electron multiplier chain, which consists of a series of secondary electron emitting electrodes (dynodes). At a dynode, each impinging electron liberates several secondary electrons. The final electrode is the anode, typically connected to ground through a low impedance. The electron flow through the anode resistor produces a signal voltage proportional to the photon flux impinging on the tube.

The probabilistic nature of photon flux on the photocathode and the photocathode emission process introduces noise into the detection process. The photoelectron statistics are more realistically modeled by a random rate and can be described by Poisson statistics. The SNR of a PMT (Yariv, 1991) is defined as:

$$SNR_P = \frac{(GI_s)^2}{2eG^2 I_k \Delta f \frac{1}{1-\delta^{-1}} + \frac{kT\Delta f}{R_L}} \tag{2.13}$$

Where I_k is total current of photo-cathode ($I_k = I_s + I_d$), I_s is the signal current caused by incident light ($I_s = e\eta_{\det}\Gamma_\phi$), I_d is the dark current of PMT, η_{det} is the quantum efficiency of PMT, Γ_ϕ is the photo flux per pulse, G is the gain of PMT, T is the Temperature, Δf is the detection bandwidth, δ is the secondary emission ratio of the PMT (about 6), R_L is the load resistor (50Ω), e is the electron charge (1.602×10^{-19}C), and k is Boltzmann's constant (1.38×10^{-23}J/K)

The first noise term in the denominator is due to the amplified photocathode shot noise. The second noise term is the thermal noise. Some assumptions can be made to simplify this equation:

1) If the thermal noise (Johnson noise) is very small or the gain is large enough, the shot noise will be much larger than the thermal noise and term $kT\Delta f / R_L$ in the denominator can be neglected. This is the so-called "*shot-noise limit*". Measurements with PMTs are usually made at this limit.

2) Dark current is small compared to signal current, $I_d << I_s$ then $I_s \approx I_k$ and dynode shot noise can be ignored, since $\delta \sim 6$, and $(1-\delta^{-1}) \sim 1$,

$$SNR_P = \frac{\eta_{\det}\Gamma_\phi}{2\Delta f} \tag{2.14}$$

3) For bandwidth $\Delta f = 1$Hz;

$$SNR_P = \eta_{\det}\Gamma_\phi / 2 \tag{2.15}$$

4) This SNR_P is for the power measured. If we consider the measured current then the corresponding SNR is:

$$SNR_I = \sqrt{\eta_{\det}\Gamma_\phi / 2} \tag{2.16}$$

The consideration of choosing a particular PMT depends on several factors, i.e. the quantum efficiency in the working wavelength range, effective gain, response time, the dark noise etc. Based on these considerations, the Hamamatsu R636-10 and H7422-40 PMTs have been chosen for the present measurements. Some characteristic performance parameters are listed in Table 2.3

(Hamamatsu PMT manual). The high gain and high quantum efficiency in the visible wavelength range are especially useful for the current experiments.

Table 2.3 Summary of R636-10 and H7422-40 PMT characteristics

Characteristic	R636-10	H7422-40
Quantum Efficiency (%) at 532 nm	16	40
Rise time (ns)	1	2
Photocathode	GaAs (Cs)	GaAsP
Cathode Radiant Sensitivity (mA/W)	63	176
Anode Radiant Sensitivity (A/W)	2.8×10^4	8.8×10^4
Anode Dark Current (nA)	0.1 (Typ.) 2.0 (Max.)	0.4 (Typ.) 1.0 (Max.)

2.1.4.2 Multi-channel high voltage power supply system

The high voltage multi-channel PMT power supply (EMCO Octo-Channel) is controlled by a NI 6703 DAQ board. The NI 6703 DAQ board has a PCI interface with the host computer and 16 channel outputs with 16 bit dynamic range. The output range was from –10.1V to 10.1V with an absolute accuracy of ±1mV. A 68 pin cable was used to connect the 6703 DAQ board to the SCB68 connector box. A 25pin cable connected the SCB68 connector box with the EMCO high voltage power supply. Since the NI 6703 DAQ has no analog inputs, the system was basically an open loop control system. The pin connection from NI 6703 DAQ board to the Octo-channel high voltage power is shown in Fig 2.22.

The octo-channel high voltage system provided eight programmable high voltage outputs and each channel was independently regulated to maintain a stable output voltage. Each regulated output was referenced to the programming voltage for that channel, and had a voltage monitor which was a direct sampling of the high voltage output in a 1000:1 ratio. The programming input voltage range was from 0V to 5V and the negative voltage output range of the octo-channel power supply was 0V to –1500V. Therefore, 1V outputs from the NI 6703 corresponded to –300V high voltage output from the octo-channel power supply. For example, if the required output is –1000V then the output from the NI 6703 should be set to –1000/–300 = 3.33V.

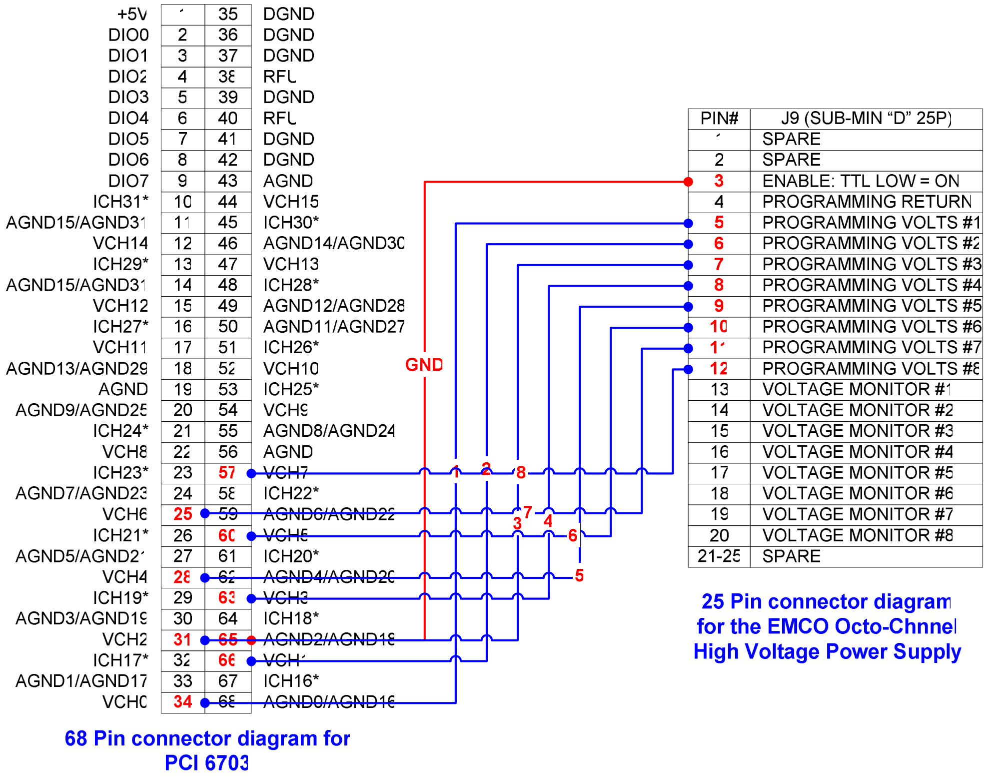

Figure 2.22 Multi-channel PMT power supply implementation

2.1.5 Multi-channel data acquisition (DAQ) system

2.1.5.1 Multi-channel gated integrator

The boxcar and gated integrator is from Stanford research systems (model SR250). The SR250 gated integrator is a NIM format gated integrator/boxcar averager which has a gate generator and fast gated integrator with averaging circuitry. It is designed for recovering fast analog signals from noisy backgrounds and is useful for pulsed laser experiments by rejecting the background and flame luminosity signals when there is no laser light. The instantaneous pulse to pulse outputs from PMT and photodiode were integrated by SR250. The boxcar integrates a sample and hold to provide an output that is a series of piece-wise continuous step functions. The DAQ board actually samples these “step-like signals”.

Three SR250s were used in the experiments for two PMTs and one photodiode. Gate widths were 300 ns. Shot by shot output was used instead of the average signal to capture the instantaneous signal from a single laser pulse. Gate outputs were monitored on two oscilloscopes to get precise gate timing, i.e. matching of the gate with the signal position. The SRS250 is triggered at 10 kHz by the DG535 pulse/delay generator. The delay time for each channel was about 150 μs.

2.1.5.2 Multi-channel DAQ

The integrated outputs of the PMTs and photodiode signals from the gated integrator are digitized using an analog-to-digital converter (NI-PCI-MIO-16E-1, specification listed in Table 2.4).

Digitized signals were read and stored on computer disk. Laser power and the background signal level were recorded at each measurement location, and corrections for any variations in these were applied during the data-reduction procedure. The maximum data rate is 1.25 M Samples/s depending on the number of channels used. The practical sampling rate was limited by the maximum repetition rate of the laser, which is 25 kHz. The acquisition time mainly depends on the experimental requirement and computer memory.

Table 2.4 Specifications for NI-PCI-MIO-16E-1 A/D card

Analog Input	Number of Channel	16 single-ended or 8 differential channels
	Sampling Rate	1.25 MS/s, 1.25 MS/s stream-to-disk rate
	Resolution	12-bit
	Input Range	±0.05V ~ ±10V
Analog Output	Number of Channel	2 analog outputs;
	Output Rate	1.0 MS/s
	Resolution	12-bit
Digital I/O		8
Counter and Timers		2 Channel, 24-bit
Trigger		Analog and digital

2.1.6 LabVIEW programs

The experiment was controlled with a LabVIEW program. The main LabVIEW virtual interface (VI), shown in Fig 2.23, has several subroutines: multi-channel data acquisition (DAQ) subroutine, two-dimensional linear translation control subroutine, fuel metering monitor subroutine and multi-channel high voltage control subroutine. The multi-channel DAQ, 2D linear translation and fuel metering monitor subroutines are integrated together to scan and sample the data.

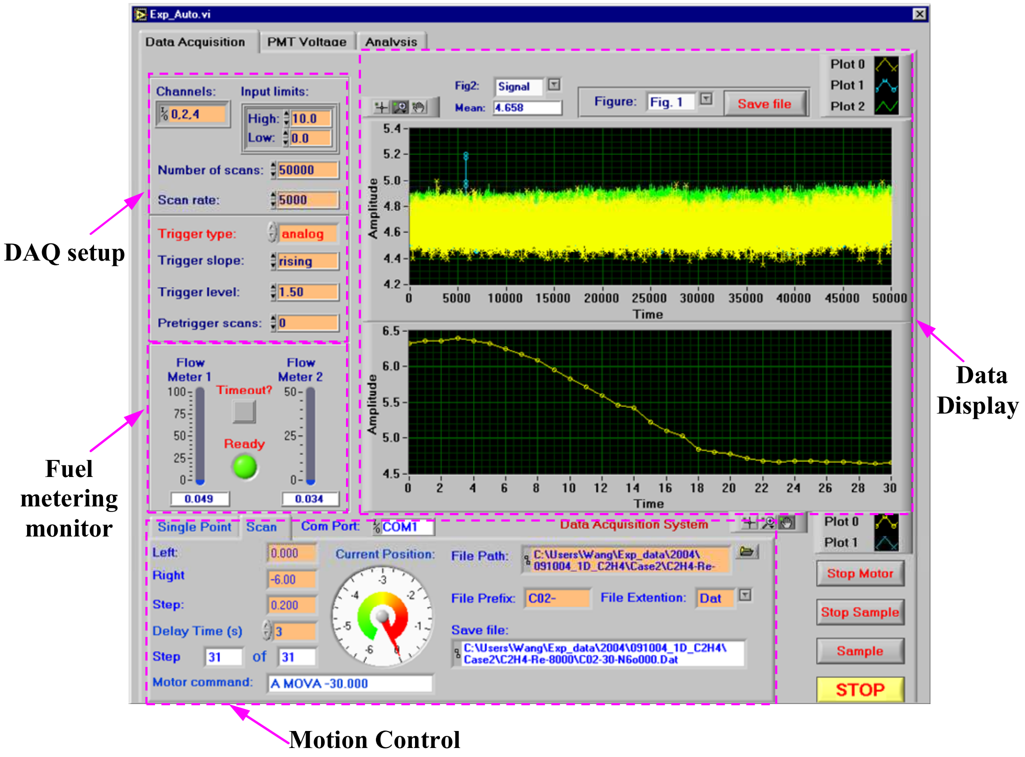

Channels: 0,2,4

Input limits: High: 10.0 Low: 0.0

Number of scans: 50000

Scan rate: 5000

Trigger type: analog

Trigger slope: rising

Trigger level: 1.50

Pretrigger scans: 0

Fig2: Signal

Mean: 4.658

Figure: Fig. 1

Flow Meter 1: 0.049

Flow Meter 2: 0.034

Com Port: COM1

Left: 0.000

Right -6.00

Step: 0.200

Delay Time (s) 3

Step 31 of 31

Motor command: A MOVA -30.000

File Path: C:\Users\Wang\Exp_data\2004\091004_1D_C2H4\Case2\C2H4-Re-

File Prefix: C02-

File Extention: Dat

Save file: C:\Users\Wang\Exp_data\2004\091004_1D_C2H4\Case2\C2H4-Re-8000\C02-30-N6o000.Dat

Figure 2.23 LabVIEW VI for data acquisition (DAQ), motion control, flow rate monitoring programs

The DAQ parameters are set by the top-left panel whose values are determined by specific experiments. These parameters include DAQ channels and order of scan, sampling frequency, number of samples (acquisition time), the expected max/min input voltage levels, triggering mode and level. The “Trigger Type” could determine whether the DAQ is in free-run mode or externally triggered by other hardware, e.g. SR250 gated integrator or DG 535 pulse/delay generator. In the current experiment, the DAQ is synchronized by the DG 535.

The middle-left panel is the fuel metering monitors which can show fuel flow rates of two fuels at a time. It can also be expanded to display three fuel flow rates at a time. This was only used for monitoring purposes and the flow rate values were not sampled in the experiments.

All configurations for the stepper motor are shown in the bottom panel in Fig. 2.23. For most point-wise experiments, one has to scan a line or even 2-D plane to collect data. Therefore, this motor control program was incorporated into the DAQ program. The data acquisition and motor control is run using the following procedure:

- Move to the LEFT end
- Hold for some time
- Acquire data and save data file 1
- Move to the next position
- Hold for some time
- Acquire data and save data file 2
- ……
- Move to the RIGHT position
- Hold for some time
- Acquire data and save data file n
- Move to the original staring position

The "Delay Time" must be set to allow for the time required for the translation system to move and stabilize at the next position and the time for the DAQ program to store all data to the hard disk.

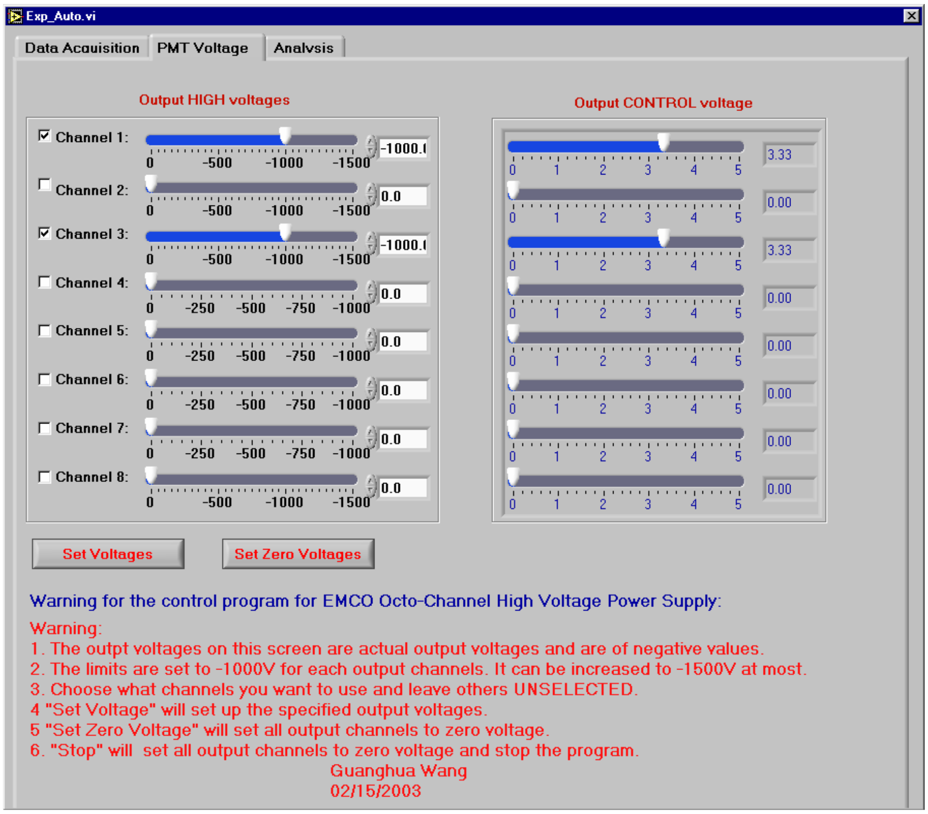

☑ Channel 1: -1000.
☐ Channel 2: 0.0
☑ Channel 3: -1000.
☐ Channel 4: 0.0
☐ Channel 5: 0.0
☐ Channel 6: 0.0
☐ Channel 7: 0.0
☐ Channel 8: 0.0

3.33
0.00
3.33
0.00
0.00
0.00
0.00
0.00

Warning for the control program for EMCO Octo-Channel High Voltage Power Supply:

Warning:
1. The outpt voltages on this screen are actual output voltages and are of negative values.
2. The limits are set to -1000V for each output channels. It can be increased to -1500V at most.
3. Choose what channels you want to use and leave others UNSELECTED.
4 "Set Voltage" will set up the specified output voltages.
5 "Set Zero Voltage" will set all output channels to zero voltage.
6. "Stop" will set all output channels to zero voltage and stop the program.

Guanghua Wang
02/15/2003

Figure 2.24 LabVIEW GUI for multi-channel PMT power supply control program

The multi-channel PMT power supply control GUI setup is shown in Fig. 2.24. The left hand panel is the setup output voltage in negative values. The maximum output of the EMCO octo-channel power supply is –1500V which is set as the upper limit of the slider bar. To get an output voltage, there must be a specified output voltage and the left check box must be selected as well. Without selecting the check box, the output voltage from the power supply is zero even if the slider bar is set to some value. This is just a double-check setup to prevent accidental damage to PMTs. After confirming the desired output voltages, “Set

Voltage" button was pressed to enable the output voltages. To disable the PMTs, the "Set Zero Voltage" button was pressed, which sets all output voltages of all channels to zero.

The right panel shows the corresponding output voltage from the NI 6703 D/A cards and their units are in volts. As discussed earlier, the mapping between the programming voltage to the real negative output is 5 V to –1500 V. Therefore, –1000V requires a 3.33V output from the NI 6703 D/A card.

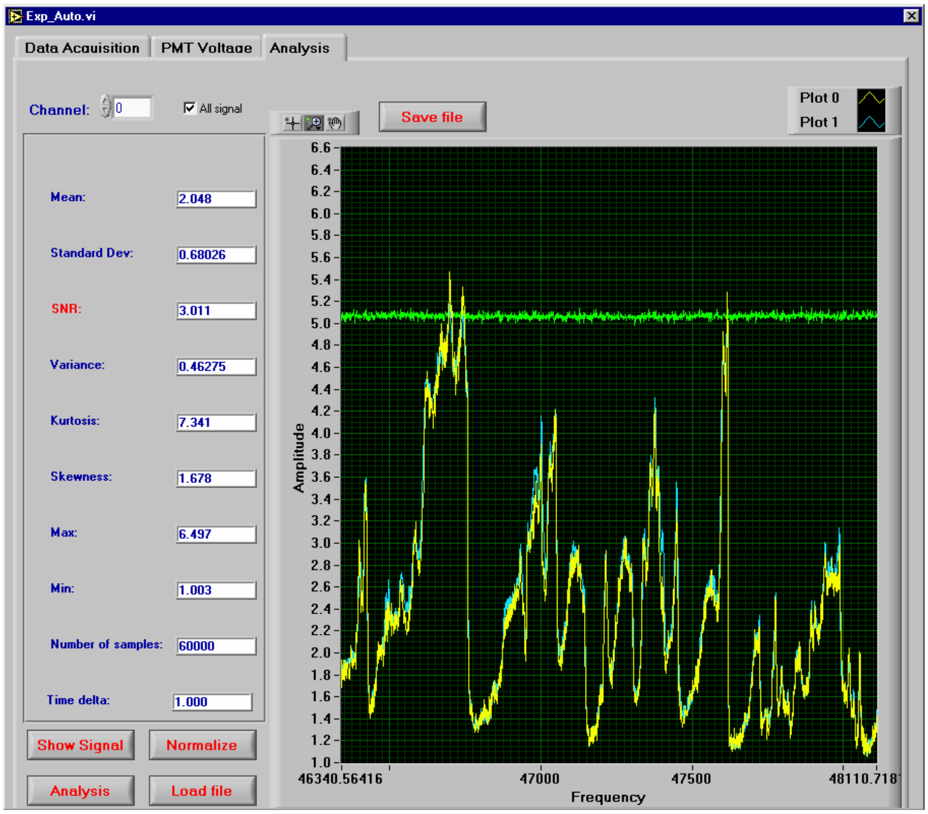

Channel: 0
☑ All signal
Mean: 2.048
Standard Dev: 0.68026
SNR: 3.011
Variance: 0.46275
Kurtosis: 7.341
Skewness: 1.678
Max: 6.497
Min: 1.003
Number of samples: 60000
Time delta: 1.000

Figure 2.25 LabView GUI for data analysis

The "Data Analysis" GUI, shown in Fig. 2.25, can do some simple statistical analysis of the experimental data. It can display single channel data and the corresponding statistical values, e.g. mean, standard deviation, Signal-to-Noise-Ratio (SNR), skewness, kurtosis etc. The motivation for including this subroutine in the main GUI is to do a quick check of the experimental data and adjust hardware setup if necessary.

The running procedure is summarized as follows:

1) Setup the PMT voltages from the GUI. The setup voltage is the actual output voltage in Volts (< 0).

2) Setup data acquisition (DAQ) parameters, i.e. sampling frequency, number of samples (acquisition time), the expected max/min input voltage levels, triggering mode and level.

3) Setup the 2-D translation system parameters, i.e. start position, end position, step size and delay time. All position and step units are in inches.

4) Press “Sample” button to start the data acquisition.

5) Press “Stop” button to stop the whole program. Before exiting the program, the output voltage of the NI 6703 DAQ board will be set to zero outputs automatically. This protects PMTs from accidental exposure to high light level.

2.2 DATA REDUCTION

2.2.1 Laser Rayleigh thermometry

Rayleigh scattering has been used to measure concentration, temperature, and density, e.g. Zhao and Hiroyasu (1993), Miles et al. (2001) and Stricker (2002). The differential cross section for Rayleigh scattering by gas molecules is given by:

$$\sigma = \frac{2\pi^2 (\mu_0 - 1)^2}{N_0 \lambda^4} \tag{2.17}$$

where μ_0 is the index of refraction of the gas at STP, λ is the laser wavelength, N_0 is Loschmidt's number ($2.69\times10^{19}/\text{cm}^3$), and a 90-deg scattering angle is assumed. The light intensity I_R that is scattered by a mixture of gases, with each species having a number density n_i and differential cross section σ_i, is given by:

$$I_R = K\sum n_i\sigma_i = Kn\sum x_i\sigma_i = Kn\sigma_{eff} \tag{2.18}$$

where x_i is the mole fraction of species i and n is the total number density. K is a parameter proportional to the laser intensity, the collection solid angle, and the length of beam imaged on the detector and is determined by calibration. σ_{eff} is the effective Rayleigh cross-section of the mixture in the probe volume which is the sum of the component cross-sections weighted by the component mole fractions

$$\sigma_{eff} = \sum x_i\sigma_i \, , \tag{2.19}$$

The measured Rayleigh signal S_R is defined here as the total charge collected on the Rayleigh PMT during a single laser pulse. The signal has several contributed factors as shown by the equations below

$$S_R = I_R + B + DC \, , \tag{2.20}$$

where I_R is the Rayleigh signal, B is the contribution from background scattering and luminosity, and DC is the integrated dark current of molecules in the probe volume of the PMT. The Rayleigh signal I_R is proportional to the total molecular number density. Because of the high polarization ratio of the current laser system (>1000:1), the background and dark count can be measured by rotating the beam polarization by 90°. Therefore, measured signals before and after rotating the polarization will be

$$S_{R,\perp} = I_{R,\perp} + B + DC \, , \tag{2.21}$$

$$S_{R,//} = I_{R,//} + B + DC \, , \tag{2.22}$$

where $\perp$ denotes the signal before the rotation of the polarization angle (s-polarized scattering light) and // denotes that after the rotation (p-polarized scattering light). In the above formula, the background scattering and dark current of the PMT were assumed the same during the rotation of the laser beam polarization. Because of the high polarization ratio $I_{R,\perp} > 1000\, I_{R,//}$, the Rayleigh signal I_R can be calculated as

$$I_R = S_{R,\perp} - S_{R,//} = I_{R,\perp} - I_{R,//} \approx I_{R,\perp} \, . \tag{2.23}$$

The temperature was then obtained from the Rayleigh signal I_R by using

$$T = K_R \sigma_{eff} \big/ I_R \, , \tag{2.24}$$

where K_R is a calibration constant.

The fuel composition used in this study was 22.1% CH_4, 33.2% H_2, 44.7% N_2 (by volume), which gives a stoichiometric mixture fraction of 0.167. The Rayleigh cross-section of this fuel has been shown to vary by ±3% across the whole flame (Bergmann et al. 1998). For constant effective Rayleigh cross section, the temperature was derived even more simply from

$$T = I_{ref} T_{ref} \big/ I_R \, , \tag{2.25}$$

where $I_{R,ref}$ is the reference Rayleigh scattering signal from air at room temperature (T_{ref}).

2.2.2 Gradient and dissipation calculation

The two-point instantaneous temperature signals were used to determine the instantaneous radial temperature gradient by using the approximation

$$\partial T/\partial r = \Delta T/\Delta r = [T(r+\Delta r,t) - T(r,t)]/\Delta r\,, \tag{2.26}$$

where ΔT is the temperature difference of the two measurements and $\Delta r = 300$ μm was the probe separation distance. The axial gradient was estimated from the time-series and Taylor's hypothesis:

$$\partial T/\partial x = -(1/\overline{U})\,\Delta T/\Delta t = -(1/\overline{U})[T(r,t+\Delta t) - T(r,t-\Delta t)]/2\Delta t \tag{2.27}$$

where $\overline{U}$ is the mean local velocity obtained from Schneider et al. (2003) and as reported in TNF database. The precision uncertainties of the mean velocities were estimated to be below 5%, whereas fluctuations were accurate to within 10% (Schneider et al. 2003). The error in using Taylor's hypothesis is estimated to be about 10% at the jet centerline in non-reacting jet flows by Mi and Antonia (1994a) and Dahm and Southerland (1997). The error in using Taylor hypothesis increases away from the centerline; therefore, the axial gradient and the 2-D dissipation components are evaluated along the centerline only. For convenience, the thermal dissipation based on single component of the gradient vector are also defined

Axial component: $$\chi_{T,x} = 2\alpha(T)\,\overline{U}^{-2}\,(\partial T/\partial t)^2\,, \tag{2.28}$$

Radial component: $$\chi_{T,r} = 2\alpha(T)\,(\partial T/\partial r)^2\,, \tag{2.29}$$

2-D Planar component: $$\chi_{T,p} = \chi_{T,r} + \chi_{T,x}\,. \tag{2.30}$$

Chapter 3. Scalar dissipation measurement model

3.1 INTRODUCTION

For most scalar gradient and dissipation measurements, the effects of resolution and noise are coupled and they tend to act in opposite directions. Finite resolution will always result in the measured scalar dissipation rate under-predicting the true value. Conversely, the effect of noise is to make the measured dissipation rate larger than the true value. These effects make the assessment of the experimental accuracy in dissipation measurements extremely difficult to achieve. In practical laser diagnostics experiments, increased SNR is usually achieved by sacrificing resolution, i.e., by reducing the bandwidth or averaging over a larger probe volume. This implies that in any actual measurements a balance must be reached between the two factors of resolution and noise.

In the current two-point time-series experiments, several practical issues must be considered. Firstly, there is the spatial resolution of the collection optics, which is determined by the slit width, magnification and blur induced by the collection optics. The resolution is set by the blurred slit that is projected into the flow. Secondly, the resolution is affected by the distance between the two measurement points. Here, both the geometric resolution and the blurring of the collection optics must be considered. Thirdly, resolution is limited by the laser beam diameter, which is determined by the characteristics of the focusing optics and the M^2 of the laser beam as discussed in Chapter 2. For time-series experiments, the sampling frequency of the DAQ system should also be considered. As will be discussed in Chapter 4, this sampling frequency should be at least twice the Batchelor frequency. Noise will create an apparent dissipation (i.e., bias error), which will be more significant at small spatial resolution, as discussed by Mi and Antonia (1994b). For Rayleigh scattering measurements in reacting flows, signal levels will be about 5-7 times lower than those in corresponding non-reacting flows; thus, these noise effects will be even more significant in reacting flows.

A major accomplishment of this work was the development of a system-level model to account for the effects of resolution, noise, filtering and data processing on the measured dissipation. Assumptions for the experimental noise are also discussed and their effects on the measured scalar dissipation are illustrated. For the current two-point time-series thermal dissipation measurements, techniques to correct the measured mean dissipation for this bias are also developed. The first technique uses the noise floor information in the Power Spectral Density (PSD) to calculate the apparent dissipation. This technique extended the PSD noise correction methods used by Renfro et al. (1999, 2000). A calculation procedure was provided to guide the data processing code.

In turbulent nonpremixed jet flames, the Batchelor scale is relatively large compared to the corresponding non-reacting jet flow at the same jet exit Reynolds number due to the heat release effect. However, the convection velocity will be higher than that of the equivalent non-reacting jet because heat release reduces the decay of the centerline velocity. The net effect is that the convective Batchelor frequency tends to be higher in turbulent nonpremixed jet flames than in non-reacting jets. This makes fully temporally resolved measurements in the jet flame near-field difficult to achieve. In this case, the noise floor in the PSD can't be resolved as well, and the correction technique based on the PSD is no longer feasible.

To correct for the apparent dissipation due to noise in the near-field, a redundant measurement technique was developed. Here, the two measurement points must be made to coincide (i.e., measure the same spatial location), in which case the measured dissipation should be zero; however, the presence of noise will result in the measurement of an *apparent dissipation*. This measure of the apparent dissipation is assumed to be the same when the probes are separated by a distance that is the same order of magnitude as the estimated Batchelor scale. Experiments in this configuration yield the *measured dissipation*, which includes the *true dissipation* and *apparent dissipation* due to noise. Subtracting the noise dissipation from the measured dissipation gives the true dissipation. Results from the PSD correction technique and redundant measurement are compared in Chapter 4.

The corrected dissipation results motivated further consideration of the apparent dissipation in general laser diagnostics experiments. A generic technique to estimate the noise level for scalar dissipation measurement was developed, which can be used to estimate the minimum apparent dissipation due to noise. The predicted apparent dissipation is compared to results obtained by the PSD correction technique and the redundant measurement technique in Chapter 4.

3.2 THEORETICAL MODELING

Figure 3.1 shows the system model for the scalar dissipation measurement as inferred from the differentiation of a measured scalar profile *o(x)*. The model was developed for 1-D experiments but it can be easily extended to the 2-D imaging case. The system model is composed of five sub-models that represent the different processes used to obtain the measured dissipation. These sub-models are: measurement, post-processing, data reduction, gradient and dissipation. The data reduction sub-model is diagnostic-technique dependent and is not general; therefore, in the following discussion, it will be treated as a do-nothing model first and its function will be discussed in a later section.

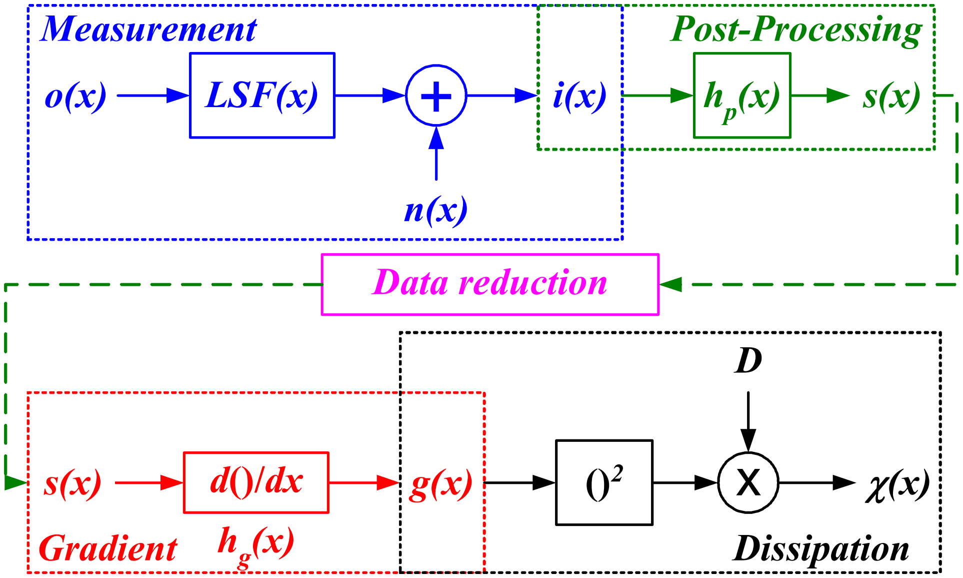

Figure 3.1 System model from scalar field *o(x)* to the calculated dissipation *χ(x)*

For 1-D linear operations, these sub-models can be expressed as:

Measurement: $$i(x) = LSF(x) * o(x) + n(x) \qquad (3.1)$$

Post-processing: $s(x) = h_p(x) * i(x)$ (3.2)

Gradient: $g(x) = h_g(x) * s(x)$ (3.3)

Dissipation: $\chi(x) = 2D(x) \cdot g(x)^2$ (3.4)

where $o(x)$ is the true scalar concentration profile, $LSF(x)$ is the collection optics Line Spread Function, $n(x)$ is the noise, $i(x)$ is the image or measured scalar concentration, $h_p(x)$ is the post-processing filter, $s(x)$ is the filtered data, $h_g(x)$ is the digital filter for $d(\,)/dx$ (i.e., the gradient calculation operator), $g(x)$ is the computed gradient, $\chi(x)$ is the corresponding computed scalar dissipation and D is the diffusivity.

The measurement sub-model includes the resolution and noise effects in the scalar dissipation experiments. The resolution is modeled as a convolution process and quantified by the Line-Spread-Function (LSF). The LSF was used instead of the Point-Spread-Function (PSF) because the gradient calculation is based on the two-point technique, which is essentially a 1-D measurement. The noise was modeled as an additive source. Poisson (shot) noise can be approximated as an additive random source whose variance is proportional to the signal intensity. The post-processing sub-model considers the effects of the post-processing filters, e.g. averaging, smoothing, low-pass filters etc. The gradient sub-model takes into account the effects of the differentiation stencils, e.g., first-order forward/backward and second-order central differencing. The dissipation sub-model mainly considers the issue of the calculation of the diffusivities. In reacting flows, where there are large temperature fluctuations, the errors in the diffusivity may have a more significant impact on the calculated scalar dissipation than errors in the gradient square term (Geyer et al. 2004).

It should be pointed out that all sub-models function simultaneously in scalar dissipation measurements. The purpose of dividing the system into different sub-models is to facilitate discussion of these effects.

3.2.1 Measurement sub-model

In the measurement sub-model (shown in Fig. 3.2), two important issues are considered, i.e. resolution and noise. The resolution is modeled as the convolution of the true scalar quantity *o(x)* with the *LSF(x)*. The ideal *LSF* is a δ-function in the spatial domain, in which case the object is faithfully reproduced at the image plane without blur.

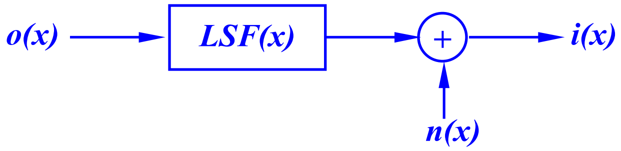

Figure 3.2 Dissipation system resolution and noise modeling

For most optics used in the flow imaging or point measurements, the *LSF* can be modeled as a low-pass filter. Experimental results of Turiskov (2002) and Wang and Clemens (2004) showed that a Gaussian function is a reasonable model of the *LSF* resulting from flow imaging optics, which do not tend to be diffraction limited. The Fourier transform of the *LSF* is the Modulation-Transfer-Function (*MTF*), which is generally used to quantify the optical system resolution. The 4% *MTF* or FWHM of the *LSF* are commonly used to determine the resolution of the optical system. In some applications, the blurring effects of the optical system can outweigh the pixel-resolution and hence determine the real resolution. A discussion of the *LSF* and its use in quantifying measurement resolution in flow imaging can be found in Clemens (2002) and Wang and Clemens (2004).

Here, additive noise is also included to represent shot-noise, readout noise and thermal noise, etc. Two noise models are generally used in the literature, i.e. Poisson noise and white Gaussian noise. They have fundamentally different characteristics. Gaussian noise, also known as white noise, is evenly distributed across the entire range of frequencies. Gaussian noise is usually appropriate when the noise originates primarily from the detector. In this case, the noise is often assumed to be independent of the signal and it is this type of noise that is most commonly used in analyses that aim to show the effect of noise on experimental measurements (e.g., Mi and Antonia, 1994b). The independence of the signal and noise is advantageous because most of the correlation terms between noise and signal vanish, which simplifies the analysis significantly.

However, for most optical based experiments, Poison noise is more appropriate. Scattered light is not a truly continuous quantity, and is collected as discrete photons that do not arrive in a perfectly steady stream. Discrete arrivals over a period of time are modeled statistically by a *Poisson* distribution. If the mean number of photons collected during the sampling time is μ, then for Poisson statistics the probability that m photons will be collected during the sampling time is given by

$$P(m;\mu) = \mu^m e^{-\mu} \big/ m! \tag{3.5}$$

The Poisson distribution has the following properties: (1) its variance is equal to its mean ($\sigma^2 = \mu$); (2) $SNR = \sigma/\mu = 1/\sqrt{\mu}$ and hence, increasing the mean photon count reduces the effect of Poisson noise in the measured signal.

3.2.2 Post-Processing filters

For most experiments, post-processing filters, such as smoothing filters, are commonly used to improve the signal quality. Using linear post-processing filters, the post-processed signal *s(x)* is:

$$s = h_p * i = h_p * (LSF * o + n) = h_p * LSF * o + h_p * n \tag{3.6}$$

where h_p is an averaging or smoothing filter. This process is shown schematically in Fig. 3.3.

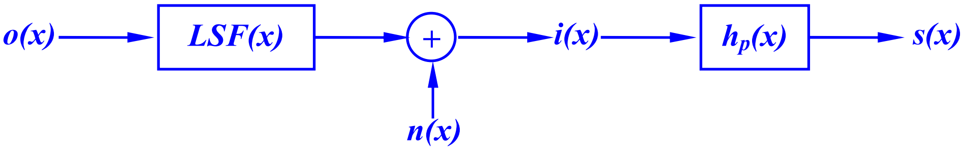

Figure 3.3 Modeling of the post-processing filter

The post-processing filter is generally low-pass in nature which removes high-frequency noise. If the post-processing filter works so well that noise is no longer significant, one gets:

$$s \approx h_p * LSF * o\,. \tag{3.7}$$

Introducing the *apparent* Line-Spread-Function LSF_a:

$$LSF_a = h_p * LSF\,, \tag{3.8}$$

the post-processed signal *s(x)* will be:

$$s = LSF_a * o\,. \tag{3.9}$$

This actually reduces to an even simpler model as shown in Fig. 3.4.

Figure 3.4 Simplified model for post-processing filter that uses the "apparent LSF" to account for noise effects

The pixel binning technique is easy to implement experimentally, but insufficient attention has been paid to the artifacts it creates, especially when calculating gradient related quantities. Imaging with an array is a process that both averages over a pixel and samples the spatial frequency content of the object. Pixel binning affects both of these processes as well as reducing the noise content of the signal. The pixel binning can be modeled as a digital post-processing filter as shown in Fig. 3.5.

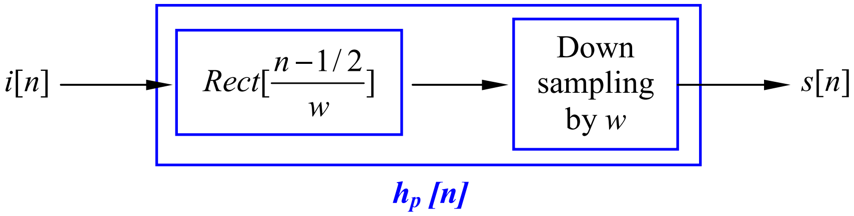

Figure 3.5 Model of $h_p[n]$ for the pixel binning effect

The digital image $i[n]$ is filtered by the rectangle spatial filter *Rect* (essentially an average filter) and then down sampled by a factor of w which is the width of the binning window. The Rectangle-filter *Rect* causes significant frequency leakage in the frequency domain.

3.2.3 Combined effects of resolution and noise

For the filtered signal *s(x)*, all the analysis and results presented in Wang and Clemens (2004) can be applied. Here, the noise issue is essentially transferred to the resolution issue. In other words, if the noise effect cannot be determined and corrected, it can be removed by the post-processing filters at the expense of resolution. This may be a useful tradeoff as in some cases it is possible to correct the image for the effects of blur (Molina et al., 2001). The concept of the apparent *LSF* is also useful, because it emphasizes that when the signal is noisy, the effective resolution may not be as good as the user believes.

In real scalar dissipation experiments, finite resolution will always result in the measured scalar dissipation rate under-predicting the true value. Conversely, the effect of noise is to make the measured dissipation rate larger than the true value. The combined effect of resolution and noise makes the assessment of the experimental accuracy in dissipation measurements extremely hard.

For ideal fully-resolved and noise-free scalar dissipation measurements, the measurement error curve is like the black line in Fig. 3.6, which is similar to the measurement error curve in Fig. 2 of Mi and Nathan (2003). Figure 3.6 shows that there is no measurement error when the spatial resolution is smaller than or equal to the Batchelor scale. However, if there is noise in the signal, no matter what the magnitude of the noise level, the ratio of the measured to the true scalar dissipation grows without bound as the spatial resolution becomes higher, i.e. $\lambda_r \to 0$. This is discussed by Mi and Antonia (1994b) as will be discussed in detail in section 3.3. This is the *noise dominant regime* where the measured scalar dissipation is always higher than the true scalar dissipation and error generally increases with increasing noise level as illustrated in Fig. 3.6.

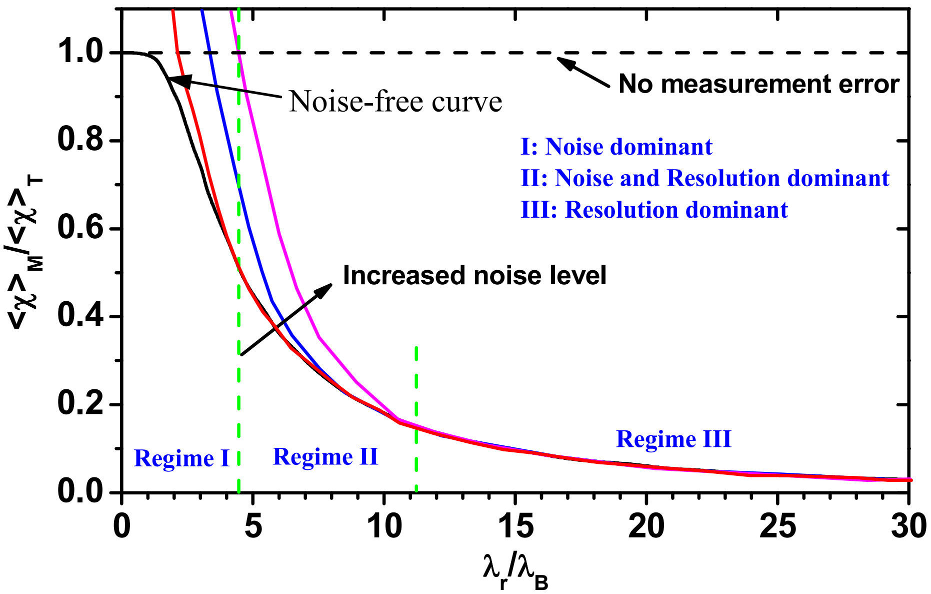

Figure 3.6 Illustration of correlated effects of resolution and noise in the scalar dissipation measurement

In the *noise and resolution dominant regime*, the effects of finite resolution and noise compete with each other to determine the measurement error. Interestingly, the measurement error is smaller compared to the noise-free (i.e., resolution only) error curve as shown in Fig. 3.6. This implies that at moderate resolution and moderate noise level, the measurement accuracy is actually improved by the presence of noise. This seemingly counter-intuitive result is because noise adds an apparent (false) dissipation that makes up for the attenuated dissipation resulting from finite resolution. It may not be a useful strategy to try to improve the accuracy of a dissipation measurement by working in this regime because it is hard to know the noise level in actual experiments and so the accuracy would be difficult to determine.

At lower probe resolution (higher λ_r), the averaging is so significant that the noise is not important at all. This is the *resolution-dominant regime*. In this case, the error curve collapses to the noise-free error curve, regardless of the SNR. Figure 3.6 clearly illustrates this intricate relation between resolution and noise in the scalar dissipation measurement.

3.2.4 Gradient calculation

In order to compute the spatial gradient for the dissipation measurement, a particular numerical stencil must be used. For example, Mi and Nathan (2003) used central differencing, and Barlow and Karpetis (2002) tested pixel binning and curve fitting techniques which are equivalent to a spatial domain averaging filter. Two schemes are commonly used to calculate the gradient: first order forward or backward differences and central differences as shown in Table 3.1 (Oppenheim et al. 1999). They are essentially digital filters in nature. In Table 3.1 $\delta[n]$ is the delta function, f_s is the sampling frequency, $H_g(e^{j\omega})$ is the Discrete Time Fourier Transform (DTFT) of the impulse response function $h_g[n]$, $\left|H_g(e^{j\omega})\right|$ is the magnitude of the $H_g(e^{j\omega})$, and ω is the angular frequency [rad/s]. The gradient *g(x)* is determined from:

$$\begin{aligned} g &= h_g * s = h_g * (h_p * i) = h_g * [h_p * (LSF * o + n)] \\ &= h_g * h_p * LSF * o + h_g * h_p * n. \end{aligned} \tag{3.10}$$

The gradient filter $h_g(x)$ is a high-pass filter for forward/backward differencing and a band-pass filter for the central difference scheme respectively.

The post-processing filter, $h_p(x)$, is generally a linear low-pass filter, e.g. Gaussian filter. However, it can also be a non-linear filter, e.g. a median filter, an image-processing morphological filter, or a non-isotropic filter. This model can not be applied to non-linear filters, but a numerical simulation can be used following the same procedure. Due to optical blurring, *LSF(x)* is a low-pass filter in most experiments.

Table 3.1 Comparison of differentiation stencils

Scheme	1st order backward difference	2nd order central difference
$g[n]$	$(s[n]-s[n-1])/\Delta t$	$(s[n+1]-s[n-1])/2\Delta t$
$h_g[n]$	$f_s\cdot(\delta[n]-\delta[n-1])$	$0.5\cdot f_s\cdot(\delta[n+1]-\delta[n-1])$
$H_g(e^{j\omega})$	$2f_s\cdot je^{-j\omega/2}\sin(\omega/2)$	$f_s\cdot j\sin(\omega)$
$\lvert H_g(e^{j\omega})\rvert$	$2f_s\cdot\lvert\sin(\omega/2)\rvert$	$f_s\cdot\lvert\sin(\omega)\rvert$
Filter type:	High-Pass filter	Band-Pass filter
Figure:	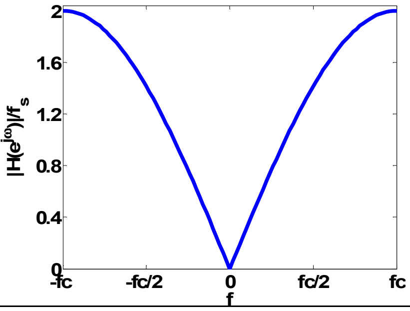	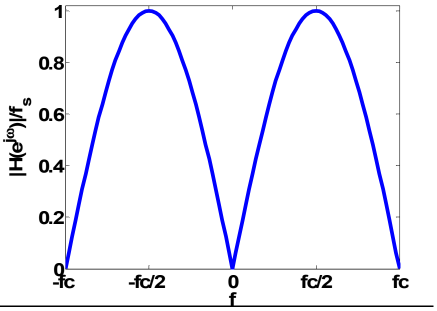

Figure 3.7 shows an example of the one-side forward differencing and central differencing effects when calculating the power spectral density (PSD) of the temperature gradient. The calculation of the PSD will be discussed in a later section. The experimental data is from temperature measurements in a turbulent

non-premixed jet flame at $Re_d = 15{,}200$ and $x/d = 80$ (detail discussion of experimental data will be presented in Chapter 4). The sampling frequency is 10 kHz and the effective cut-off frequency is 5 kHz. The black curve is the theoretical gradient spectra computed from the data, i.e., in isotropic turbulence the dissipation is expected to scale as $f^2 PSD_T(f)$. Note that the f^2 scaling greatly amplifies the noise at high frequencies. It can be seen clearly that at the high frequency end, the central-difference stencil attenuates the signal because it acts as a band-pass filter, whereas the one-sided difference, which acts as a high-pass filter, amplifies the noise.

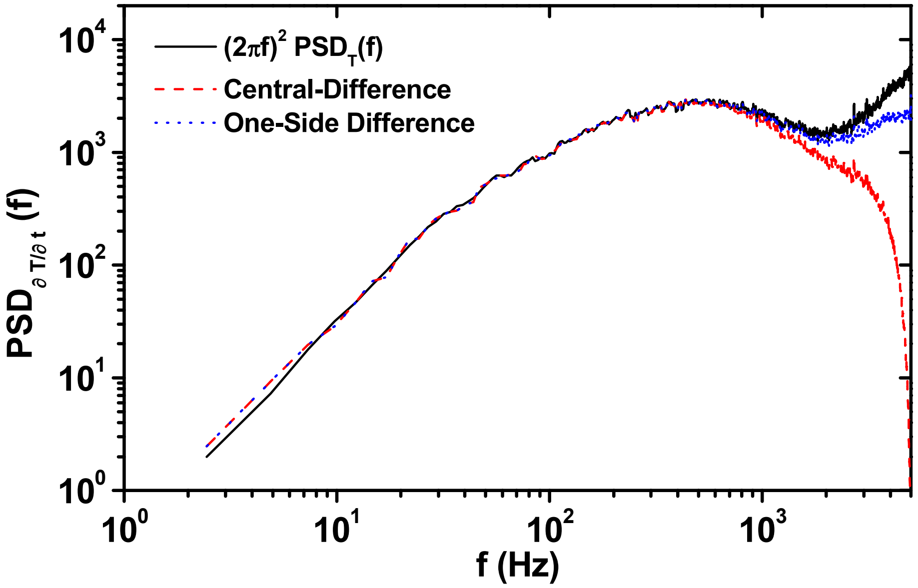

Figure 3.7 Effect of gradient stencil on the computation of the temperature gradient *PSD*. $PSD_T(f)$ and $PSD_{\partial T/\partial t}(f)$ are the *PSD*s of the temperature and temperature gradient respectively. The black curve was computed without differentiation of the data, whereas the red and blue curves were differenced. Data were acquired in a turbulent nonpremixed jet flame, Re_d=15,200, x/d=80.

It should be noted that the objective is to measure the thermal dissipation, which is most significant at the high frequency end of the spectrum. The example above shows that the stencil has a significant effect on this calculation. This has significant implications when comparing experimental data from different sources or obtained using different experimental techniques.

Without the post-processing filter $h_p(x)$, the noise will be amplified by the gradient calculation filter $h_g(x)$ since the gradient is calculated as:

$$g = h_g * LSF * o + h_g * n\,, \tag{3.11}$$

where $h_g(x)$ is a high-pass or band-pass filter. As discussed earlier, *LSF* is low-pass in nature and h_g could be band-bass or high-pass. Therefore, the filter applied to *o(x)*, i.e., $h_g * LSF$, will be a band-pass filter or all-stop filter. The worst case is clearly when the combined filter is an all-stop one which essentially means that useful information in the spectra will be filtered out and only noise will be remained in the calculated gradient and dissipation.

3.3 APPARENT DISSIPATION (NOISE-BIAS)

Here we present an analysis of the noise effect in the scalar dissipation measurement, which is similar to the work of Mi and Antonia (1994b). The assumptions made in the derivations are carefully considered and their validity is also discussed. In contrast to Mi and Antonia (1994b), the errors due to noise will be cast in term of the SNR. The derivation is for temperature measurements although it can be readily extended to other scalars.

The instantaneous measured temperature can be decomposed as follows

$$T_m(x,t) = \overline{T}_m(x,t) + T'_m(x,t)\,, \tag{3.12}$$

where $\overline{T}_m$ and T'_m are the measured mean and fluctuating temperatures, respectively. The standard deviation of the measured temperature T_m is σ_m. The instantaneous measured temperature can also be represented by the instantaneous true temperature *T(x,t)* and noise *n(x,t)* as

$$T_m(x,t) = T(x,t) + n(x,t)\,. \tag{3.13}$$

The instantaneous true temperature is

$$T(x,t) = \overline{T}(x,t) + T'(x,t)\,, \tag{3.14}$$

where $\overline{T}$ and T' are the mean and fluctuation of the true temperature respectively. The standard deviation of the true temperature T is σ_T. The noise *n(x,t)* has zero mean and standard deviation of σ_n. From these definitions, it can be shown that

$$T_m(x,t) = \overline{T}(x,t) + T'(x,t) + n(x,t)\,, \tag{3.15}$$

$$T'_m(x,t) = T'(x,t) + n(x,t)\,. \tag{3.16}$$

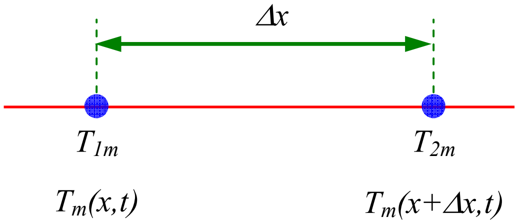

Figure 3.8 Illustration of the differentiation stencil

To simplify the derivations, the following substitutions were used as shown in Fig. 3.8:

$$T_{1m} = T_m(x,t)\,, \tag{3.17}$$

$$T_{2m} = T_m(x+\Delta x,t)\,. \tag{3.18}$$

In the following derivation it was further assumed that adjacent sampling points are so closely spaced that they have the same local mean values, i.e. $\overline{T_{1m}} = \overline{T_{2m}}$, i.e., the probes measure a relatively large *instantaneous* temperature difference, but a small difference in the *mean* temperature. Additionally, it is assumed that noise is independent of the fluctuating temperature, i.e. $\overline{T_i' \cdot n_j} = 0$ where $i = 1, 2$ and $j = 1, 2$. Using these assumptions, one obtains:

$$(\partial T/\partial x)_m = \left(T_{2m}' - T_{1m}'\right)/\Delta x \,, \tag{3.19}$$

$$(\partial T/\partial x)_m^2 = \left[\left(T_2' - T_1'\right) + \left(n_2 - n_1\right)\right]/\Delta x^2 \tag{3.20}$$

$$\overline{(\partial T/\partial x)_m^2} = \frac{1}{\Delta x^2}\left[\underbrace{\overline{\left(T_2' - T'\right)^2}}_{I} + \underbrace{2\overline{\left(T_2' - T_1'\right)\left(n_2 - n_1\right)}}_{II} + \underbrace{\overline{\left(n_2 - n_1\right)^2}}_{III}\right], \tag{3.21}$$

$$\text{Term I:} \quad \overline{\left(T_2' - T_1'\right)^2}\Big/\Delta x^2 = \overline{(\partial T/\partial x)^2} \,, \tag{3.22}$$

$$\text{Term II:} \quad \overline{\left(T_2' - T_1'\right)\left(n_2 - n_1\right)}\Big/\Delta x^2 = 0 \,, \tag{3.23}$$

$$\text{Term III:} \quad \overline{\left(n_2 - n_1\right)^2}\Big/\Delta x^2 \,. \tag{3.24}$$

It can be seen that Term I is the true or noise-free finite-difference approximation to the squared gradient, Term II represents all the cross-correlations between noise and signal and Term III is the apparent squared gradient or noise-bias. If all the cross correlation terms are neglected (Eqn. 3.23), the measured squared gradient square is:

$$\overline{(\partial T/\partial x)_m^2} = \overline{(\partial T/\partial x)^2} + \overline{\left(n_2 - n_1\right)^2}\Big/\Delta x^2 \,. \tag{3.25}$$

The absolute and relative errors are given by:

$$\text{Absolute:} \quad \varepsilon_a = \overline{(\partial T/\partial x)_m^2} - \overline{(\partial T/\partial x)^2} = \overline{\left(n_2 - n_1\right)^2}\Big/\Delta x^2 \,, \tag{3.26}$$

$$\text{Relative:} \quad \varepsilon_r = \varepsilon_a \Big/ \overline{(\partial T/\partial x)^2} = \overline{\left(n_2 - n_1\right)^2}\Big/\overline{\left(T_2 - T_1\right)^2} \,. \tag{3.27}$$

Defining the instantaneous temperature difference as $\Delta T = T_2 - T_1 = T_2' - T_1'$, these errors can be written as:

$$\varepsilon_a = \overline{(n_2 - n_1)^2} \big/ \Delta x^2 \tag{3.28}$$

$$\varepsilon_r = \overline{(n_2 - n_1)^2} \big/ \overline{\Delta T^2} \tag{3.29}$$

3.3.1 Case 1

If the noise signals in the adjacent two points are uncorrelated, i.e. $\overline{n_i \cdot n_j} = 0$ for $i \neq j$, the above errors will be:

$$\varepsilon_a = \left(\overline{n_2^2} + \overline{n_1^2}\right) \big/ \Delta x^2 , \tag{3.30}$$

$$\varepsilon_r = \left(\overline{n_2^2} + \overline{n_1^2}\right) \big/ \overline{\Delta T^2} . \tag{3.31}$$

If the standard deviation of the noise is defined as $\overline{n^2} = \sigma_n^2$, the absolute error is given by:

$$\varepsilon_a = \left(\sigma_{n_1}^2 + \sigma_{n_2}^2\right) \big/ \Delta x^2 \tag{3.32}$$

Defining the SNR as

$$SNR_i = \overline{T_i} \big/ \sigma_{ni} , \tag{3.33}$$

the absolute error is

$$\varepsilon_a = \frac{1}{\Delta x^2}\left[\left(\frac{\overline{T_1}}{SNR_1}\right)^2 + \left(\frac{\overline{T_2}}{SNR_2}\right)^2\right]. \tag{3.34}$$

Since the mean gradient is small we can let $\overline{T_1} \approx \overline{T_2} = \overline{T}$, in which case these errors will be:

$$\varepsilon_a = \left(\frac{\overline{T}}{\Delta x}\right)^2 \left[\frac{1}{SNR_1^2} + \frac{1}{SNR_2^2}\right], \tag{3.35}$$

$$\varepsilon_r = \frac{\overline{T}^2}{\overline{\Delta T^2}} \left[\frac{1}{SNR_1^2} + \frac{1}{SNR_2^2}\right]. \tag{3.36}$$

For experiments dominated by detector noise, the noise can be modeled as Gaussian and this assumption will apply.

3.3.2 Case 2

If the fluctuation of the two channels are independent, i.e. $\overline{T_1' T_2'} = 0$, the errors are given by:

$$\varepsilon_a = \left(\frac{\overline{T}}{\Delta x}\right)^2 \left[\frac{1}{SNR_1^2} + \frac{1}{SNR_2^2}\right], \tag{3.37}$$

$$\varepsilon_r = \frac{\overline{T}^2}{(\overline{T_1'^2} + \overline{T_2'^2})} \left[\frac{1}{SNR_1^2} + \frac{1}{SNR_2^2}\right]. \tag{3.38}$$

For the current two-point technique, the two point spacing is approximately equal to the Batchelor scale (discussed in Chapter 4). In this case the temperature fluctuations on each channel are correlated and so this case is not applicable here.

3.3.3 Case 3

If further assumed that the two detection channels have the same noise characteristics (i.e. $\sigma_{n_1} = \sigma_{n_2}$), and the two channels have the same fluctuation temperature (i.e., $T_{1,rms} = T_{2,rms}$), the absolute and relative errors are:

$$\varepsilon_a = \left(\frac{\sqrt{2}\overline{T}}{\Delta x \cdot SNR}\right)^2 = \left(\frac{\sqrt{2}\sigma_n}{\Delta x}\right)^2, \tag{3.39}$$

$$\varepsilon_r = \left(\frac{\overline{T}}{T_{rms} SNR}\right)^2 = \left(\frac{1}{T_{TI} \cdot SNR}\right)^2 = \left(\frac{\sigma_n}{T_{rms}}\right)^2. \tag{3.40}$$

where $T_{TI} = T_{rms} / \overline{T}$ is the turbulence intensity of the temperature fluctuations.

Equation 3.40 shows that the effect of noise is only important when the variance of the noise is large compared to the variance of the temperature. Interestingly, the SNR is not the key factor in the scalar dissipation measurement, but rather the *Turbulence-to-Noise Ratio* (*TNR*) defined by

$$TNR = T_{rms} / \sigma_n . \tag{3.41}$$

The higher the TNR, the lower is the relative error due to noise. This implies that the relative experimental error due to noise in scalar dissipation measurements depends on the specific flow conditions. Even for the same noise level, the relative error is different for different measurement locations, e.g., along the centerline versus the edge of the jet flame. This makes the quantification of the noise error in scalar dissipation measurements even harder.

The above relations also show that the effect of noise is to make the measured scalar dissipation higher than the true scalar dissipation, i.e., $\overline{(\partial T/\partial x)_m^2} \geq \overline{(\partial T/\partial x)^2}$. Especially when $\Delta x \to 0$, $\overline{(\partial T/\partial x)_m^2} \to \infty$. Therefore, for very small values of Δx (high spatial resolution), $\overline{(\partial T/\partial x)_m^2}$ can be much greater than $\overline{(\partial T/\partial x)^2}$. This emphasizes the need for noise correction if accurate quantitative measurements are needed.

The effect of noise is opposite to that of finite spatial resolution because the effect of blurring always reduces the measured dissipation relative to the true value. Noise error will dominate the dissipation measurement error at fine resolution, whereas errors associated with finite resolution will dominate at coarse resolution. This illustrates the difficulty in quantitative dissipation measurements. The measurements must resolve the Batchelor scale to be fully spatially resolved, which means that a very small Δx is needed, but the dissipation measurement error goes up as Δx^{-2}.

3.3.4 Error relations for current study

The following assumptions/facts were used in the current two-point time series measurements. The two channels were adjusted so that the noise characteristics were nearly the same in each channel, i.e. $\overline{n_2^2} = \overline{n_1^2} = \sigma_n^2$. And the cross correlation between noise and temperature fluctuation were neglected; therefore, the following relations apply:

$$\overline{(\partial T/\partial x)_m^2} = \overline{(\partial T/\partial x)^2} + 2\sigma_n^2 / \Delta x^2 \tag{3.42}$$

Absolute error: $\varepsilon_a = 2\sigma_n^2 / \Delta x^2$ (3.43)

Relative error: $\varepsilon_r = \varepsilon_a / \overline{(\partial T/\partial x)^2} = 2\sigma_n^2 / \overline{(T_2 - T_1)^2}$ (3.44)

For the current study, the *Difference Signal-to-Noise Ratio* (*DSNR)*

$$DSNR = \sqrt{\overline{\Delta T^2}} / \sigma_n\ . \tag{3.45}$$

will be more proper since the two channels are not independent. Accurate dissipation measurements require that the probes be so closely spaced that the temperature difference is small, obtaining sufficiently high *DSNR* is challenging in most experiments.

3.4 APPARENT DISSIPATION CORRECTION TECHNIQUES

In the above sections, the importance of the noise effects was clearly shown in the measurement model. The question that arises naturally from this analysis is: How should one correct for the noise bias? In this section, several techniques are presented and discussed to correct for the apparent dissipation, or noise bias, in the measured scalar dissipation.

3.4.1 Redundant measurement

If the two sampling points are overlapped, then the mean and fluctuations of the two points will be equal, i.e. $\overline{T_1} = \overline{T_2}$ and $T_1' = T_2'$. The measured mean squared gradient becomes:

$$\overline{(\partial T/\partial x)_m^2} = \overline{(n_2 - n_1)^2 / \Delta x^2} \tag{3.46}$$

This is essentially the absolute error of the mean gradient squared given by Eqn. (3.28). When the two sampling points are separated, the measured mean squared gradient will be the same as Eqn. (3.25). Subtracting Eqn. (3.46) from Eqn. (3.25) will give the true mean squared difference as in Eqn. (3.22).

Notice that this correction can only be applied to mean quantities, e.g., scalar dissipation, fluctuation temperature, skewness, etc. In practice, this technique can be implemented by performing two separate measurements with the two-point technique. The first run with the two points separated by a specific distance gives the measured scalar dissipation. The second run with overlapped points gives the corresponding noise statistics. Subtraction of the second run from the first run yields the true mean scalar dissipation rate to within the precision permitted by the spatial resolution.

3.4.2 Pixel-Binning

Noise correction in 1-D line-imaging experiments can be made in the same manner as for the two-point technique.

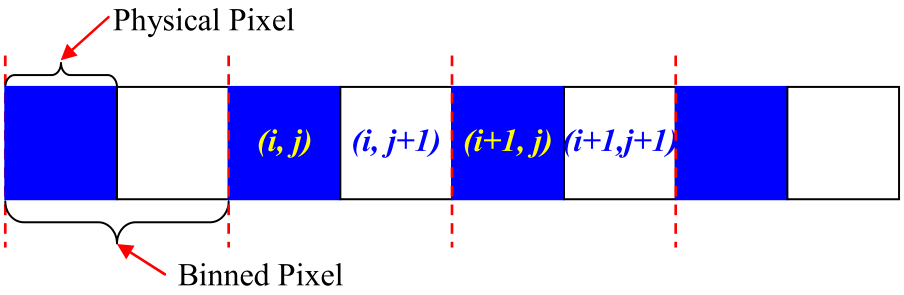

Figure 3.9 Illustration of the pixel-binning in 1-D imaging experiments. (*i, j*) is the pixel index, *i* is the binned or super pixel index and *j* is the index of the physical pixel within the super-pixel *i*

Assuming that the true resolution is limited by the binned pixel size, e.g., twice the physical pixel size in Fig. 3.9, the instantaneous measured temperature is:

$$T_{m,ij} = \overline{T}_i + T_i' + n_{ij}\,, \tag{3.47}$$

where i is the binned- or super- pixel index and j is the physical index within the binned pixel which is 1 and 2 in this case. Assuming that these two physical pixels within the binned pixel have similar characteristics, i.e., $\overline{T_{i1}} = \overline{T_{i2}} = \overline{T_i}$, $T_{i1}' = T_{i2}' = T_i'$. The instantaneous measured temperature for the binned pixel is then

$$T_{m,i} = \left(T_{m,i1} + T_{m,i2}\right)/2 = \overline{T}_i + T_i' + \left(n_{i1} + n_{i2}\right)/2 = \overline{T}_i + T_i' + n_i\,, \tag{3.48}$$

where n_i is the noise of the super-pixel i, $n_i = \left(n_{i1} + n_{i2}\right)/2$. The measured mean scalar dissipation is

$$\overline{(\partial T/\partial x)_m^2} = \frac{1}{\Delta x^2}\left[\overline{\left(T_2' - T_1'\right)^2} + \overline{\left(n_2 - n_1\right)^2}\right], \tag{3.49}$$

where the noise correlation term can be expressed as:

$$\overline{\left(n_2 - n_1\right)^2} = \overline{[(n_{21} + n_{22}) - (n_{11} + n_{12})]^2}/4\,. \tag{3.50}$$

From the instantaneous measurements, one obtains

$$\overline{[(T_{m,12} - T_{m,11}) + (T_{m,22} - T_{m,21})]^2} = \overline{[(n_{12} - n_{11}) + (n_{22} - n_{21})]^2}\,. \tag{3.51}$$

If we assume that

$$\overline{\left(n_{11}n_{12} + n_{21}n_{22} - n_{12}n_{22} - n_{11}n_{21}\right)} \approx 0\,, \tag{3.52}$$

then the error can be determined from

$$\overline{\left(n_2 - n_1\right)^2}/\Delta x^2 = \overline{[(T_{m,12} - T_{m,11}) + (T_{m,22} - T_{m,21})]^2}/4\Delta x^2\,. \tag{3.53}$$

If all noise terms are uncorrelated, then this assumption is not necessary and the relation is exact. If the noise terms are correlated, then the error arising from the assumption will be smaller to the extent that the positive and negative terms cancel each other. The assumption can be checked by verifying that the following relation is satisfied:

$$\overline{[(T_{m,12}-T_{m,11})+(T_{m,22}-T_{m,21})]^2} \approx \overline{[(T_{m,12}-T_{m,11})-(T_{m,22}-T_{m,21})]^2} \quad (3.54)$$

This technique is essentially another redundant technique since the information from the two binned pixels is used to infer the noise statistics. It can also be extended to 2-D imaging when pixel-binning is used.

3.4.3 Power Spectra Density (PSD) correction technique

For time-series measurements, the noise in the measured signal will affect the measured power spectra (especially in the high frequency region), the autocorrelation function and dissipation rate. A correction for noise effects is therefore necessary.

The derivation will follow the procedure of Gaskey et al. (1990), Miller and Dimotakis (1996), Renfro et al. (1999, 2000). Renfro et al. (1999) used it to correct the power spectral density (PSD) and auto-correlation functions of OH time-series data and found that for the jet exit Reynolds number greater than a threshold value (i.e., 2800), the normalized auto-correlation functions will overlap independent of Reynolds number. Here, a more detailed derivation is provided and a calculation procedure is summarized at the end of the section.

In Renfro’s work (1999, 2000), the PSD correction technique was used only for the PSD and auto-correlation function correction. Here, this technique is further extended to the correction of the mean scalar dissipation. All derivations are shown in detail starting from the PSD correction technique.

The standard-deviations of the measured temperature $T_m(t)$ and true temperature $T(t)$ are σ_m and σ_T, respectively. The noise $n(t)$ has zero mean and standard deviation of σ_n. From these definitions and the assumption that *noise and measured temperature are independent*, it can be shown that

$$\sigma_m^2 = \sigma_T^2 + \sigma_n^2 , \tag{3.55}$$

$$(\sigma_T / \sigma_m)^2 = 1 - C^2 , \tag{3.56}$$

where $C = \sigma_n / \sigma_m$ is the noise fluctuation intensity normalized by the total fluctuation intensity (*rms*), and $C \leq 1$. If the signal is normalized by its own standard deviation, e.g., $T_m'^*(t) = T_m'(t)/\sigma_m$ where "*" denotes the normalized signal, the relation between the normalized signals will be

$$\sigma_m T_m'^*(t) = \sigma_T T'^*(t) + \sigma_n n^*(t) . \tag{3.57}$$

The normalized fluctuation signals will have zero mean and unity standard deviation by definition. The corresponding autocorrelation functions are

$$R_{T_m'^*}(\tau) = \frac{\overline{T_m'(t) T_m'(t-\tau)}}{\sigma_m^2} = \int_0^\infty PSD_{T_m'^*}(f) e^{j2\pi f\tau} df , \tag{3.58}$$

$$R_{T'^*}(\tau) = \frac{\overline{T'(t) T'(t-\tau)}}{\sigma_T^2} = \int_0^\infty PSD_{T'^*}(f) e^{j2\pi f\tau} df , \tag{3.59}$$

$$R_{n^*}(\tau) = \frac{\overline{SN(t) SN(t-\tau)}}{\sigma_n^2} = \int_0^\infty PSD_{n^*}(f) e^{j2\pi f\tau} df . \tag{3.60}$$

At $\tau = 0$, the autocorrelation functions are

$$R_{T_m'^*}(0) = \int_0^\infty PSD_{T_m'^*}(f) df = 1 , \tag{3.61}$$

$$R_{T'^*}(0) = \int_0^\infty PSD_{T'^*}(f) df = 1 , \tag{3.62}$$

$$R_{n^*}(0) = \int_0^\infty PSD_{n^*}(f) df = 1 . \tag{3.63}$$

The relations between power spectral density functions are

$$PSD_{T_m'}(f) = PSD_{T'}(f) + PSD_n(f) , \tag{3.64}$$

$$PSD_{T'_m}(f) = \sigma_m^2 PSD_{T'^*_m}(f) = \sigma_T^2 PSD_{T'^*}(f) + \sigma_n^2 PSD_{n^*}(f)\,, \qquad (3.65)$$

$$PSD_{T'_m}(f) \big/ \sigma_m^2 = (1 - C^2) PSD_{T'^*}(f) + C^2 PSD_{n^*}(f)\,. \qquad (3.66)$$

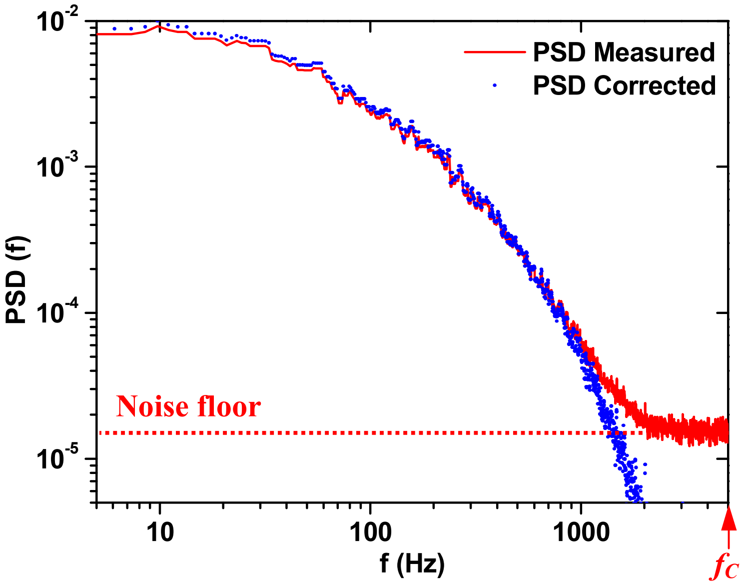

Figure 3.10 Comparing measured and corrected PSDs

For turbulent flow, the PSD at high frequency is usually dominated by the noise (noise floor $PSD_{NF}(f)$) which suggests that

$$PSD_{NF}(f) = C^2 PSD_{n^*}(f), \quad when\ f \to f_C\,. \qquad (3.67)$$

Here f_C is the cutoff frequency in the PSD and is equal to half the sampling rate f_s. The noise PSD is generally assumed flat, which means it is evenly distributed over all frequencies as shown in Fig. 3.10. With the assumption that $PSD_{n^*}(f) = const$, it can be shown that,

$$PSD_{n^*}(f) = 1/f_C\,, \quad for\ f \le f_C\,. \qquad (3.68)$$

Note that this is for the normalized noise signal $n^*(t)$ only

$$PSD_{NF}(f) = C^2 / f_C \,. \tag{3.69}$$

Thus by averaging the $PSD_{T_m'^*}$ at high frequencies where noise dominates, C can be determined from

$$C = \sqrt{f_C \cdot PSD_{NF}(f)} \,. \tag{3.70}$$

The true fluctuating $PSD_{\underline{T'}}(f)$ can then be corrected to remove noise effects by:

$$PSD_{T'^*}(f) = \frac{PSD_{T_m'^*}(f) - PSD_{NF}(f)}{1 - C^2} = \frac{PSD_{T_m'^*}(f) - C^2 / f_C}{1 - C^2} \tag{3.71}$$

Accordingly the corrected autocorrelation function can be calculated as:

$$\begin{aligned} R_{\underline{T'}}(\tau) &= \Im^{-1}\left(\frac{PSD_{T_m'^*}(f) - C^2 / f_C}{1 - C^2} \right) \\ &= \frac{\Im^{-1}\left\{ PSD_{T_m'^*}(f) \right\}}{1 - C^2} - \Im^{-1}\left(\frac{C^2 / f_C}{1 - C^2} \right) = \frac{R_{T_m'^*}(\tau)}{1 - C^2} - \left(\frac{C^2}{1 - C^2} \right) \delta(\tau) \end{aligned} \tag{3.72}$$

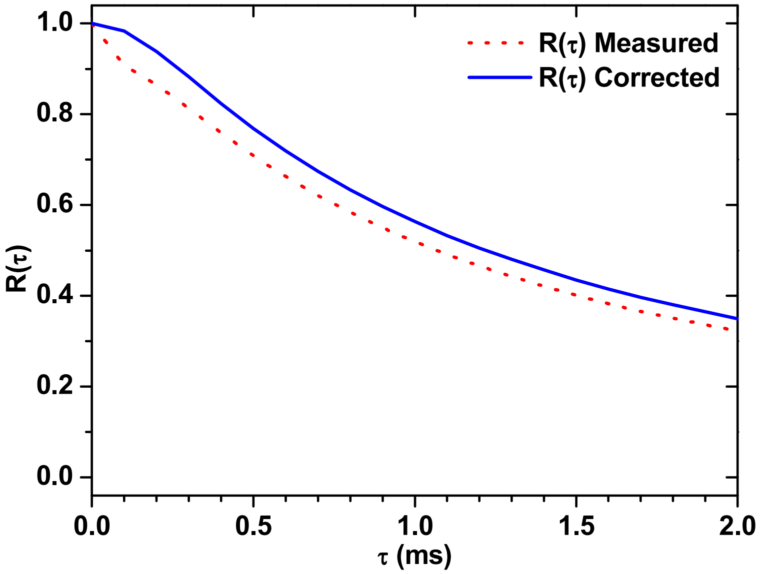

Figure 3.11 Comparing measured and corrected autocorrelation functions

The corrected integral time scale is then

$$\tau_I = \int_0^\infty R_{T'^*}(\tau)d\tau = PSD_{T'^*}(0) \tag{3.73}$$

An example comparing the original and corrected auto-correlation function is illustrated in Fig. 3.11. The most significant correction effect is near the origin which essentially changes the curvature of the profile. This will significantly affect the measured Taylor micro-scale since it is calculated by the fitting of a parabola near the origin.

The whole calculation procedure is summarized as follows:

1. Calculate mean temperature $\overline{T}_m$ and fluctuating temperature $T'_m(t) = T_m(t) - \overline{T}_m$ from the measured temperature T_m;
2. Normalize the fluctuating temperature $T'_m(t)$ to get $T'^*_m(t) = T'_m(t)/\sigma_m$;
3. Calculate the PSD for the normalized fluctuating temperature $T'^*_m(t)$, $PSD_{T'^*_m}(f) = (1-C^2)PSD_{T^*}(f) + C^2 PSD_{n^*}(f)$;
4. Average the measured PSD in the high frequency region (noise floor), where $PSD_{T'^*_m}(f) = C^2/f_C$
5. Calculate $C = \sqrt{f_C \cdot PSD_{T'^*_m}(f)}$;
6. Apply the correction to calculate the PSD for the true fluctuating temperature $T'(t)$ from: $PSD_{T'^*}(f) = \dfrac{PSD_{T'^*_m}(f) - C^2/f_C}{1-C^2}$
7. Calculate the autocorrelation function for the true fluctuating temperature $T'(t)$ as: $R_{T'^*}(\tau) = \dfrac{R_{T'^*_m}(\tau)}{1-C^2} - \left(\dfrac{C^2}{1-C^2}\right)\delta(\tau)$
8. Calculate the integral time scale τ_I for the true fluctuating temperature $T'(t)$ from: $\tau_I = \int_0^\infty R_{T'^*}(\tau)d\tau = PSD_{T'^*}(0)$
9. Calculate Signal-to-Noise Ratio (SNR) of the true temperature from:

$$SNR = \frac{\overline{T}}{\sigma_n} = \frac{\overline{T_m}}{C\sigma_m}$$

10. Correct the measured scalar dissipation via:

$$\overline{(\partial T/\partial x)^2} = \overline{(\partial T/\partial x)_m^2} - 2C^2\sigma_m^2/\Delta x^2 \ .$$

In this procedure, steps from 1 to 8 were used by Gaskey et al. (1990) in correction of LIF signals obtained in a non-reacting jet. Renfro et al. (1999, 2000) applied it in their OH LIF experiments. In the current study their procedure was extended by steps 9 and 10, using C and σ_m and the additional assumption that the noise signals in different channels are uncorrelated.

3.5 APPARENT DISSIPATION ESTIMATION TECHNIQUES

If the measurement is not temporally resolved due to a high Batchelor frequency, or the measurement itself is only statistical in nature (e.g., as with most Raman, LIF and 2-D imaging techniques using pulsed lasers with low repetition rates), the correction method based on the PSD analysis can not be used. When designing experiments with the objective of measuring scalar dissipation (i.e., choosing the experimental technique, flow conditions, fuel combinations, etc.), one also needs to estimate how the apparent dissipation will affect the measurement accuracy. Here, a procedure is developed to estimate the best possible measurement, i.e. the one with the smallest apparent dissipation in the real experiments. The effect of the data-reduction sub-model will also be discussed here.

3.5.1 Apparent noise estimation for mixture fraction measurement by Rayleigh scattering in non-reacting flows

For a binary gas mixture of fuel and air, the Rayleigh scattering signal is

$$I_R = C_{R1} n \left(x_f \sigma_f + x_{air} \sigma_{air} \right) = C_{R2} [A x_f + 1] \tag{3.74}$$

where x_f and x_{air} are the mole fractions of fuel and air respectively, C_{R1} and C_{R2} are constants that depend on the collection optics, detector quantum efficiency, etc., and $A = \sigma_f / \sigma_{air} - 1$. Once the calibration intensities are available, the concentration of an arbitrary mixture of the two species can be calculated from

$$x_f(t) = \frac{I_R(t) - I_{R,air}}{I_{R,f} - I_{R,air}} = \frac{I_R / I_{R,air} - 1}{A}, \tag{3.75}$$

where $I_R(t)$, $I_{R,f}$ and $I_{R,air}$ are the Rayleigh scattering intensities from the mixture, pure fuel and pure air, respectively. For the non-reacting case, the mixture fraction ξ is identical to the fuel mass fraction and is related to x_f by the following equation, which accounts for the molecular weight of air and fuel:

$$\xi(t) = \frac{x_f(t) MW_f}{x_f(t)(MW_f - MW_{air}) + MW_{air}}. \tag{3.76}$$

where MW_f and MW_{air} are the molecular weight of fuel and air respectively. If the fuel has nearly the same molecular weight as that of the air (e.g., for ethylene C_2H_4, $MW_f \approx MW_{air}$), this equation simplifies to

$$\xi(t) \approx x_f(t), \tag{3.77}$$

which means that the mixture fraction is equal to the mole fraction.

$$\xi(t) \approx x_f(t) = \frac{I_R / I_{R,air} - 1}{A} \tag{3.78}$$

Differentiating the above equation, it can be shown that the noise standard deviation in the measured mixture fraction is

$$\sigma_{n,\xi} = \frac{1}{A\, I_{R,air}} \sigma_{n,I_R}, \tag{3.79}$$

where σ_{n,I_R} is the corresponding noise standard deviation of the Rayleigh scattering signal. The absolute error for the dissipation derived from the two-point technique is

$$\varepsilon_{a,\xi} = \overline{(n_2 - n_1)^2} \big/ \Delta r^2 = 2\sigma_{n,\xi}^2 \big/ \Delta r^2, \tag{3.80}$$

$$\varepsilon_{a,\xi} = \frac{2\sigma_{n,I_R}^2}{\left(A\, I_{R,air}\right)^2} \frac{1}{\Delta r^2} = 2\frac{1}{A^2 \Delta r^2} \frac{1}{SNR_{air}^2} \frac{\sigma_{n,I_R}^2}{\sigma_{n,I_{R,air}}^2}, \tag{3.81}$$

where $SNR_{air} = I_{R,air} \big/ \sigma_{n,I_{R,air}}$. In pure air, the apparent dissipation due to noise is

$$\varepsilon_{a,\xi_{air}} = \frac{2\sigma_{n,I_{R,air}}^2}{\left(A\, I_{R,air}\right)^2} \frac{1}{\Delta r^2} = 2\frac{1}{A^2 \Delta r^2} \frac{1}{SNR_{air}^2}. \tag{3.82}$$

The ratio of any measured absolute error to that of the air is

$$\frac{\varepsilon_{a,\xi}}{\varepsilon_{a,\xi_{air}}} = \left(\frac{\sigma_{n,I_R}}{\sigma_{n,I_{R,air}}} \right)^2. \tag{3.83}$$

If the measurement is shot-noise limited, the ratio of the standard deviation of the noise is

$$\frac{\sigma_{n,I_R}}{\sigma_{n,I_{R,air}}} = \sqrt{\frac{I_R}{I_{R,air}}}. \tag{3.84}$$

Therefore, the corresponding absolute error ratio is

$$\frac{\varepsilon_{a,\xi}}{\varepsilon_{a,\xi_{air}}} = \frac{I_R}{I_{R,air}} = A\xi + 1. \tag{3.85}$$

This implies that the apparent noise is proportional to the signal intensity, the higher the signal the higher the apparent noise.

The centerline mixture fraction decay for non-reacting jets can be correlated with distance from the virtual origin x_0. This correlation can be expressed as

$$\overline{\xi_C} = \frac{C_1}{(x-x_0)/d^*}, \tag{3.86}$$

where C_1 is a constant, and d^* is the effective diameter $d^* = d(\rho_j/\rho_\infty)^{1/2}$. Experimental results (Schefer and Dibble, 2000) showed that C_1 is independent of the density ratio in non-reacting jets and $C_1 \approx 5$. If the virtual origin is small and can be neglected, and $d^* \approx d$ for $MW_f \approx MW_{air}$, then

$$\frac{\varepsilon_{a,\xi_C}}{\varepsilon_{a,\xi_{air}}} = \frac{I_{R_C}}{I_{R,air}} = A\overline{\xi_C} + 1 = \frac{5A}{x/d} + 1. \tag{3.87}$$

If the fuel is ethylene, $A = \sigma_f/\sigma_{air} - 1 = 5.02$, so

$$\frac{\varepsilon_{a,\xi_C}}{\varepsilon_{a,\xi_{air}}} = \frac{25.1}{x/d} + 1. \tag{3.88}$$

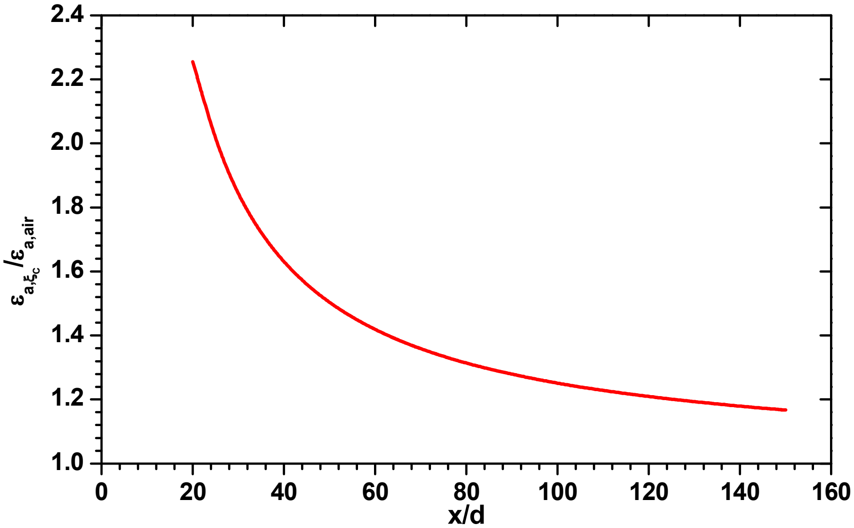

Figure 3.12 Centerline absolute error ratio $\varepsilon_{a,\xi_C}/\varepsilon_{a,\xi_{air}}$ in non-reacting ethylene jet.

Figure 3.12 shows the centerline absolute error ratio as a function of the normalized downstream distance *x/d*. It can be seen that the absolute error at *x/d* = 20 is about twice that at *x/d* = 150. This could be a significant problem if the ratio of the true scalar dissipation to the apparent dissipation in air is small.

From this analysis we see that non-reacting scalar dissipation measurements can be corrected exactly if the signal is shot-noise limited, or approximately if the SNR is very high.

3.5.2 Thermal dissipation measurement by shot-noise limited Rayleigh scattering in reacting flows

For constant Rayleigh cross section, the temperature can be derived simply from (discussed in Chapter 2):

$$T = I_{ref} T_{ref} \big/ I_R \, , \tag{3.89}$$

where I_{ref} is the reference Rayleigh scattering signal from air at room temperature (T_{ref}). The temperature is calculated by

$$T = C_T \big/ I_R \, , \tag{3.90}$$

where $C_T = I_{ref} T_{ref}$ is a constant. The relative error in the temperature measurement is

$$\sigma_{n,T} \big/ T = \sigma_{n,I_R} \big/ I_R \, . \tag{3.91}$$

The relative error for the dissipation derived from the two-point technique is

$$\varepsilon_{a,T} = \overline{(n_2 - n_1)^2} \big/ \Delta r^2 = 2\sigma_{n,T}^2 \big/ \Delta r^2 \, . \tag{3.92}$$

Substituting for $\sigma_{n,T}$ into this equation gives

$$\varepsilon_{a,T} = 2T^2 \left(\frac{\sigma_{n,I_R}}{I_R} \right)^2 \frac{1}{\Delta r^2} = 2T^2 \frac{1}{SNR^2} \frac{1}{\Delta r^2} \, , \tag{3.93}$$

where $SNR = I_R \big/ \sigma_{n,I_R}$. For measurements in air at room temperature, this error is

$$\varepsilon_{a,T_{air}} = 2T_{air}^2 \left(\frac{\sigma_{n,I_{R,air}}}{I_{R,air}} \right)^2 \frac{1}{\Delta r^2} = 2T_{air}^2 \frac{1}{SNR_{air}^2} \frac{1}{\Delta r^2}, \tag{3.94}$$

where $SNR_{air} = I_{R,air} / \sigma_{n,I_{R,air}}$. Therefore, the corresponding absolute error ratio is:

$$\frac{\varepsilon_{a,T}}{\varepsilon_{a,T_{air}}} = \left(\frac{T}{T_{air}} \right)^2 \left(\frac{\sigma_{n,I_R}}{I_R} \frac{I_{R,air}}{\sigma_{n,I_{R,air}}} \right)^2 = \left(\frac{T}{T_{air}} \right)^2 \left(\frac{SNR_{air}}{SNR} \right)^2 \tag{3.95}$$

If the signal is shot-noise limited, the SNR scales as

$$SNR \propto \sqrt{I_R}, \tag{3.96}$$

and therefore

$$\frac{SNR_{air}}{SNR} = \sqrt{\frac{I_{R,air}}{I_R}} = \sqrt{\frac{T}{T_{air}}}, \tag{3.97}$$

$$\frac{\varepsilon_a}{\varepsilon_{a,air}} = \left(\frac{T}{T_{air}} \right)^2 \left(\frac{SNR_{air}}{SNR} \right)^2 = \left(\frac{T}{T_{air}} \right)^3. \tag{3.98}$$

Equation (3.98) is an important relation because it shows that the apparent dissipation scales as T^3, which represents very strong temperature dependence. This shows that the apparent dissipation will likely be very large in high temperature regions of the flame unless the SNR in cold air is very high.

In the above analysis, we assumed that the thermal diffusivity was unity to simplify the analysis. In the real thermal dissipation measurements, the effect of the thermal diffusivity must be considered as well. Here the absolute error is

$$\varepsilon_{a,T} = 2\,\overline{\alpha(T)}\,T^2 \left(\frac{\sigma_{n,I_R}}{I_R} \right)^2 \frac{1}{\Delta r^2} = 2\,\overline{\alpha(T)}\,T^2 \frac{1}{SNR^2} \frac{1}{\Delta r^2}, \tag{3.99}$$

$$\frac{\varepsilon_{a,T}}{\varepsilon_{a,T_{air}}} = \frac{\overline{\alpha(T)}}{\overline{\alpha(T_{air})}} \left(\frac{T}{T_{air}} \right)^3 \approx \frac{\alpha(T)}{\alpha(T_{air})} \left(\frac{T}{T_{air}} \right)^3. \tag{3.100}$$

The thermal diffusivity is a strong function of temperature

$$\alpha(T) = \alpha_{ref} \left(T / T_{ref} \right)^{\gamma}, \tag{3.101}$$

where γ is a constant close to 1.8 and depends on the particular fuel composition. Therefore the absolute error ratio is

$$\frac{\varepsilon_{a,T}}{\varepsilon_{a,T_{air}}} = \left(\frac{T}{T_{air}}\right)^{3+\gamma} \approx \left(\frac{T}{T_{air}}\right)^{5}. \tag{3.102}$$

This shows that including the effects of the temperature-dependent thermal diffusivity makes the absolute error ratio even worse.

3.6 SUMMARY

A system-level model has been developed that shows the effect of all relevant processes required to compute the thermal dissipation. These processes include those related to the measurement itself (resolution and noise) as well as the computational techniques (such as smoothing and gradient filters) that operate on the measured data. The model shows that if the noise offset in the measured scalar dissipation can be corrected, or the SNR is so high that noise is not important in the dissipation measurement, then noise-effects can be neglected and the error is due to resolution only. The resolution error is determined by the optical system blur (or measurement bandwidth for time-series) and probe spacing. In this case, the analysis by Mi and Nathan (2003) for the probe resolution and model for flow imaging experiments proposed by Wang and Clemens (2004) can be applied.

If the noise offset cannot be determined and corrected, the noise effect can be removed or reduced by the post-processing averaging and smoothing filters but at the expense of resolution. Here the noise issue is essentially transferred to the resolution issue. The TNR and DSNR are more important in dissipation oriented measurements rather than the traditional SNR. The relative importance of turbulent fluctuations compared to noise will determine the relative error of measured scalar dissipation. This further illustrates the difficulties in getting precise measurement of scalar dissipation.

Noise correction techniques for the mean dissipation, e.g. the two-point overlapping technique, binning-pixel in 1-D imaging, and PSD for time-series data, were discussed and detailed correction procedures presented. Their limitations, especially the assumptions regarding noise, were presented. These assumptions regarding noise characteristics must be considered when applying these techniques.

For the laser Rayleigh scattering technique, the apparent dissipation at any measurement location can be scaled to the value in air. Therefore, it can be used to estimate the apparent dissipation or the absolute dissipation error in the scalar dissipation measurement.

Chapter 4. Time-series temperature and thermal dissipation measurement in a non-premixed turbulent jet flame

4.1 INTRODUCTION

The objective of this study is to make high-quality, high-repetition rate (10 kHz), two-point laser Rayleigh temperature measurements in a weakly co-flowing turbulent nonpremixed jet flame with high SNR (~65 in room air) and where the finest scales of turbulence were spatially and temporally resolved.

The spatial resolution was carefully considered and the error estimation procedures developed in chapter 3 are implemented in this chapter. An outstanding issue in turbulent flame research is how does one estimate the Batchelor scale? The answer to this question is important because it determines the measurement resolution that must be obtained to make accurate measurements of dissipation in flames. The fluctuating temperature measurements will be used to address this issue.

The two-point temperature data are used to obtain temperature fluctuations, power spectra, gradients, thermal dissipation rate and detailed statistics of the nonpremixed turbulent jet flame. The objective is to use this information to reveal characteristics of the underlying turbulence of this nonpremixed turbulent jet flame that were previously not available. The flame studied here was similar to the TNF simple jet flame DLR_A which was used as a benchmark flame for the TNF Workshop. The current two-point time-series measurements provide some additional insights into the structure of this benchmark flame.

To review the conditions studied, the fuel composition used was 22.1% CH_4, 33.2% H_2, 44.7% N_2 (by volume), which gives a stoichiometric mixture fraction of 0.167. The source Reynolds number was $Re_d = U_0 d/\nu_0$ = 15,200 (where ν_0 is the kinematic viscosity of the fuel and U_0 is the bulk jet exit velocity) and the measurements were taken at downstream locations from x/d = 40 to 80. Here, x and r are the axial and radial coordinates, respectively. The visible flame length was at about x/d = 84 and the stoichiometric flame length, estimated based on data in the TNF database, was at about x/d = 60. Some of these data were shown in Wang et al. (2004).

4.2 THERMAL DIFFUSIVITY

The thermal diffusivity is generally estimated by scaling the value for air to the elevated local temperature. For example, Effelsberg et al. (1988) and Everest et al. (1995) used $\alpha_C = \alpha_{air}\left(T/T_0\right)^{1.8}$, Caldeira-Pires and Heitor (1998) used $\alpha_C = 3.70\times10^{-6}\left(T\right)^{1.714}$ instead.

For centerline measurements of thermal dissipation in the current study, the thermal diffusivity $\alpha_C[m^2/s]$ based on the mixture composition at local flame temperature T was calculated from

$$\alpha_C = \alpha_{C0}\left(T/T_0\right)^{1.723} , \tag{4.1}$$

where $\alpha_{C0}[m^2/s]$ is the centerline thermal diffusivity of the mixture composition from the TNF database calculated at room temperature T_0 using the online "Transport Property Evaluation" package at http://navier.engr.colostate.edu/tools/.

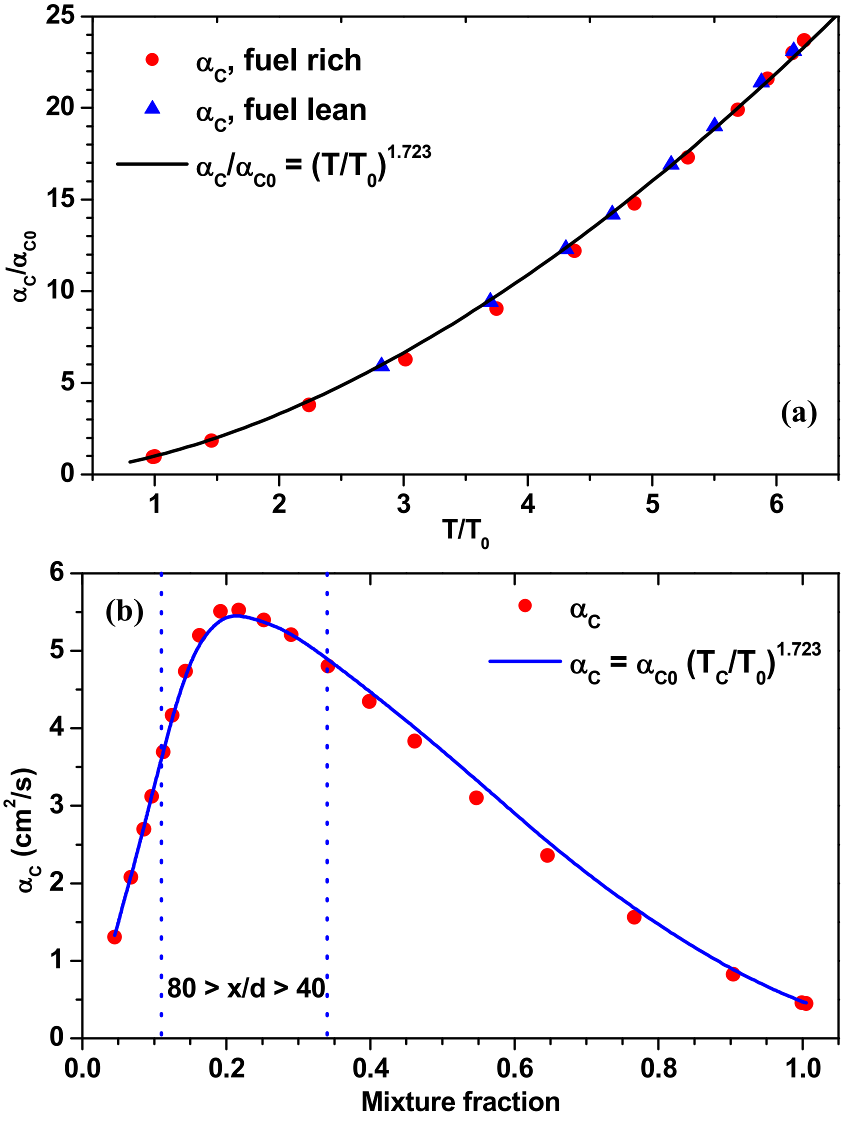

Figure 4.1 Thermal diffusivity $\alpha_C = \alpha_{C0}\left(T_C/T_0\right)^{1.723}$, where α_{C0} is the thermal diffusivity at T_0 of the mixture composition at T_C. (a) fuel rich and fuel lean sides, (b) in mixture fraction space

The exponent 1.723 was determined from the curve fit of α_C/α_{C0} to T/T_0 as shown in Fig. 4.1. Figure 4.1(a) shows the curve fitting by separating the fuel rich and fuel lean sides and Fig. 4.1(b) shows the fitted thermal diffusivity vs. thermal diffusivity calculated from the TNF workshop database in the mixture fraction space. The fitted curve shows good agreement with the thermal diffusivity from the TNF workshop database when the centerline thermal diffusivity was normalized by the centerline thermal diffusivity at room temperature.

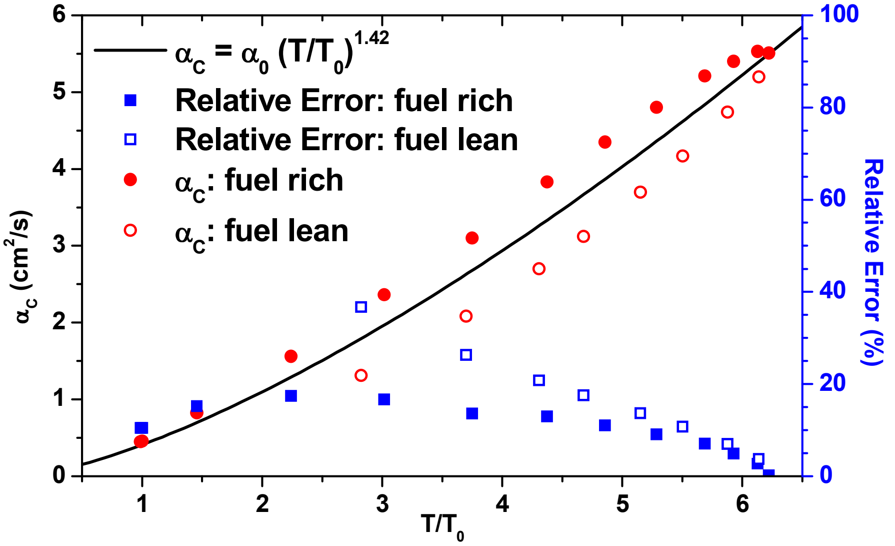

Figure 4.2 Thermal diffusivity $\alpha_C = \alpha_0 \left(T_C / T_0\right)^{1.42}$, where α_0 is the thermal diffusivity of the fuel combination at T_0

The estimation of thermal diffusivity for measurements of radial profiles of the dissipation is complicated by the fact that temperature is measured in the current study, but not mixture fraction. At any radial location the measured instantaneous temperature can correspond to a local mixture that is either rich or lean and thermal diffusivity depends on both mixture fraction and temperature. The curve fit in Fig. 4.1(a) requires that α_{C0}, and hence mixture fraction, be known. Figure 4.2 shows that the thermal diffusivity data cannot be correlated as well if only temperature is know because α_c has a different dependence on temperature depending on whether the mixture fraction is on the lean or rich side of stoichiometric. Thus there is additional uncertainty in the computed thermal dissipation when using a single curve fit for both the rich and lean curves. Figure 4.2 shows that if we estimate the diffusivity based on temperature only, then the relative error in calculating the thermal diffusivity is typically less than 20% but can be as much as 40% at temperatures of about 1000 K. The impact of variations in the thermal diffusivity on the accuracy of thermal dissipation measurements will be discussed further in section 4.5.6.

4.3 RESOLUTION ESTIMATION

The finest spatial structures in the scalar field are of order the Batchelor scale which is defined as

$$\lambda_B = \eta \, Sc^{-1/2}. \tag{4.2}$$

where $\eta = \left(\nu^3/\bar{\varepsilon}\right)^{1/4}$ is the Kolmogorov scale, ν is the kinematic viscosity, $\bar{\varepsilon}$ is the mean rate of kinetic energy dissipation and $Sc = \nu/D$ is the Schmidt number. Using measurements of $\bar{\varepsilon}$ in nonreacting round jets by Friehe et al. (1971), the Batchelor scale can be shown to be equal to

$$\lambda_B = 2.3\delta \, Re_\delta^{-3/4} \, Sc^{-1/2}. \tag{4.3}$$

where Re_δ is the local Reynolds number defined as

$$Re_\delta = \overline{U}_C \delta / \nu_C , \tag{4.4}$$

with $\overline{U}_C$ the jet centerline mean velocity and δ the full width at half maximum (FWHM) of the velocity profile. The jet exit Reynolds number is defined as,

$$Re_d = U_0 d / \nu_0 \tag{4.5}$$

which is approximately equal to Re_δ in non-reacting jet, but not necessarily so in jet flames. Muniz and Mungal (2000) showed that the local Reynolds number Re_δ will decrease with increasing downstream locations, e.g., Re_δ = 3,000 at $x/d = 20$, and Re_δ = 1,000 at $x/d = 80$.

For time-series measurements, the highest frequency present in the flow is expected to be the "convective" Batchelor frequency (Bernard and Wallace, 2002; Mi and Nathan, 2003),

$$f_B = \overline{U}/(2\pi\lambda_B), \tag{4.6}$$

where $\overline{U}$ is the local mean velocity. Note that the Batchelor frequency can be quite large in jet flames and is not always resolved because SNR considerations usually necessitate relatively low bandwidths. To estimate f_B in this study, the mean velocities were taken from Schneider et al. (2003) and the TNF workshop database. Since the experimental data from Schneider et al. (2003) only covered particular downstream locations, their data were extrapolated to get velocity values for the specific downstream locations used in this study.

The centerline mean velocity decay for nonreacting jet flows can be correlated with distance from the jet exit as

$$\overline{U_C}/U_0 = C_1\,(x/d^*)^{-1}, \tag{4.7}$$

where $C_1 \approx 6.2$ is a constant (Chen and Rodi, 1983) and d^* is the *jet source diameter* defined as

$$d^* = d\,(\rho_j/\rho_\infty)^{1/2}, \tag{4.8}$$

where ρ_j and ρ_∞ are the density of the jet and the coflow air respectively. Review of experimental results from Chen and Rodi (1983) showed that C_1 is independent of the density ratio (ρ_j/ρ_∞). In turbulent jet flames, the centerline mean velocity decay is more complicated than non-reacting jets due to effects of heat release, buoyancy and chemical reactions etc. There has been some theoretical work and modeling directed towards the development of a general decay law for the mean velocity in jet flames, e.g. the momentum conservation analysis by Becker and Yamazaki (1978), the simple mixing model by Tacina and Dahm (2000), and the density transformation similarity solution by Peters and Donnerhack (1981), Peters and Götgens (1991) and Peters (2000). The fundamental idea behind all these models is to find a *flame source diameter* d^+ to replace the *jet source diameter* d^* in Eqn. (4.7) such that most experimental data can be collapsed. Unfortunately, these theories and models can only collapse some datasets and fail on others and there is no consensus on the correct *flame source diameter* d^+. Since all of the models and most measurements support a x^{-1} scaling for the decay of centerline velocity in momentum driven jet flames, we curve fit the data of Schneider et al. (2003) to the following relation

$$\overline{U_C}/U_0 = C_2\,(x/d)^{-1}. \tag{4.9}$$

The data and curve fit are shown in Fig. 4.3(a). It can be seen that the curve-fitted formula $\overline{U_C}/U_0 = 14.30\,(x/d)^{-1}$ agrees well with experimental data from downstream locations *x/d* = 25 to 63. The least square fit gives an uncertainty (95% confidence) in C_2 of ± 0.4%. This uncertainty in C_2 leads to an uncertainty in the extrapolated velocity (at *x/d* = 80) of ± 0.4%.

The local characteristic length scale, i.e. the full-width half-maximum of the velocity profile δ, can be correlated with distance from the jet exit via

$$\delta/d = C_3\,(x/d)\,. \tag{4.10}$$

Experimental data from Schneider et al. (2003) were curve fitted and the result $\delta/d = 0.132\,(x/d)$ is shown in Fig. 4.3(b). It is nearly a linear relation for downstream locations between *x/d* = 20 and 60. The least square fit gives an uncertainty (95% confidence) in C_3 of ± 1.5% which leads to an uncertainty in the extrapolated FWHM of the velocity profile (at *x/d* = 80) of ± 1.5%.

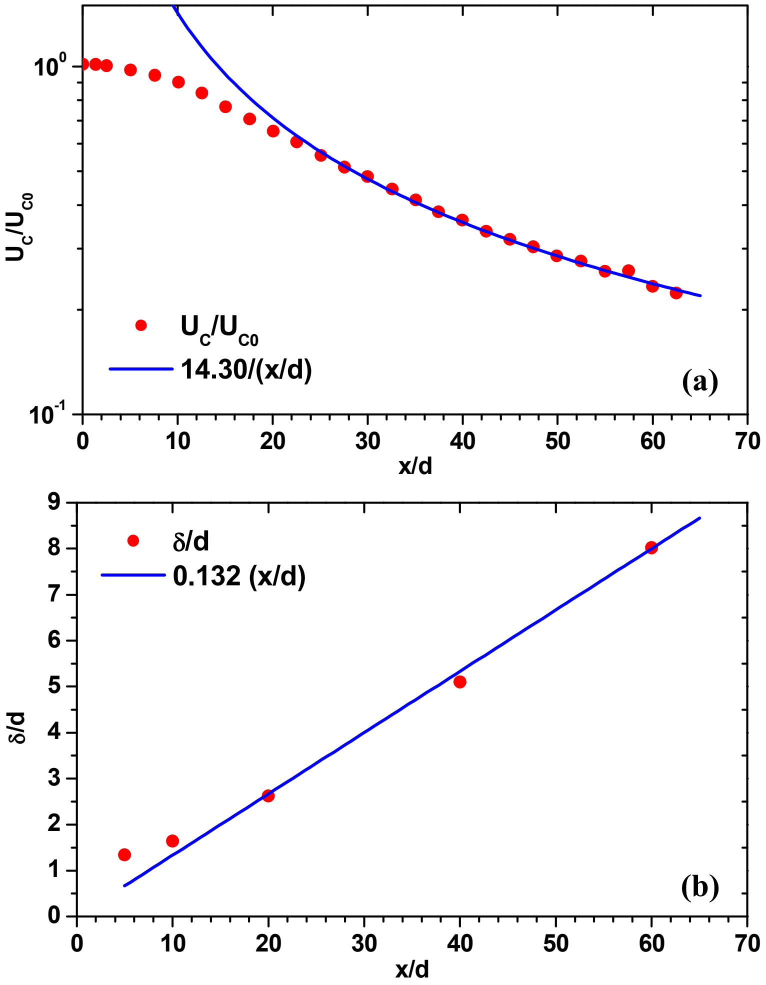

Figure 4.3 Scaling laws for DLA A flame from Schneider et al. (2003), (a) mean centerline velocity, (b) FWHM of velocity profile

With above information, the local Reynolds number, Batchelor scale and frequency were estimated based on Eqns. (4.3), (4.4) and (4.6). These estimated quantities are given in Table 4.1.

Figure 4.4 shows the local Reynolds number variation along the jet flame centerline between x/d = 40 and 80. It can be seen that the estimated local Reynolds numbers are about only 2,500 and the lowest local Reynolds number is about 2,250 at x/d = 60 (a location that is very close to the stoichiometric flame length). There is a significant decrease from the jet exit Reynolds number (15,200) to the local Reynolds number of 2,800 at x/d = 40. The local Batchelor scale scales as $Re_{\delta}^{-3/4}$, and therefore the resolution requirement will be relatively more stringent for measurement locations close to the jet exit.

Table 4.1 Jet flame conditions and estimates of resolution requirements. (Velocity data from Schneider et al. (2003), U_{C0} = 51.6 m/s is the mean jet exit centerline velocity which is different from the mean jet exit velocity U_0; temperature data from TNF workshop database)

x/d	T_C (K)	ν_C (cm^2/s)	U_C/U_{C0}	δ/d	Re_δ	λ_B (mm)	f_B (kHz)
40	1565	2.9415	0.365	5.33	2727	0.260	11.5
45	1684	3.2547	0.324	6.00	2465	0.316	8.4
50	1755	3.4301	0.292	6.67	2339	0.365	6.6
55	1814	3.5670	0.265	7.33	2249	0.413	5.3
60	1842	3.6091	0.243	8.00	2223	0.455	4.4
65	1817	3.4662	0.224	8.67	2314	0.478	3.9
70	1740	3.1878	0.208	9.33	2516	0.483	3.5
75	1629	2.8302	0.195	10.00	2834	0.474	3.4
80	1525	2.5211	0.182	10.67	3182	0.463	3.2

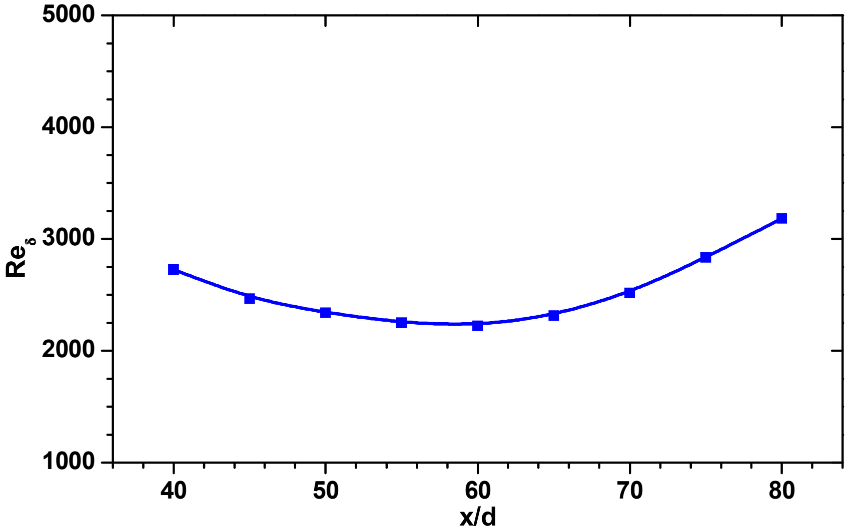

Figure 4.4 Variation of estimated local Reynolds number along jet flame centerline

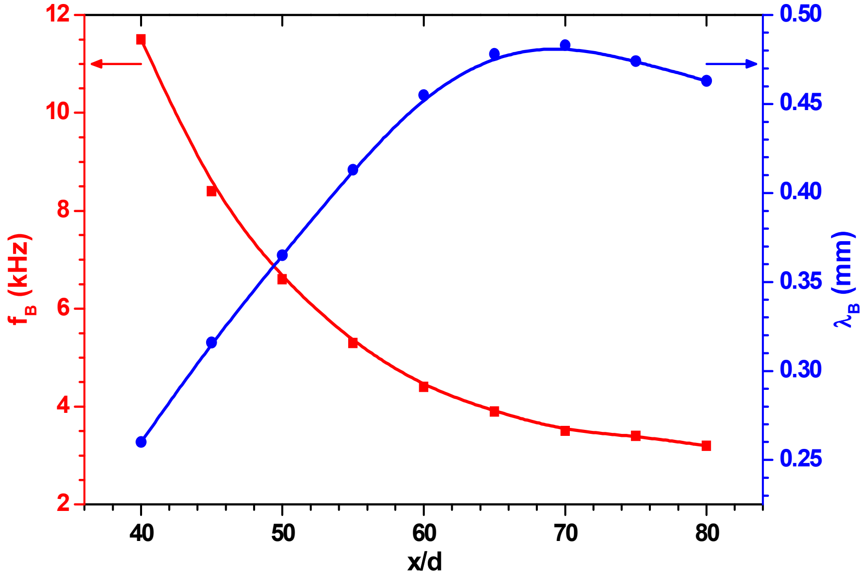

Figure 4.5 Variation of estimated local Batchelor length and time scales along the jet flame centerline

Figure 4.5 shows the variation of the local Batchelor scale and Batchelor frequency along the jet flame centerline. It can be seen that the current two-point spatial separation of 300 μm is nearly equal to λ_B at $x/d = 45$ and is about a factor of 1.5 smaller than λ_B farther downstream. At $x/d = 40$, the estimated Batchelor scale is about 0.26 mm which is about 86.7% of the current resolution. Based on the non-reacting circular turbulent jet results of Mi and Nathan (2003), the estimated error in the measured mean scalar dissipation rate will be only 3%. Therefore, the spatial resolution of the current experiments is considered to be high enough for all downstream measurement locations, i.e. the radial gradient measurement is fully spatially-resolved.

The convective Batchelor frequency f_B is about twice the frequency resolution (cut-off frequency $f_C = 0.5f_s = 5$ kHz) at $x/d = 40$ and the errors in the axial dissipation are expected to be about 10% according to Mi and Nathan's results (2003). The sampling frequency of this study is sufficient to resolve the convective Batchelor frequency (and hence the Batchelor scale) along the centerline for $x/d \geq 60$. The measurements were limited to stations of $x/d = 40$ and larger so that the resolution of the dissipation scales could be maintained, at least for the radial gradient.

4.4 SINGLE POINT RESULTS

4.4.1 Mean and fluctuation temperature

Figure 4.6 shows measured mean and *rms* radial temperature profiles at three downstream stations ($x/d = 40$, 60 and 80). The temperature profiles from the TNF workshop database (both SANDIA and DLR dataset) are also shown for comparison, and it is seen that the current measurements of both mean and *rms* radial profiles agree well with both datasets especially in the near field regions, e.g. $x/d = 40$. Further downstream, e.g. $x/d = 80$, the agreement is not as good as at $x/d = 40$.

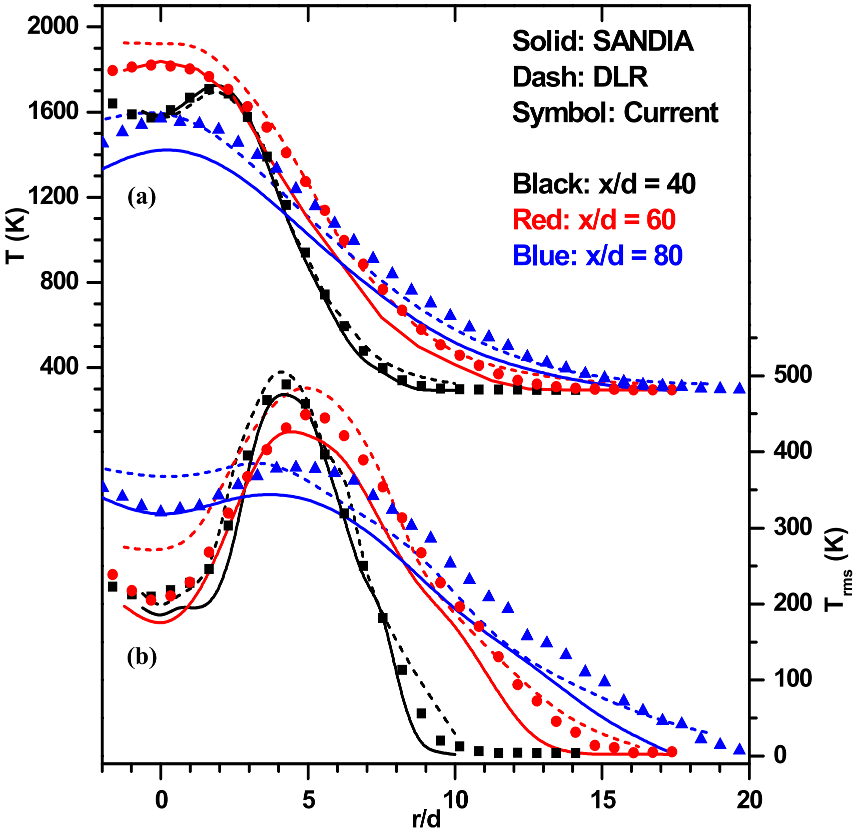

Figure 4.6 Radial profiles of (a) mean and (b) rms temperature at three different axial stations ($x/d = 40, 60, 80$). Data from TNF workshop data base (SANDIA and DLR datasets) were shown for comparison.

One possible reason is because of the different coflow geometry used in the different studies. The current setup has a square test section with 280 mm by 280 mm cross-section which is about twice the size of the standard DLR_A flame with a circular coflow and radius of 140 mm. The shear layer generated between the coflow and room air will develop with increasing downstream distance and will finally merge at the center at some distance downstream. For example, Raguraman et al. (2004) used the standard DLR_A burner and obtained Rayleigh measurements only up to *x/d* = 40. The current setup does better in reducing the interference from the shear layer interactions and enables measurements to be made farther downstream.

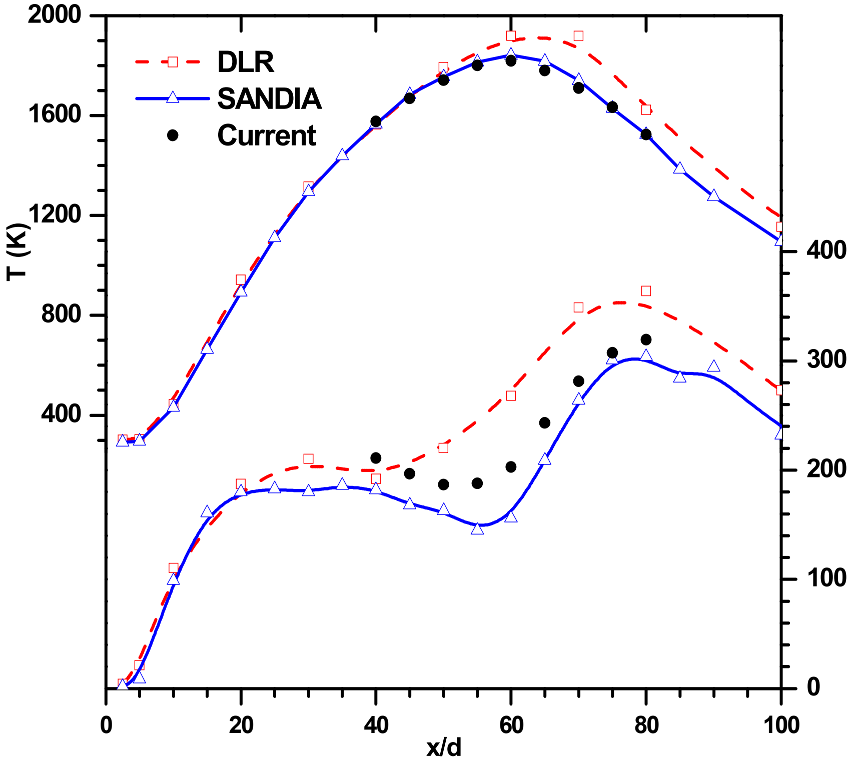

Figure 4.7 Axial profiles of (a) mean and (b) *rms* temperature at three different axial stations (*x/d* = 40, 60, 80). Data from TNF workshop data base (SANDIA and DLR datasets) were shown for comparison

Figure 4.7 shows the axial profiles of the measured mean and *rms* temperature profiles along the jet centerline. The mean centerline temperature agrees well with the SANDIA dataset and is lower than the DLR dataset for downstream locations $x/d \geq 50$. The current *rms* temperature data tend to lie between the SANDIA and DLR values.

4.4.2 Temperature autocorrelation function and turbulent time scales

The auto-correlation function was calculated from the time-series data and was corrected for noise effects based on the procedure discussed in Chapter 3. The integral time scale is calculated from the auto-correlation function $R(\tau)$ via

$$\tau_I = \int_0^\infty R(\tau)d\tau \; . \qquad (4.11)$$

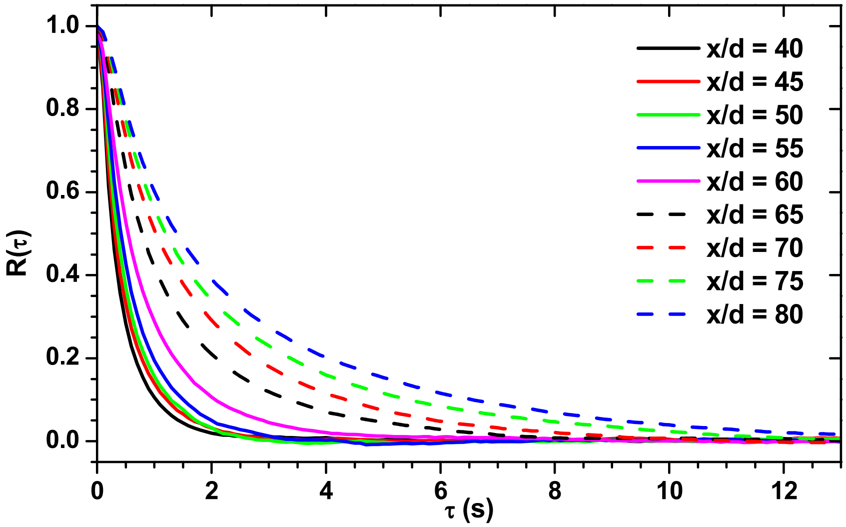

Figure 4.8 Auto-correlation functions at the jet flame centerline

Figure 4.8 shows the calculated autocorrelation functions on the centerline at downstream locations of x/d = 40 to 80. The area under the auto-correlation function keeps increasing with increasing downstream distance, which implies that the integral time scale increases as well.

This is seen quantitatively in Fig. 4.9, which shows the variation of the integral time scale at the centerline for different downstream locations. As expected, the integral time scale increases with increasing downstream distance. In a non-reacting jet the integral scale is expected to scale as $\delta/U_c \sim x^2$, and Fig. 4.9 shows that this may be approximately the case. The current integral time scales based on temperature fluctuations seem to agree with the integral time scales computed from OH concentration time-series measured by Raguraman et al. (2004) in a similar flame. For example, their integral time scales for OH time-series is 0.5ms at *x/d* = 40, which are in good agreement with Fig. 4.9.

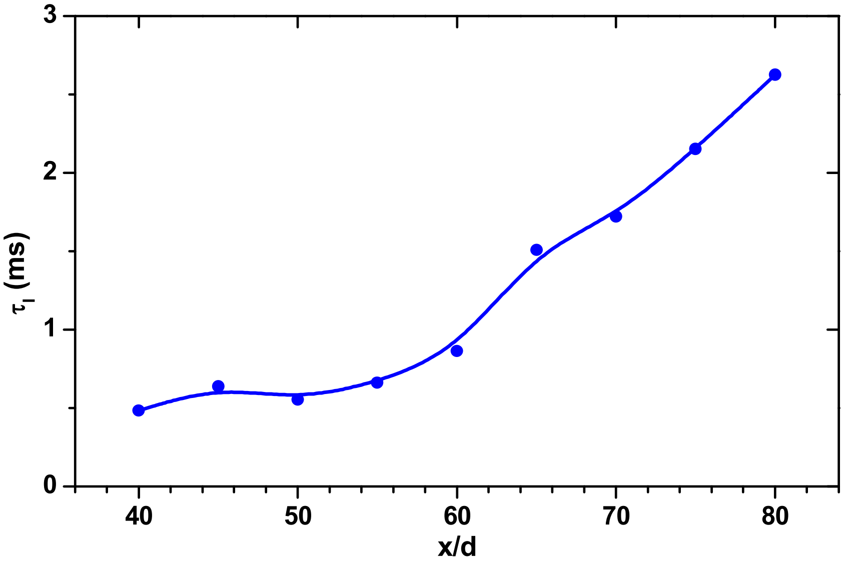

Figure 4.9 Integral time scale for at the jet flame centerline

We can compare the integral time scale to the outer-scale and Batchelor time scales, where the outer time scale is defined as

$$\tau_\delta = \delta / \overline{U_C}\,, \tag{4.12}$$

and the Batchelor time scale is defined as

$$\tau_B = 1/f_B\,. \tag{4.13}$$

The outer time scale can be determined based on the velocity measurement and the scaling laws developed in section 4.3. The Batchelor time scale can be calculated from the estimated Batchelor frequency from section 4.3 as well.

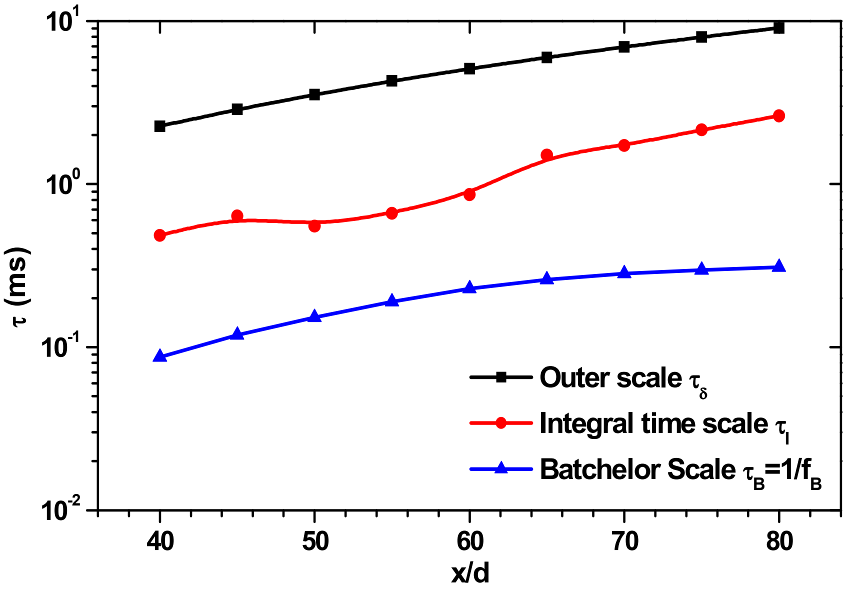

Figure 4.10 Comparison of the outer, integral and Batchelor time scales along the jet flame centerline

Figure 4.10 compares these three time scales. All three time scales follow the same trend in the semi-log plot, i.e. they increase with increasing downstream distance. The dip in the axial profile of the integral time scale near *x/d* = 50-60 is probably related to the proximity of the measurements to the stoichiometric flame tip, which occurs at *x/d* = 60. Near the reaction zone, temperature is not simply a passively transported scalar as is essentially the case on centerline for locations upstream or downstream of the flame tip. The reaction zone is associated with thin regions of high temperature and so should exhibit a reduced integral length scale as compared to either fuel rich or fuel lean regions of the flow.

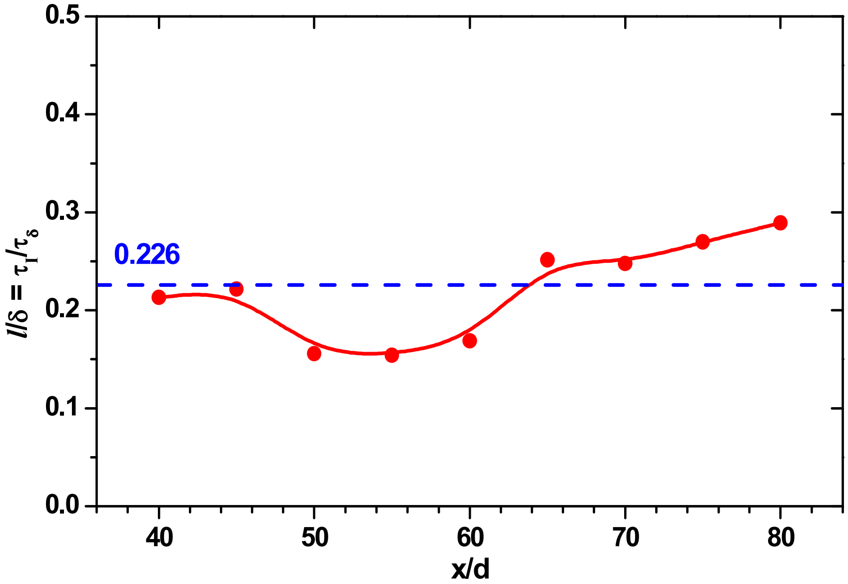

Figure 4.11 Ratio of outer to integral length scale along the jet flame centerline

The integral length scale *l* is a classical large scale of the flow, which is the characteristic scale of the energy containing eddies (Libby, 1996). Here, the integral length scale is assumed to be related to the integral time scale as follows

$$l = \overline{U_C}\tau_I \,. \tag{4.14}$$

The ratio of the integral scale l and outer scale δ should be a constant because they are both outer scales

$$\frac{l}{\delta} = \frac{\overline{U_C}\tau_I}{\overline{U_C}\tau_\delta} = \frac{\tau_I}{\tau_\delta}. \tag{4.15}$$

Figure 4.11 shows how this ratio varies with the increasing downstream distance on the jet flame centerline. Wygnanski & Fiedler (1969) conducted measurements in a round jet and found that at the jet centerline,

$$l = 0.226\,\delta \tag{4.16}$$

where l is the integral length scale based on the autocorrelation of the velocity fluctuations and δ is the full width at half maximum of the velocity profile. The current integral length scale calculated based on the integral time scale from the autocorrelation function of the fluctuating temperature varies around $0.226\,\delta$ with increasing downstream locations. This implies that the integral length scale calculated here is close to that calculated from the fluctuating velocity. This ratio behaves similarly in both non-reacting and reacting flows.

4.4.3 Outer-scale estimates of the Batchelor scale

The most commonly used Reynolds number in classical turbulence theory is the "*turbulence Reynolds number*" Re_l, defined as

$$Re_l = \frac{u_{rms}l}{\nu}. \tag{4.17}$$

As discussed in Chapter 1, the relation between the Kolmogorov scale λ_K and the integral scale l of a flow can be expressed as

$$\lambda_K / l = 1.2\,Re_l^{-3/4} \tag{4.18}$$

using this Reynolds number definition, and the corresponding Batchelor scale is

$$\lambda_B / l = 1.2\, Re_l^{-3/4}\, Sc^{-1/2} . \qquad (4.19)$$

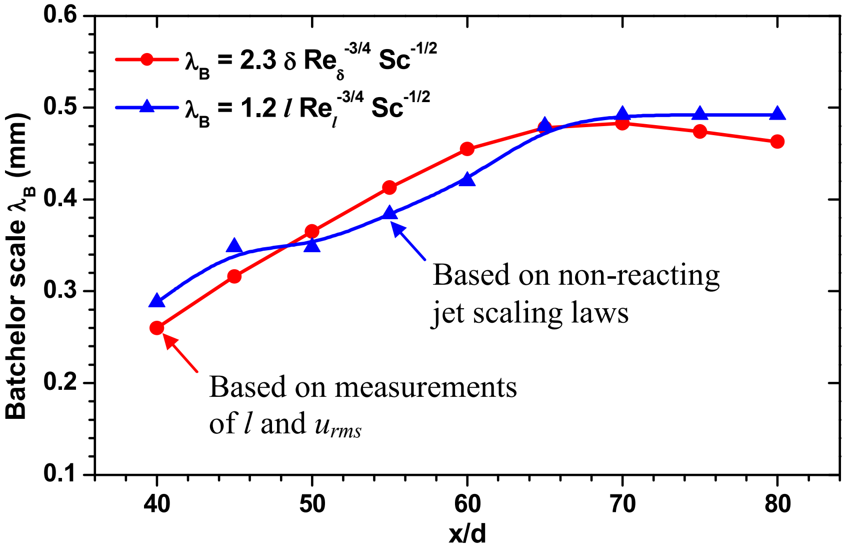

Figure 4.12 Comparison of the Batchelor scale estimated from the integral length scale and from non-reacting jet scaling laws in section 4.3

The Batchelor scale based on the integral length scale is shown in Fig. 4.12 and compared to the estimated Batchelor scale from Section 4.3. It can be seen that estimated Batchelor scales from both methods follow the same trend and have nearly the same value with a maximum relative difference of about 10%. This result suggests that the estimation method proposed in section 4.3 based on the relation in non-reacting flow with the substituted local Reynolds number can be used to estimate the Bachelor scale in turbulent non-premixed jet flames with fairly good accuracy. This result is not surprising because the scaling of the centerline mean velocity and the jet flame velocity width follow scaling laws similar to those in non-reacting flows.

4.4.4 Higher order moments

Radial variations in the third and fourth moments of the temperature (skewness and kurtosis, respectively) are shown in Figs. 4.13 and 4.14. The values of skewness and kurtosis for a Gaussian distribution are 0.0 and 3.0 respectively, shown as dotted lines in the figures. For any symmetric distribution, the skewness value is close to zero. Negative skewness implies that the left tail is heavier than the right tail in the distribution and vice versa. When kurtosis is greater than three, the distribution is more "peaked" than a Gaussian distribution. Conversely, if the kurtosis is less than three, the distribution is more "flat" than Gaussian.

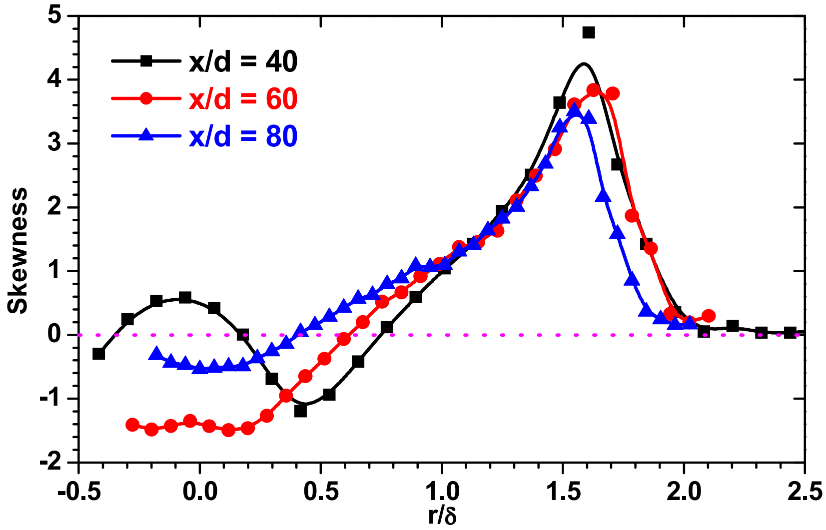

Figure 4.13 Radial profiles of skewness at *x/d* = 40, 60 and 80. The dotted line indicates the skewness value for a Gaussian distribution which is 0.

At the centerline, the skewness has a slight positive value at *x/d* = 40, slight negative value at *x/d* = 80 and a relatively large negative value at *x/d* = 60.

These are different from results in non-reacting jet flows where skewness is slightly negative at all axial locations. Both radial profiles of skewness and kurtosis at *x/d* = 80 are very close to those in non-reacting jet flows. This is not surprising because at this downstream location, which is well past the stoichiometric flame tip, the jet is essentially non-reacting. Outward from the centerline, skewness and kurtosis increase rapidly at approximately the same radial location ($r/\delta = 1.6$), which is the outer edge of the jet. The rapid increase in skewness and kurtosis in the intermittent mixing region is due to the passage of cold air past the measurement volume.

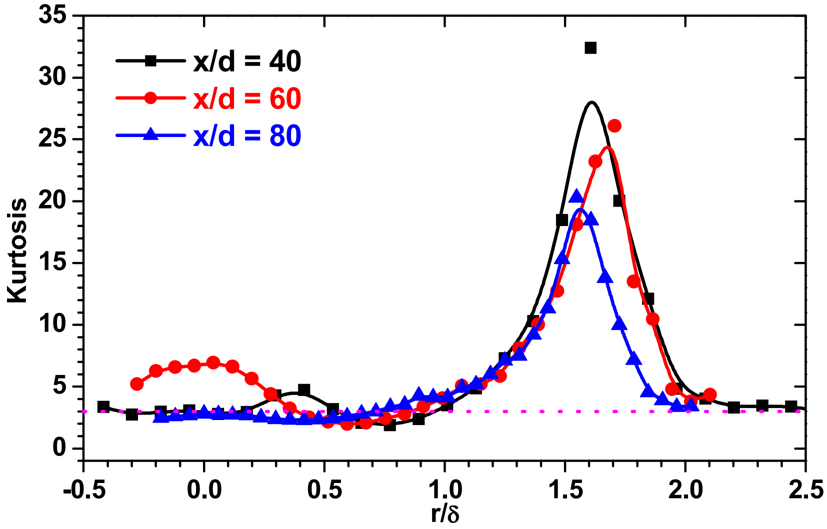

Figure 4.14 Radial profiles of kurtosis at *x/d* = 40, 60 and 80. The dotted line indicates the kurtosis value for a Gaussian distribution which is 3.

At the stoichiometric flame length, e.g. *x/d* = 60, skewness has a larger negative value and kurtosis has a larger positive value. Interestingly, for the radial profile *x/d* = 40, the local reaction zone is at $r/\delta = 0.4$ approximately, where the local temperature is the highest. Here, skewness has a larger negative value and kurtosis has a larger positive value as well. It appears then, that this is an indication of the presence of the reaction zone.

The centerline variations in skewness and kurtosis are shown in Fig. 4.15. The present results show that the skewness decreases from 0.5 at *x/d* = 40 to –1.4 at *x/d* =60 and then increases to –0.5 at *x/d* = 80. In non-reacting C_3H_8-air jets, Schefer and Dibble (2000) found that the centerline skewness of the mixture fraction increases from –0.45 at *x/d* =15 to –0.31 at *x/d* = 50. Similar results were found by Pitts and Kashiwagi (1993) in nonreacting CH_4-air jets. These previous measurements in non-reacting flows are clearly different from the current temperature measurement in a turbulent jet flame.

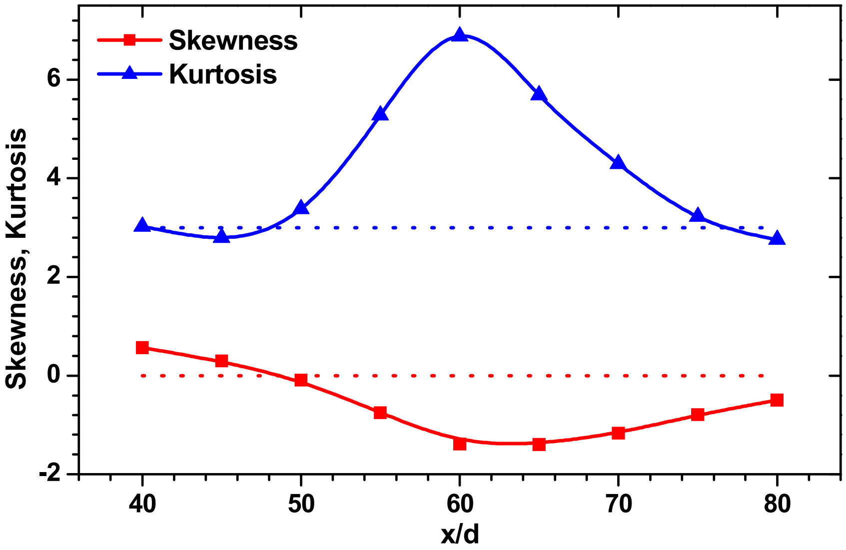

Figure 4.15 Centerline Skewness and Kurtosis for *x/d* = 40 to 80. The dotted line indicates the skewness and kurtosis values for a Gaussian distribution which are 0 and 3 respectively.

4.4.5 Temperature Probability Density Function (PDF)

Probability density functions (PDF) of the temperature were calculated from the time-series data. The PDFs were computed using 360k samples at each spatial location and 155 bins equally spaced over four standard deviations of the data. The PDFs have been normalized so that

$$\int_{T_{min}}^{T_{max}} PDF(T)dT = 1. \qquad (4.20)$$

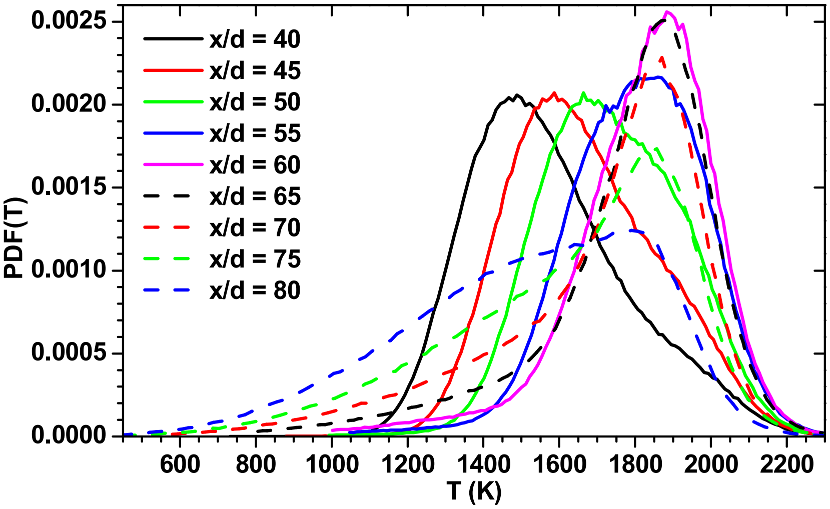

Figure 4.16 Possibility density functions of temperature at the jet flame centerline

The evolution of *PDF*(*T*) along the centerline is shown in Fig. 4.16. At the farthest upstream location (*x/d* = 40), the peak *PDF*(*T*) is around *T* = 1450 K and the distribution is skewed towards the high temperature end, which corresponds to the mixing of the cold fuel with the hot products. The skewed distribution continues downstream till *x/d* = 55 at which point the distribution becomes more Gaussian. Downstream of *x/d* = 60, which is approximately the stoichiometric flame length, the peak of the PDFs remains at *T* = 1900 K, but the distribution becomes skewed toward lower temperature values owing to mixing of the hot products with the cold coflow air.

4.4.6 Temperature Power Spectral Density (PSD)

The power spectral density functions shown here are all for the normalized fluctuating temperature

$$T'^{*} = \left(T - \overline{T}\right)/T_{rms} \tag{4.21}$$

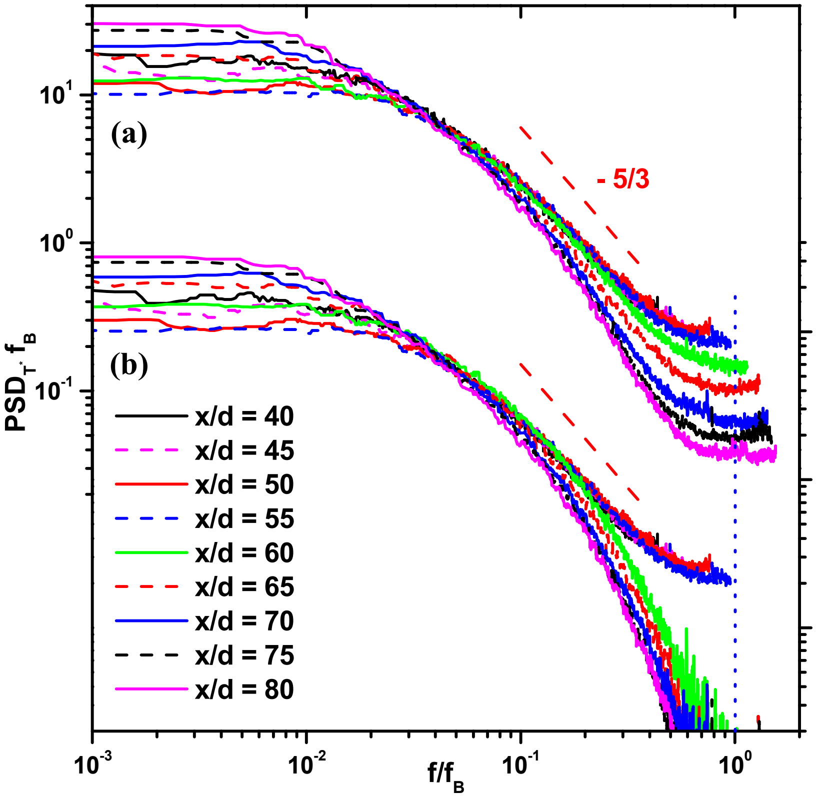

Figure 4.17 Normalized fluctuating temperature power spectra at the jet flame centerline (a) without noise floor correction; (b) after noise floor correction (except for *x/d* < 55)

Normalized fluctuating temperature PSDs along the jet flame centerline are shown in Fig. 4.17. Figure 4.17(a) shows the PSDs without the noise-floor correction and Fig. 4.17(b) shows the PSDs with the noise-floor correction except for $x/d < 55$ where the sampling frequency was not sufficient to resolve the Batchelor frequency and the noise floor. The correction procedure was discussed in Chapter 3 and is based on the procedure developed by Renfro et al. (1999, 2000). The frequency is normalized by the convective Batchelor frequency, and the power spectral density is normalized by $1/f_B$. All of the spectra exhibit a similar appearance: they are relatively flat at low frequency, begin rolling off for $f/f_B > 10^{-2}$, and then roll-off more rapidly in the dissipation range ($f/f_B > 0.2$). An inertial subrange, where the power scales as $f^{-5/3}$, characterizes scalar spectra in high Reynolds numbers non-reacting jet flows, e.g. Dowling (1991), Dowling and Dimotakis (1990), and a line that follows this scaling is shown as reference. Figure 4.17 shows the spectra along the centerline exhibit only a small inertial subrange (if any), likely because the local Reynolds number at all locations is only about 2,500 (shown in Fig. 4.4).

A large inertial-subrange is a well known signature of fully developed turbulence and measurements of mixture fraction fluctuations clearly show this range diminishing with decreasing Reynolds number (Dowling and Dimotakis, 1990). The farthest upstream location seems to exhibit a more extended inertial subrange, but that spectrum is not corrected for noise and that seems to contribute to the apparent power law dependence. Figure 4.17 also shows that the spectra collapse relatively well in the dissipation range near $f/f_B = 1$. This is significant because it suggests that the estimate of the Batchelor scale is largely correct, and that the dissipation range is apparently resolved. Note, however, that no dissipation range is observed at *x/d* = 40 because the sampling frequency was not high enough to resolve it. This conclusion is consistent with the Batchelor frequency estimates shown in Table 4.1.

Figure 4.18 shows the same PSDs normalized by the integral time-scale τ_I and outer-time scale τ_δ. The spectra in Fig. 4.18(b) exhibit a steeper roll-off than the –5/3 power law at a non-dimensional frequency of about 5, which is consistent with measurements of mixture fraction fluctuations in non-reacting jets (Dowling and Dimotakis, 1990). However, in the nonreacting jet studies of Dowling and Dimotakis (1990), the dissipation range could not be collapsed with this outer-scale normalization of the frequency. This latter result is different from result shown in Fig 4.18(a) and (b) when the frequency is scaled by the integral and outer time scales. Renfro et al. (1999, 2000) also found that OH fluctuation spectra could be collapsed over the entire frequency range with integral-scale normalization, which is similar to the result in Fig. 4.18(a).

The explanation of this difference between the non-reacting and reacting results has to do with the small Reynolds number range studied in the reacting case. As discussed in the resolution estimation section, the local Reynolds number for the current measurement locations is essentially constant at 2,500. The ratio of the Bachelor time scale and the outer time scale is

$$f_B \tau_\delta = \overline{U} / (2\pi\lambda_B) \cdot \delta / \overline{U} = \delta / (2\pi\lambda_B) = \mathrm{Re}_\delta^{3/4}\, Sc^{1/2} / 4.6\pi \qquad (4.22)$$

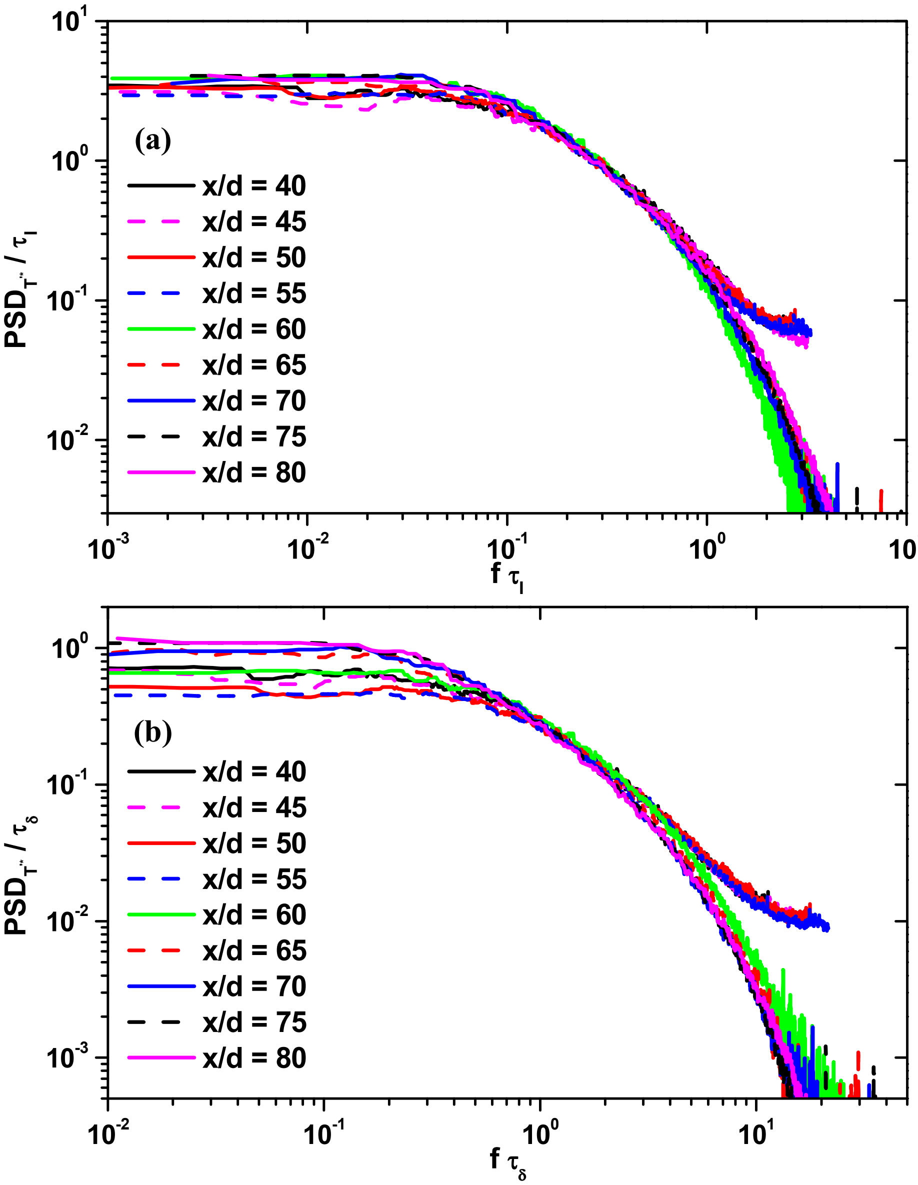

Figure 4.18 Normalized fluctuating temperature power spectra at the jet flame centerline (noise effects were corrected except for *x/d* < 55) (a) normalized by the integral time scale τ_I ; (b) normalized by the outer time scale τ_δ .

This indicates that for nearly constant local Reynolds number Re_{δ}, the fluctuating temperature PSD scaled by either the Batchelor frequency or the outer time scales will give essentially the same overlapping characteristics in the high frequency or dissipation end if the local flow fields of the jet flames have the same Reynolds number. This can also be seen in Fig. 4.10 when comparing outer, integral and Bachelor time scales. It is only when significantly different Reynolds number flows are compared that the importance of inner- versus outer-scale normalization becomes apparent.

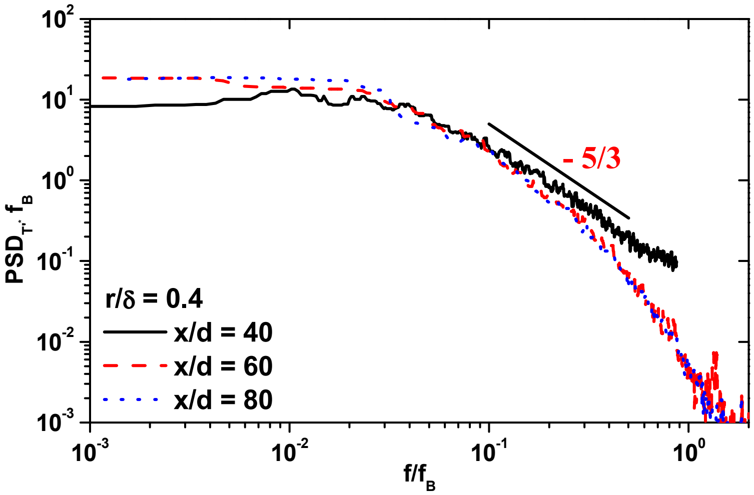

Figure 4.19 Fluctuating temperature power spectra along ray r/δ = 0.4 (corrected except at *x/d* = 40)

Figure 4.19 shows the power spectra at the same downstream locations but along the ray where $r/\delta = 0.4$, which is close to the region of maximum shear. The convective Batchelor frequency used in the normalization of the frequency was scaled by the local velocity. Figure 4.19 shows that, in contrast to the centerline locations, the spectra seem to exhibit an extended inertial-subrange. This observation of a larger power-law region for increasing radial location is similar to what has been seen in non-reacting jet scalar dissipation measurements (Lockwood and Moneib, 1980), and is likely related to the proximity to the peak shear region. This similarity with non-reacting jets is somewhat surprising at the $x/d = 40$ location, because the $r/\delta = 0.4$ location is near the reaction zone and so substantial turbulence damping by the increased viscosity is expected.

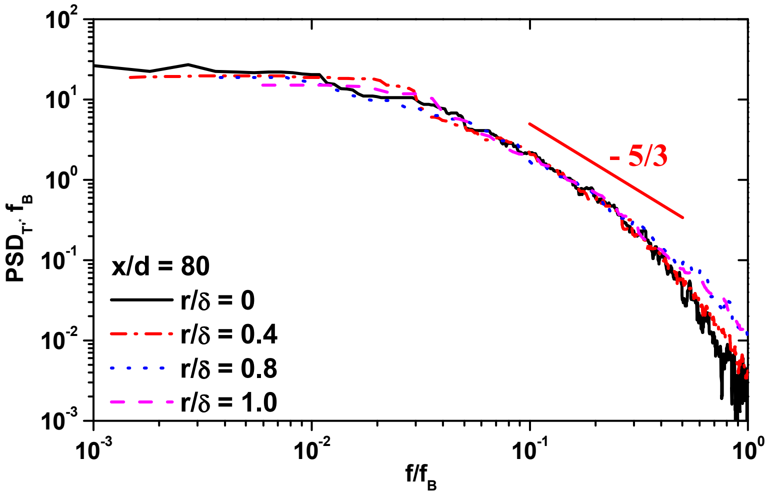

Figure 4.20 Fluctuating temperature power spectra at $x/d = 80$ and different radial locations, all corrected.

Figure 4.20 shows normalized temperature power spectra as a function of radial location at the $x/d = 80$ station, which is fully resolved. Note that this station is past the stoichiometric flame length and point of maximum centerline temperature. Although not entirely apparent from the figure, the spectra exhibit an increasing inertial-subrange with increasing radial location, and they collapse relatively well in the dissipation range. As mentioned previously, since this location is downstream of the stoichiometric flame tip it represents an effectively nonreacting flow, and so its characteristics should be similar to those of a low Reynolds number, nonreacting, low-density jet.

4.5 TWO-POINT RESULTS

All results discussed in section 4.4 can be obtained from single-point time-series measurements. In this section, the results from two-point time-series measurements will be discussed in detail. Representative two-channel temperature and radial thermal dissipation rate along the jet flame centerline at x/d = 40, 60 and 80 are shown in Fig. 4.21. This figure shows that the fluctuating temperatures measured by the two channels are very similar. This is expected since the probe spacing is of order the Batchelor scale, and the characteristic temperature difference across a thermal dissipation structure will be substantially less than T_{rms}. This can be seen by considering the scaling proposed by Tennekes and Lumley (1972). They argue that the gradient across a dissipation structure will scale as T_{rms}/λ_T, where λ_T is the Taylor microscale. This is a scaling law only, and does not represent the characteristic temperature difference or length scale at the dissipation scale. Instead we can argue that the gradient can be approximated as $\Delta T_B/\lambda_B$, where ΔT_B is the characteristic temperature difference across a dissipation structure. Combining these we have $\Delta T_B \sim T_{rms}\, \lambda_B \big/ \lambda_T \sim T_{rms} Re_\delta^{-1/4}$. In other words, the characteristic temperature difference will be approximately $Re_\delta^{-1/4}$ smaller than T_{rms}. For example, if $T_{rms} \approx 300$ K and assuming $Re_\delta \approx 2500$ then we have $\Delta T_B \approx 40$ K.

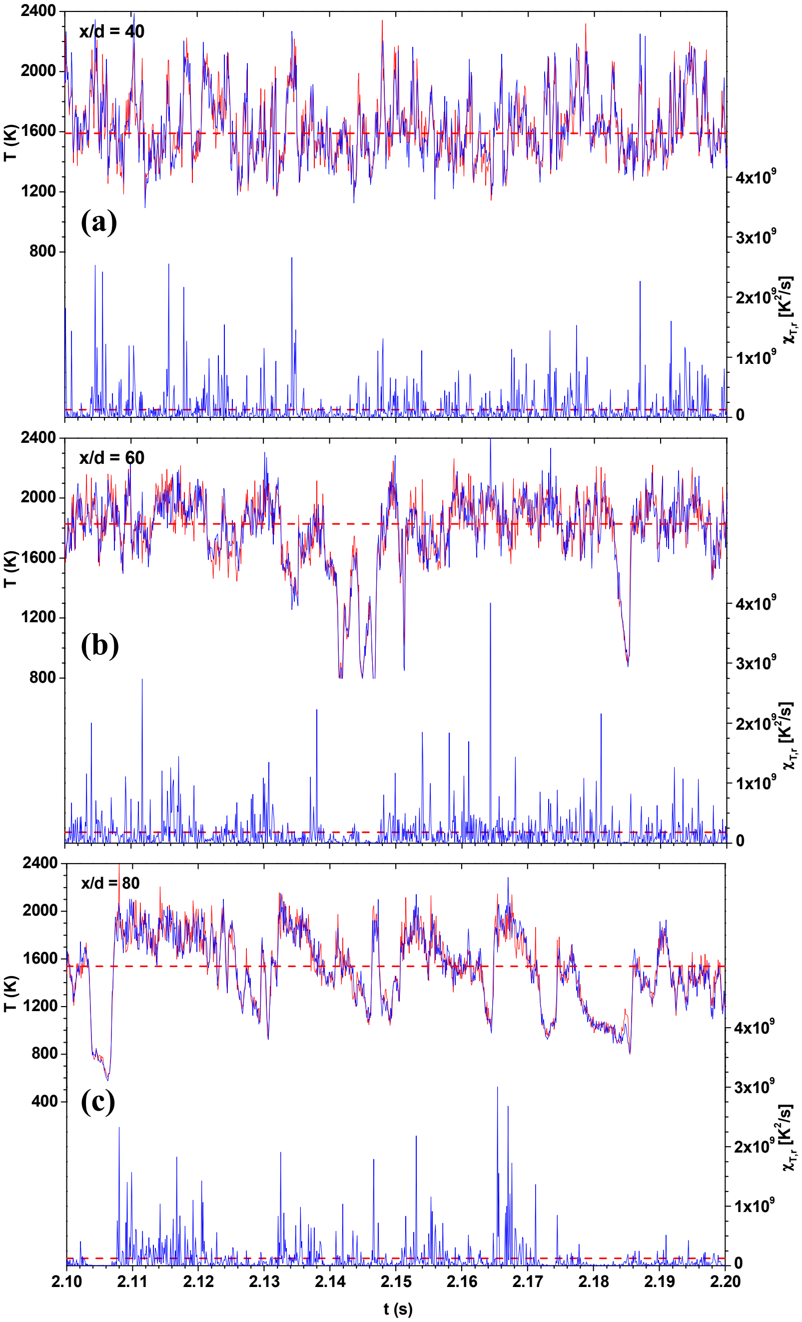

Figure 4.21 Representative two-channel temperature and radial thermal dissipation rate time-series at the jet flame centerline at *x/d* = 40, 60 and 80. Dash-lines are mean values of temperature and radial thermal dissipation rate.

Figure 4.21 provides a fairly stark demonstration of why the relevant signal-to-noise ratio for these types of measurements is the *difference* SNR as was shown in chapter 3. The characteristic temperature difference is quite small and so what is considered a good SNR for fluctuating temperature may not be good when considering the temperature difference measured by two closely spaced probes. The time-traces of the thermal dissipation are highly intermittent or spotty, and are consistent with scalar dissipation time traces measured in non-reacting flows (Dowling and Dimotakis, 1990).

4.5.1 Joint PDF of T_1 and T_2

Figure 4.22 shows $JPDF(T_1, T_2)$ of the temperature from two channels at the jet flame centerline. All these JPDFs are symmetric along the $T_1 = T_2$ line. This symmetry implies that temperature measurements from these two probes are statistically similar, which is expected since they are so closely spaced. As discussed in the resolution estimation section, the separation distance of the two probe volumes in the object plane is very close to the estimated Batchelor scale at x/d = 40 and smaller than the Batchelor scale further downstream. As the time-series showed, there are no large gradients across the Batchelor scale and these two probes should detect similar temperatures most of the time. Although the two probes record similar temperatures they are not identically the same. The fact that the JPDF becomes wider with increasing temperature indicates that there is an increasing difference between the temperatures of the two probes. This effect is expected since higher temperature regions should be associated with higher gradients at a given point where the Batchelor scale is largely the same.

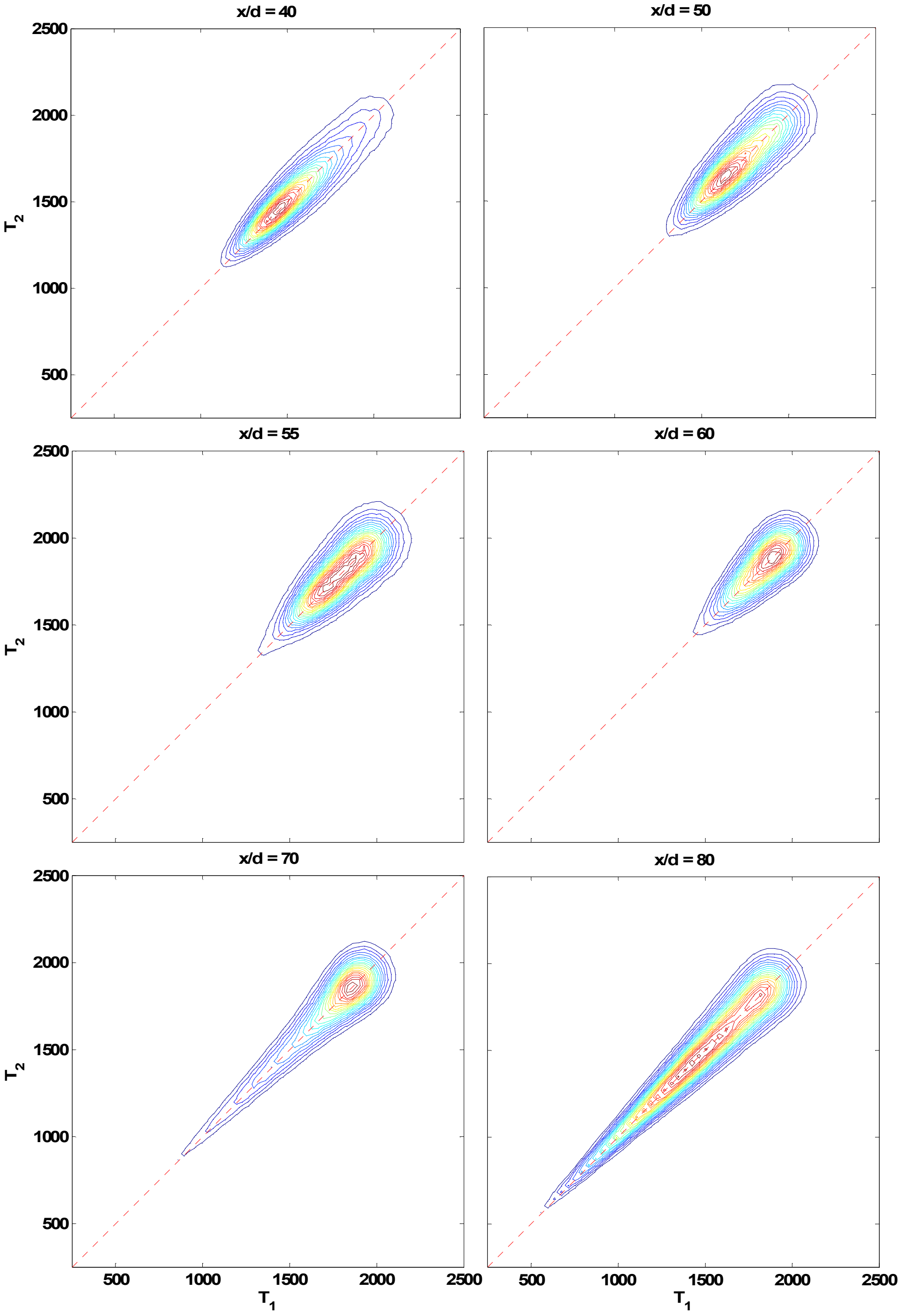

Figure 4.22 Joint PDF(T_1, T_2) at the jet flame centerline

4.5.2 PDF of temperature gradients

Figure 4.23 shows PDFs of the normalized temperature gradients in the radial direction at the jet centerline. At *x/d* = 60, 70 and 80, the semi-log plot shows that the PDFs are similar, which indicates the similarity of the gradients when normalized by T_C/λ_B. All the distributions appear to exhibit approximately exponential scaling of the tails (which should appear as a straight line in the semi-log plot). Exponential scaling is well documented in nonreacting turbulent flows and is a result of the intermittent nature of the scalar dissipation fluctuations (Gurvich and Yaglom, 1967).

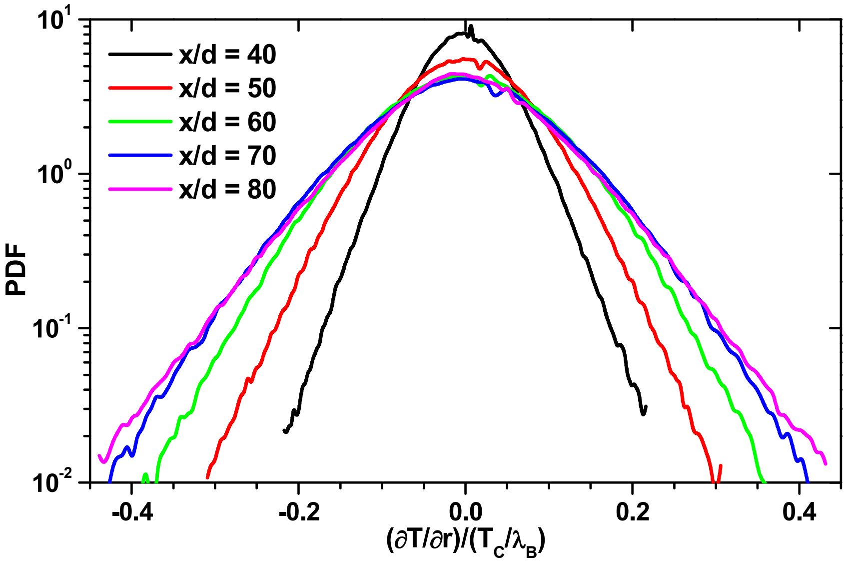

Figure 4.23 Probability density functions (PDFs) of the normalized radial temperature gradients along the jet centerline

Figure 4.23 also shows the gradient PDFs at the *x/d* = 40 and 50 stations. One can see that the shapes of the radial components are similar to those for *x/d* > 60, but the normalized values are much smaller. The dissipation scale should be resolved for *x/d* > 40 (and well resolved at 60) and so it seems unlikely that inadequate resolution is the cause of the difference. Instead, the difference in the distributions may result from a difference in the nature of the gradient fluctuations.

4.5.3 PDF of thermal dissipation

PDFs of the normalized thermal dissipation rate, which were computed from measurements made along the jet centerline and at three axial stations, are shown in Figure 4.24. The PDFs were computed by using the radial term only, and the radial and axial terms. PDFs of the 2-D scalar (Namazian et al. 1988) and thermal (Everst et al. 1995) dissipation have been shown to be approximately log-normal, and some experimental data have shown that the 1-D dissipation PDFs are also log-normal (Boyer and Queiroz, 1991 and Effelsberg and Peters, 1988). It is seen from Fig. 4.24(a) that the PDFs that use the radial term only do not exhibit a log-normal distribution, which would appear as an inverted parabola on a log-log plot. This observation is consistent for all three axial stations. The high dissipation values are apparently log-normally distributed but not the low dissipation values. However, when the axial component is included, the PDFs approach the lognormal distribution. These observations are consistent with previous measurements of scalar dissipation in nonreacting jets (Dowling, 1991) and mixture fraction dissipation in jet flames (Karpetis and Barlow, 2002). In nonreacting flows the 1-D dissipation (Dowling, 1991) exhibits a slope of 1/2 in the low-dissipation portion of the PDF when plotted in log-log coordinates, which is similar to what is seen in Fig. 4.24(a).

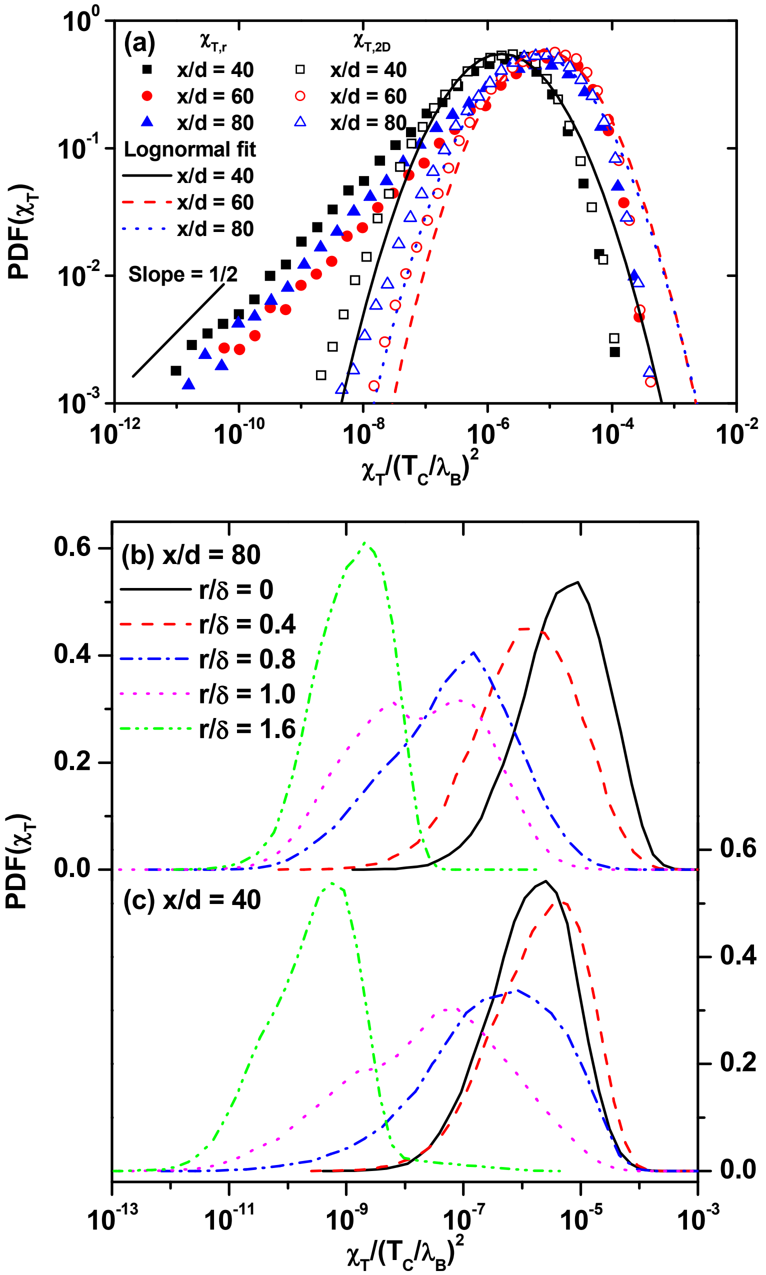

Figure 4.24 Probability density functions of thermal dissipation. (a) log-log plot showing effect of using radial and axial components to compute dissipation, (b) variation with radial location at *x/d* = 80, (c) variation with radial location at *x/d* = 40.

The power law dependence of the low-dissipation portion of the PDF is a direct result of the 1-D gradient overestimating the total gradient vector magnitude (Dowling, 1991). It is interesting that including the axial gradient term improves the log-normality of the PDF as well as it does, considering that the axial term is not fully resolved at the upstream stations. It is likely that the low-dissipation end of the distribution is in fact better resolved because the associated low-dissipation structures are much larger than the Batchelor scale. Figure 4.24(b) shows a linear-log plot of the PDFs of thermal dissipation computed from the two-component data at several radial locations at $x/d = 80$. This figure shows that the PDFs exhibit essentially log-normal behavior on centerline and near the outside edge of the jet, but not at intermediate locations. For example, at $r/\delta = 1.0$, the profile is almost bimodal, suggesting that the dissipation is either high or low at that location. The PDF at $r/\delta = 1.0$ at the $x/d = 40$ station is similarly not log-normal and the shape suggests a "double-hump" structure. The bimodal structure results from the intermittent edge of the jet, which alternatively brings turbulent fluid or co-flow air into the probe volume.

4.5.4 Joint PDF of temperature and thermal dissipation

The JPDFs of the temperature and the radial thermal dissipation rate at the jet flame centerline are shown in Fig. 4.25. The contours are scaled with the same contour levels from downstream locations x/d = 40 to 80 instead of scaled independently using different contour levels. The vertical axis represents temperature ranging from 200 to 2400 K and the horizontal axis represents the log mean radial thermal dissipation rate ranging from 2 to 10.

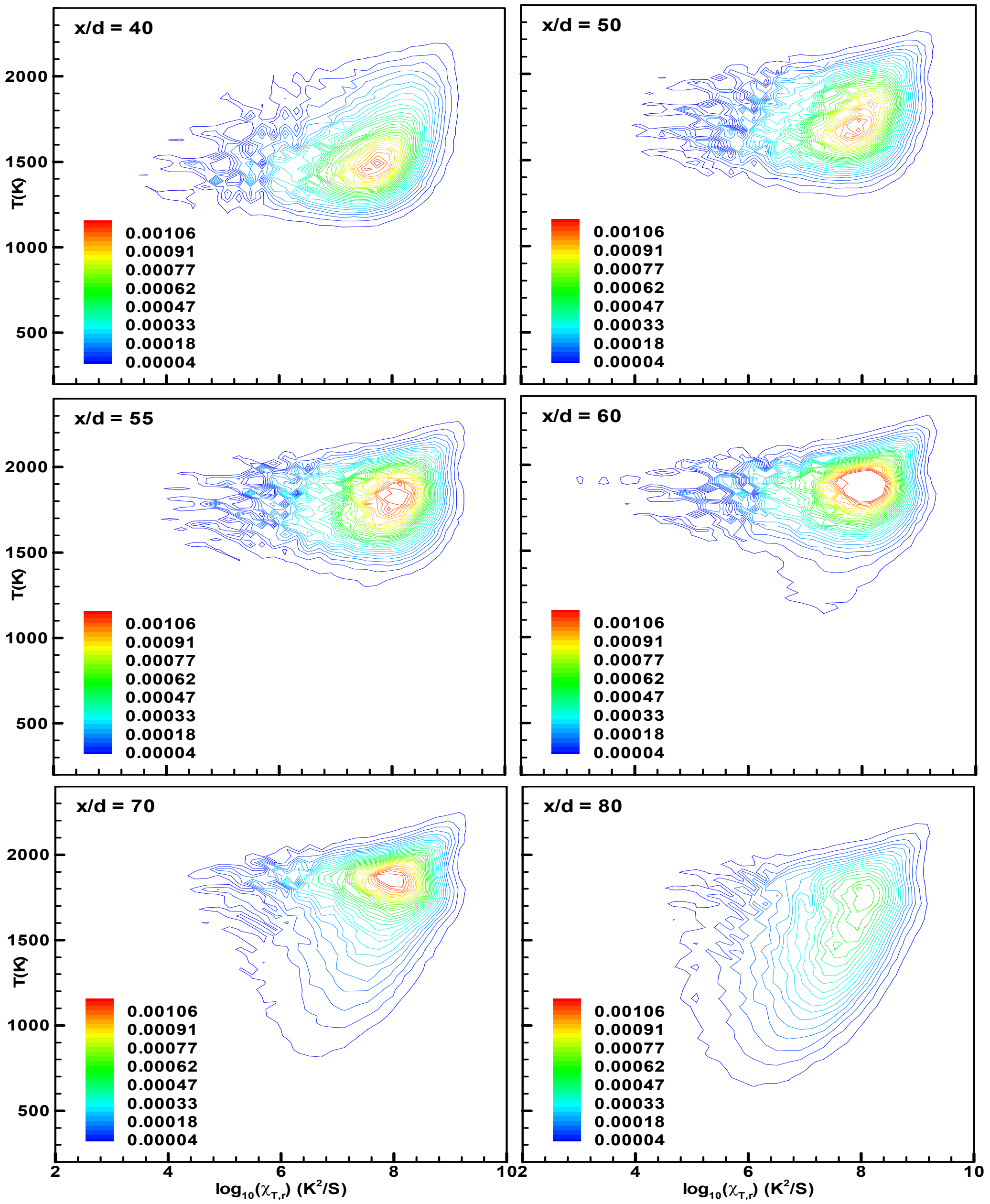

Figure 4.25 Joint PDF of temperature and radial thermal dissipation rate at the jet flame centerline

It can be seen from Fig. 4.25 that these JPDFs exhibit a similar shape from *x/d* = 40 to 60, i.e. from fuel rich region to the stoichiometric flame length. After passing the stoichiometric flame length, the JPDF shifts towards lower temperature and thermal dissipation due to jet growth and mixing with cold coflow air. The JPDF contours at the high thermal dissipation end from *x/d* = 40 to 60 generally lie vertically, which suggests a low correlation between the temperature and the radial thermal dissipation rate. The outer contour lines at *x/d* = 70 and 80 imply an increase in the correlation as they are no longer vertical.

These centerline JPDFs are different from the 2-D imaging measurement by Everest et al. (1995). They showed that the JPDF between temperature and the 2-D planar thermal dissipation rate along the centerline is nearly lognormal. As discussed in Section 4.5.3, the 1-D thermal dissipation deviates from lognormality at the low thermal dissipation end of the distribution. Therefore, the shape of the JPDF at the low thermal dissipation end is probably primarily due to 1-D effects. The noisy shape at this end is due to the apparent dissipation resulting from noise.

The shape of the these JPDFs at the high dissipation end exhibit similarities with the JPDFs measured by a two-wire probe by Boyer and Queiroz (1991) in a lifted turbulent non-premixed propane jet flame. Their JPDFs are much smoother at the low dissipation end and are closer to the lognormal distribution. The difference could be a resolution effect since their spatial resolution significantly under-resolved the Batchelor scale (20 to 60 times the Batchelor scale.

4.5.5 Correction for the apparent dissipation

The correction techniques for the apparent dissipation were discussed and the estimation procedure was derived in Chapter 3. In the two-point redundant technique, the mean-squared gradient term was measured at a fixed spatial location, i.e. on the centerline at $x/d = 40$. If the correction technique is correct then it should give the same corrected value regardless of the signal-to-noise ratio. To test this, measurements were made at different laser energies, keeping everything else the same. Varying the laser energy changes the relative contribution of the apparent dissipation rate to the measured mean thermal dissipation rate (i.e., lower laser energy should result in higher apparent dissipation rate).

Fig. 4.26 shows the effects of varying the laser energy on the measured mean-squared gradient term at the centerline and $x/d = 40$. Three laser energies were used: 5 mJ, 7.2 mJ and 12 mJ per pulse. The apparent mean-squared gradient is significantly larger than the corrected mean-squared gradient at all laser energy levels. This contribution is smaller at high laser energy (12 mJ/pulse) than at low laser energy (5 mJ/pulse). Importantly, at the smallest laser energy of 5 mJ/pulse, nearly all measured mean-squared gradient is due to noise. After subtracting the apparent mean-squared gradient from the measured mean-squared gradient term, the corrected gradients are nearly the same. These results suggest that the two-point redundant technique may provide an effective strategy for correcting for the error in the mean dissipation due to noise. Similar strategies were used by Barlow and Geyer (2004) in a laminar flame to determine the apparent noise levels for the 1-D line Raman scattering technique.

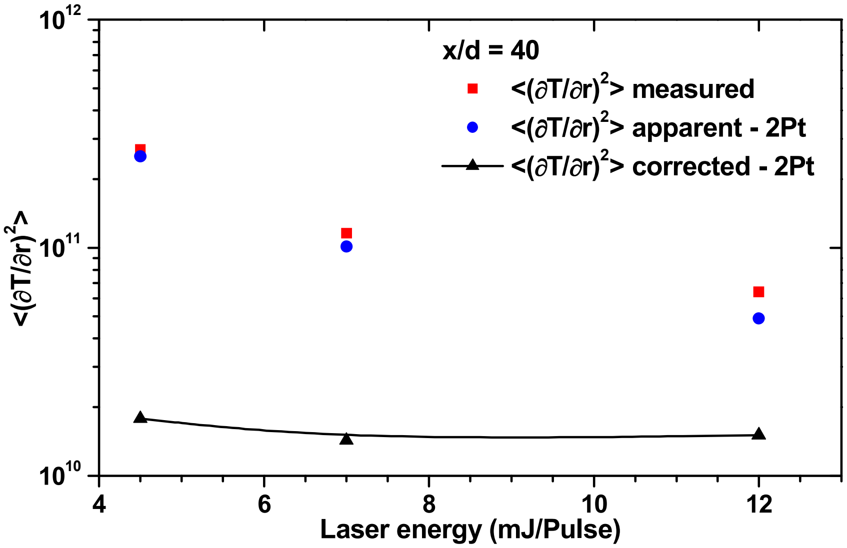

Figure 4.26 Effects of varying laser energy on the measured mean-squared gradient

Figure 4.27 shows the apparent mean-squared gradient along the jet flame centerline calculated from both the power spectra and two-point redundant techniques. As discussed in Chapter 3, the noise floor must be resolved in the power spectra technique; however, in the current study this is only true for downstream locations with *x/d* > 55. Therefore, the apparent mean-squared gradient was calculated using the PSD technique only for *x/d* > 55 as shown in Fig. 4.27. The apparent mean-squared gradient calculated from these two techniques shows nearly the same trend along the jet flame centerline. The corrected mean-squared gradients have similar values along the jet flame centerline also.

Figure 4.27 is important because it shows that the dominant contribution to the measured dissipation is noise. The apparent mean-squared gradient from both techniques is seen to represent the major contribution to the total measured mean-squared gradient. It should also be noted that the measured mean-squared gradient is always higher than corresponding apparent mean-squared gradient from the two-point redundant technique, which shows that the measured mean-squared gradient is always systematically higher than the noise, as expected. It should be noted that the corrected profiles shown in Fig. 4.27 supersede the uncorrected thermal dissipation data that are shown in Wang et al. (2004). At the time that paper was written the dominating effect of noise on the accuracy of thermal dissipation measurements was not known.

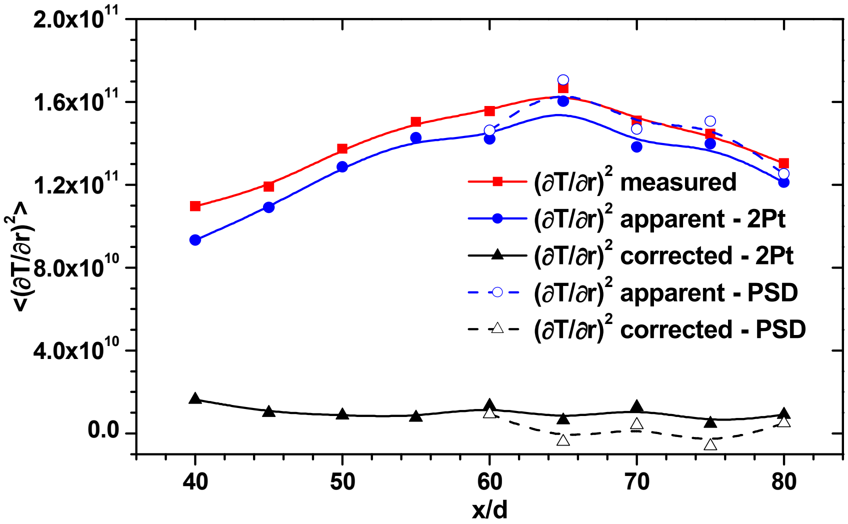

Figure 4.27 Variation of the measured mean-squared gradient, apparent mean-squared gradient by two-point redundant technique, apparent mean-squared gradient by power spectra technique and corrected mean-squared gradient (radial component only) along the jet flame centerline.

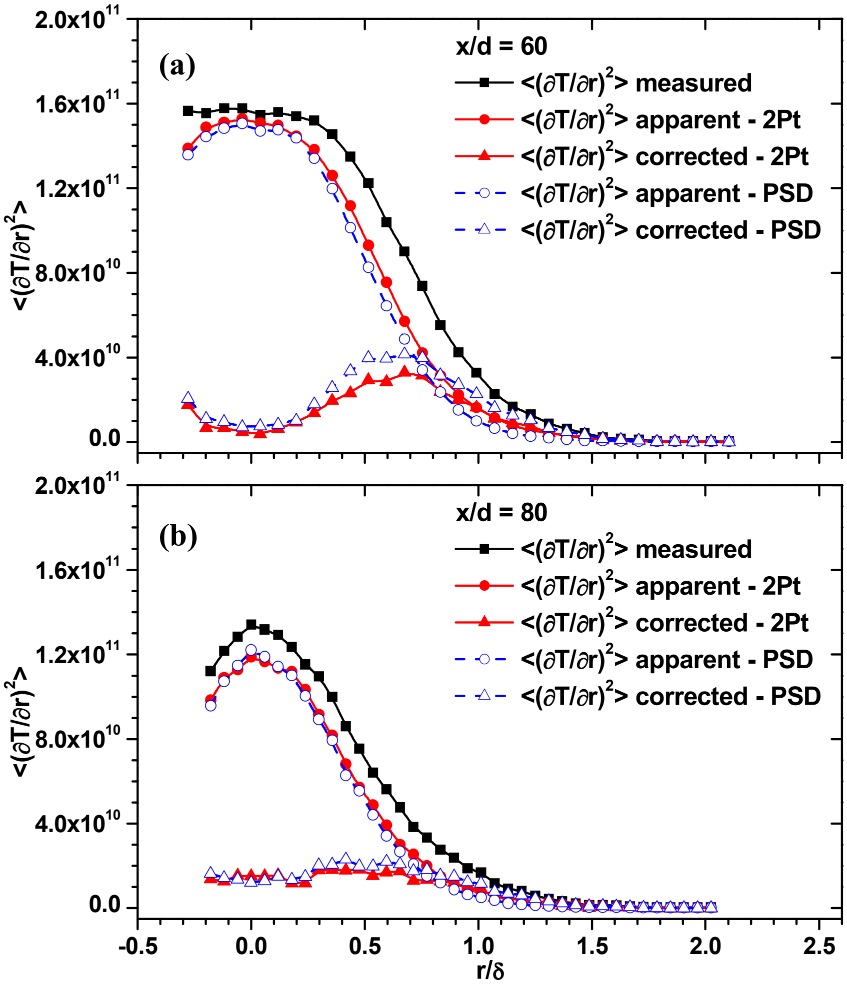

Figure 4.28 Variation of the measured mean squared gradient, apparent mean-squared gradient by two-point redundant technique, apparent mean-squared gradient by power spectra technique and corrected mean-squared gradient (radial component only) at (a) *x/d* = 60 and (b) *x/d* = 80

The radial profiles for measured, apparent and corrected mean-squared gradients by using both the two-point redundant and PSD techniques at downstream locations *x/d* = 60 and 80 are shown in Fig. 4.28. Here, the sampling frequency is high enough to resolve the noise floor at these two downstream locations and therefore the apparent mean-squared gradient from both techniques can be compared. Figure 4.28 (a) shows the results for *x/d* = 60 and Fig. 4.28(b) shows those for *x/d* = 80. At these two downstream locations, the apparent mean-squared gradients measured using both techniques agree well. Again, the apparent mean-squared gradient has a significant contribution near the jet centerline and relatively small effects at the edge of the jet flame.

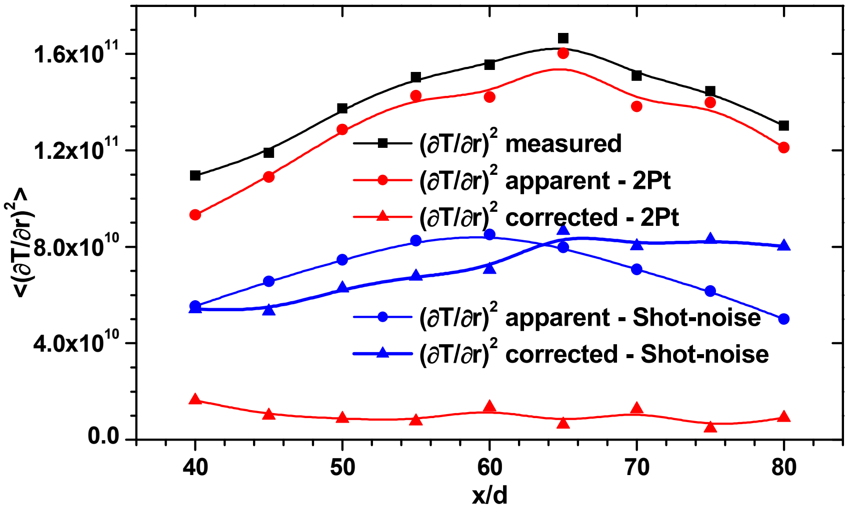

Figure 4.29 Comparing the estimated apparent mean-squared gradient from shot-noise limited noise assumptions with measured ones from the two-point redundant technique along the jet flame centerline.

At the coflow air side, the true mean-squared gradient should vanish because no gradients exist there. However, this is not the case in Fig. 4.28. This apparent dissipation was called the *shot-noise offset* by Ferrao et al. (2000). In their 1-D line Rayleigh imaging measurements in the non-reacting CO_2-air jets, they assumed that this *shot-noise offset* is constant across the whole radial profile and can be subtracted at all radial positions as well; however, this is clearly not the case. First, the apparent mean-squared gradient is not constant across the whole radial profile. Second, the apparent mean-squared gradient at the jet flame centerline due to noise effects is significantly higher than at any other radial position. Importantly, these results were obtained using independent techniques. To provide additional validation that the measured and inferred apparent mean-squared gradients are correct, the estimation procedure to calculate the apparent mean-squared gradient due to the ideal shot-noise limited noise was developed in Chapter 3.

The shot-noise limited case represents the best case, i.e., the apparent mean-squared gradient will be the lowest attainable in a real experiment. Therefore, the apparent mean-squared gradients from both the power spectra and two-point redundant techniques should be equal or greater than this shot-noise limited value and this can be used as an additional check of the apparent mean-squared gradients.

Figure 4.29 compares the variation of measured, apparent and corrected mean squared gradient assuming shot-noise limited measurements and from two-point redundant measurement and PSD technique along the jet flame centerline. It can be seen clearly that for the ideal shot-noise limited case, the estimated apparent mean-squared gradients are about 50% of the corresponding measured ones. This indicates that the measurements are not shot-noise limited, probably because of the low signals associated with the low-density region of the jet flame.

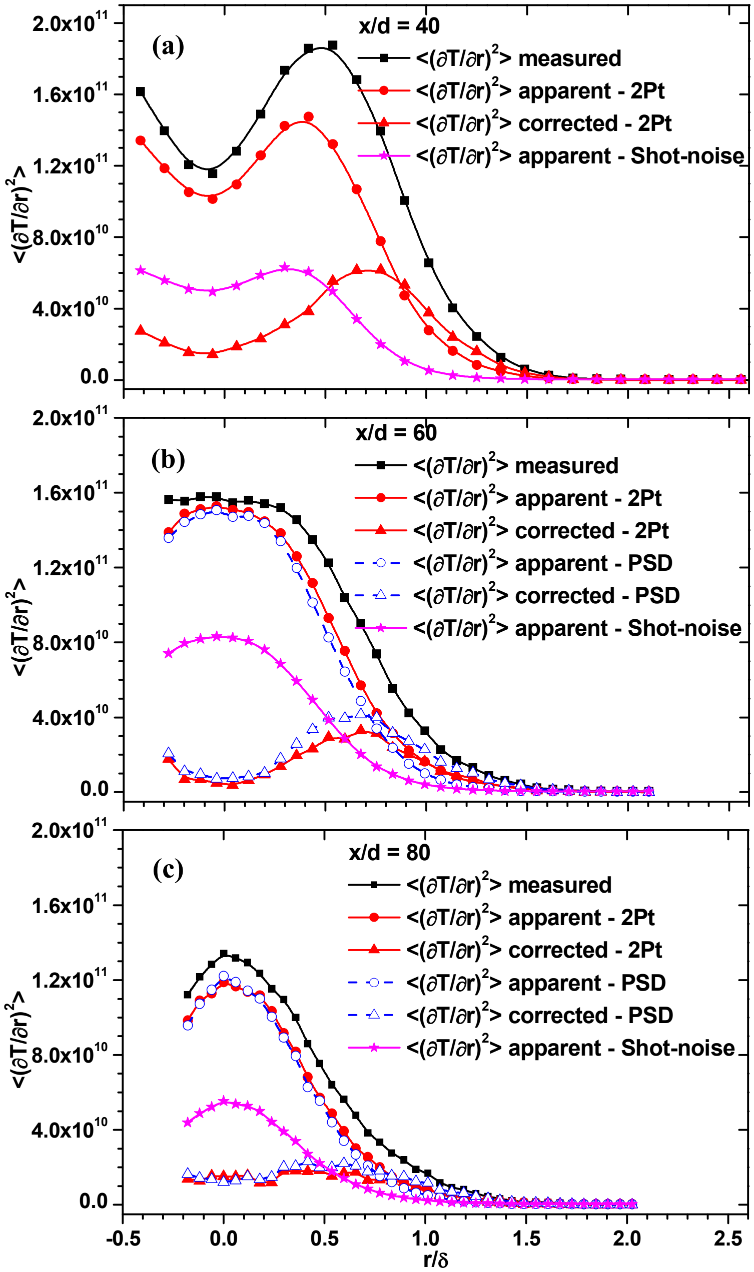

Figure 4.30 Comparing radial profiles of estimated apparent mean-squared gradient from shot-noise limited noise assumptions with measured ones from the two-point redundant technique and power spectra technique at (a) *x/d* = 40, (b) *x/d* = 60 and (b) *x/d* = 80

As discussed in Chapter 3, the estimated apparent mean-squared gradients scales as $(T/T_{air})^3$ in the shot-noise limited case. This can be a significant effect in turbulent jet flames. For example, if the local mean temperature in the centerline is 1800 K, this scaling factor will be $(1800/300)^3 = 216$. The SNR of the Rayleigh scattering signal is about 65 in the coflow air, which implies that a very small offset in the measured mean-squared gradient in air will be significantly larger on centerline.

Figure 4.30 compares the radial profiles of the apparent mean-squared gradient based on the shot-noise limited assumption with those from the two-point redundant measurement and PSD technique. The apparent mean-squared gradient profile for the shot-noise limited case was computed by using the scaling $(T/T_{air})^3$, as shown in Fig. 4.30(a), (b) and (c). Similar to axial profiles in Fig. 4.29, the shot-noise limited apparent mean-squared gradient profiles are about 50% of the corresponding measured ones over the entire profiles. Note that the apparent mean-squared gradients from both the two-point redundant and PSD technique are in good agreement over all radial positions.

Figure 4.31 compares radial profiles of the measured mean-squared gradients with corresponding corrected ones at x/d = 40, 60 and 80. It can be clearly seen that the corrected mean-squared gradients follow different trends than the uncorrected ones, especially at x/d = 60. The measured mean-squared gradient profile at x/d = 60 shows a peak on the centerline whereas the corrected radial profiles show a peak off-centerline at $r/\delta = 0.7$ where the corrected radial profile at x/d = 40 also has a peak. The peak in the radial profile of the uncorrected mean-squared gradient at *x/d* = 40 shifts from *r/δ* = 0.5 to 0.7 after correcting for noise effects and the peak value is approximately five times the centerline value. At *x/d* = 60, the off-centerline peak mean squared gradient is approximately six times the centerline value. At *x/d* = 80, the mean-squared gradient only exhibits a weak peak off-centerline. It should be also noticed that the radial locations of these peaks off-centerline are nearly the same when they are normalized by the width (FWHM) of the velocity profile.

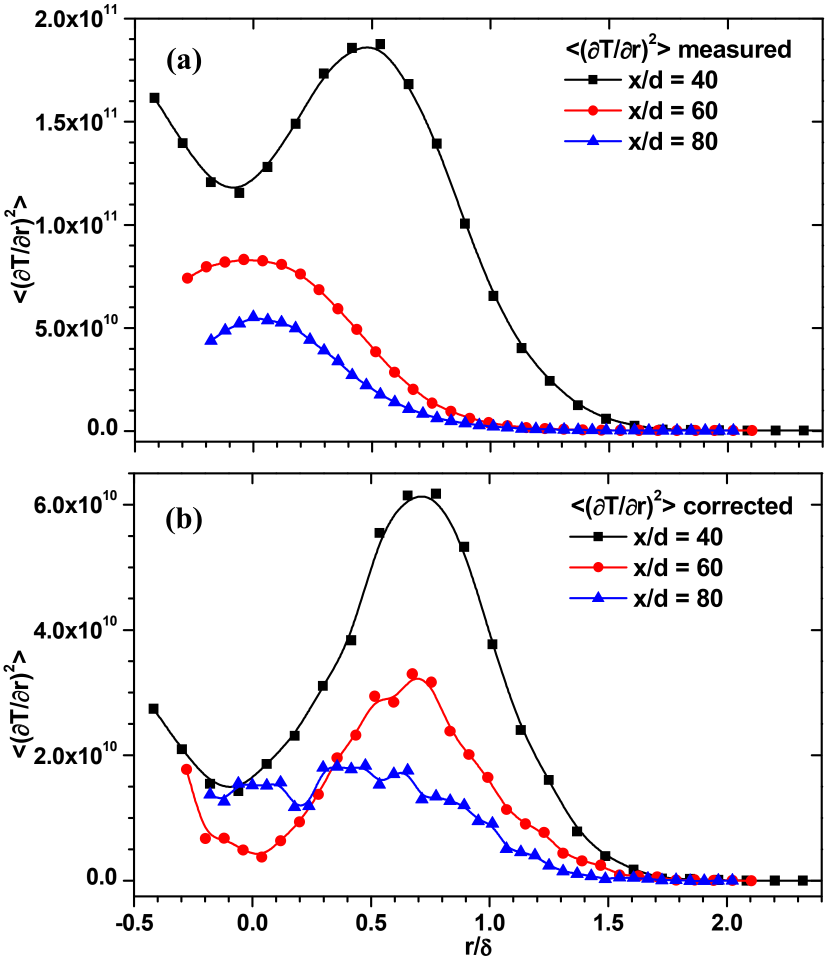

Figure 4.31 Comparing radial profiles of (a) measured (uncorrected) mean-squared gradient; (b) corrected mean-squared gradient at *x/d* = 40, 60 and 80

The off-centerline maximum was also shown by Everest et al. (1995) and they found the peak mean dissipation to be approximately five times the centerline value. Also, radial profiles of dissipation that are similar to the current $x/d = 40$ case were obtained with dual-thermocouples in the near field of a lifted propane flame (Boyer and Queriroz, 1991). They showed that the peak values were about a factor of 2-3 larger than the centerline values. The reason for these differences is probably because their measurements were made at different axial locations (relative to the flame length) than in the current study. Furthermore, their results should be viewed with some caution because the measurements either significantly under-resolved the Batchelor scale (Boyer and Queriroz, 1991) or did not carefully consider the noise effects (Everest et al., 1995). As discussed in Chapter 3, without correcting for these effects, their data could suffer from significant errors in the dissipation.

Note that measurements made in non-reacting jets have shown somewhat contradictory trends for the radial distribution of the mean scalar dissipation. For example, models suggest that the mean scalar dissipation should peak off-centerline near the region of maximum shear and hence maximum turbulence intensity. Indeed, the measurements of Lockwood and Moneib (1980), taken at a single axial station, validated this. However, other measurements (Namazian et al., 1988; Dibble et al., 1984; Antonia and Mi, 1993) show the *far-field* mean dissipation reaching a maximum on the centerline, similar to the uncorrected thermal dissipation profiles in Fig. 4.31. Once again, it should be noted that most of these studies did not consider correcting the apparent dissipation due to noise effects but rather relied on the SNR calculated for cold air.

Because the off-centerline peaks in the thermal dissipation are present at all axial locations, this suggests that they are related to the presence of the maximum shear, or more properly, the region of maximum temperature fluctuations. In the flame, however, the reaction zone is a source of thermal energy, and it may influence the distribution of the mean-square gradient. This issue is worth looking at in more detail. According to Everest et al. (1995), the thermal dissipation differs from the scalar dissipation (based on mixture fraction fluctuations) only by the factor $(dT/d\xi)^2$. The relationship between T and ξ for this flame is known from TNF workshop database, and it is similar to a piecewise linear function that peaks near the stoichiometric mixture fraction and is zero at $\xi = 0$ and 1. This means that on each side of the stoichiometric mixture fraction, $dT/d\xi$ is approximately constant, and hence the thermal dissipation should be proportional to the mixture fraction dissipation. Near stoichiometric, $dT/d\xi$ should decrease, and so the thermal dissipation should be smaller than the mixture fraction dissipation. This argument suggests that if the underlying mean scalar dissipation peaked on centerline, and decreased with increasing radius, then the thermal dissipation would not exhibit a local maximum off-centerline, but in fact would exhibit a local minimum at the reaction zone. Since this is not the behavior we see, it suggests that the underlying scalar dissipation indeed exhibits an off-centerline peak.

The discussion of dissipation profiles in connection with Fig. 4.31 assumes that the dissipation can be computed from the radial gradient alone. Off-centerline laminarization by the reaction zone may render this the dominant component of the dissipation, in contrast to the centerline where the gradients are likely to be more isotropic. It is therefore possible that the total dissipation may peak at the centerline, even though the radial dissipation does not. This would be true for the upstream locations where the reaction zone is well off the centerline, but not for locations past the stoichiometric flame tip, such as at *x/d* = 80.

Figure 4.32 shows profiles of the measured and corrected mean-squared gradients at three axial stations that have been scaled by $\left(T_{rms}/\lambda_B\right)^2$. The figure shows that without correction for the apparent mean-squared gradient, the normalized radial profiles do not show any similarities, in either magnitude or shape, at the different downstream locations. At *x/d* = 60, the normalized peak mean-squared gradient is on the centerline, whereas the peak is off-centerline at *x/d* = 40. However, the normalized corrected profiles are in good agreement and are all relatively flat. These results indicate that the corrected profiles follow the scaling of $\left(T_{rms}/\lambda_B\right)^2$. As discussed in section 4.3, the local Reynolds number is close to a constant and so the ratio between the Batchelor scale and all other scales, including the Taylor scale, is also a constant. Therefore, the profiles normalized by $\left(T_{rms}/\lambda_B\right)^2$ will have the same trend as those scaled by $\left(T_{rms}/\lambda_T\right)^2$, where λ_T is the Taylor micro-scale. This provides further support that the mean-squared gradient profiles have been accurately corrected.

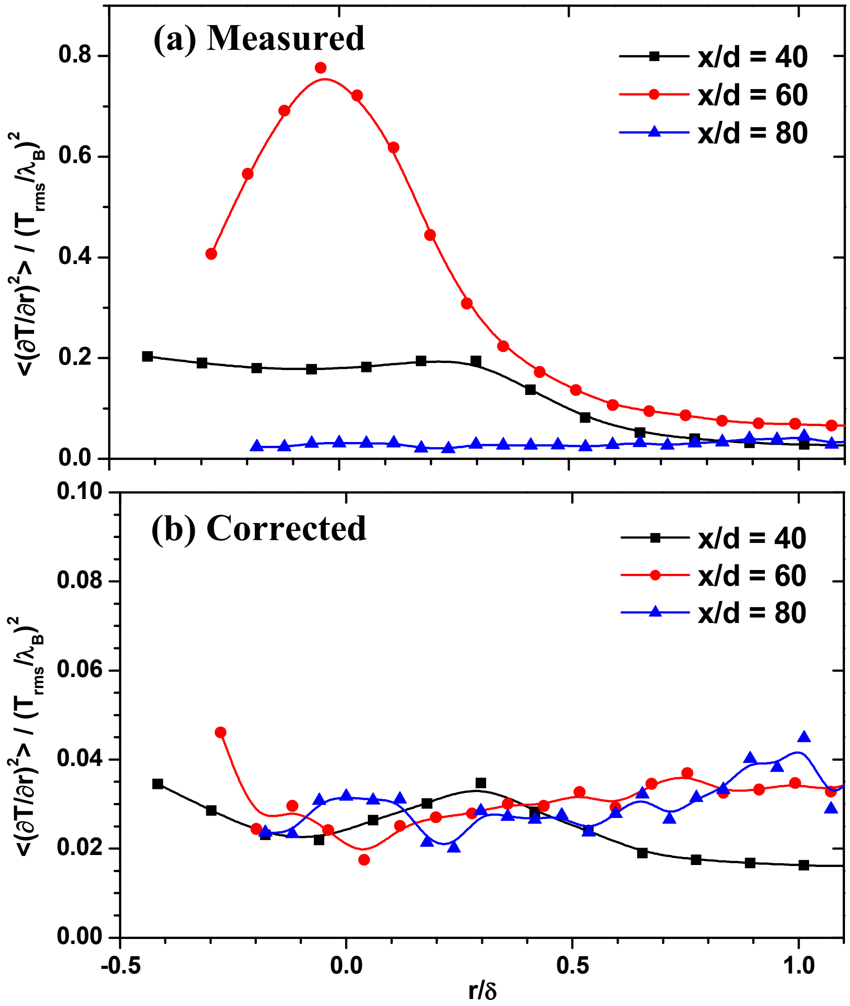

Figure 4.32 Radial profiles of the (a) measured, (b) corrected mean-squared gradient terms normalized by the $\left(T_{rms}/\lambda_B\right)^2$ at *x/d* = 40, 60 and 80

4.5.6 Effects of the thermal diffusivity

In the discussion above, the mean-squared gradient term, $\overline{\left(\partial T/\partial r\right)^2}$ or $\left\langle\left(\partial T/\partial r\right)^2\right\rangle$, was used instead of the thermal dissipation rate, $\overline{2\alpha\left(\partial T/\partial r\right)^2}$ or $\left\langle 2\alpha\left(\partial T/\partial r\right)^2\right\rangle$. The reason for this was to isolate effects of mean-squared gradient and thermal diffusivity. In non-reacting flows, the diffusivity is generally a constant and scalar dissipation rate will follow the same trends as the mean-squared gradient. However, in turbulent flames, the thermal and mass diffusivities scale as $\left(T/T_{air}\right)^{1.74}$, which shows a significant temperature dependence. Recent results comparing the LES data to the 1-D Raman experimental data by Geyer et al. (2004) showed that the mass diffusivity may sometimes outweigh the mean-squared gradient terms in the mean measured mixture fraction dissipation.

Fig. 4.33 shows a comparison of measured mean radial thermal dissipation calculated in two different ways: using the mean thermal diffusivity $\langle 2\alpha \rangle \left\langle \left(\partial T/\partial r\right)^2 \right\rangle$, and using the instantaneous thermal diffusivity $\left\langle 2\alpha \left(\partial T/\partial r\right)^2 \right\rangle$. When using the instantaneous thermal diffusivity, there are additional terms originating from the cross-correlation between the thermal diffusivity and the mean-squared gradient terms that will result in a higher measured thermal dissipation rate than dissipation rate calculated using the mean thermal diffusivity. This is illustrated in Fig. 4.33, where the radial mean thermal dissipation rate calculated using instantaneous thermal diffusivity is always higher than that using the mean thermal diffusivity. However, the corrected mean thermal dissipation from these two methods is nearly the same.

Theoretical analysis shows that even without noise, the mean thermal dissipation rate calculated using the instantaneous thermal diffusivity will be higher than that using the mean thermal diffusivity due to the cross-correlation between the fluctuating temperature and the mean-squared gradient term. This theoretical prediction is not confirmed by the data in Fig. 4.33 because the mean square temperature fluctuations and noise fluctuations are relatively small comparing to the mean squared temperature. For example, assuming all cross-correlation terms are negligible, the corrected mean thermal dissipation can be approximated by

$$\bar{\chi} \propto \left(\bar{T}^2 + \overline{T'^2} + \sigma_n^2\right)\overline{(\partial T/\partial r)^2}\ . \tag{4.23}$$

Generally, the mean temperature is much larger than the other two terms. For example, at *x/d* = 60, $\left(\overline{T'^2}/\bar{T}^2\right) = (203/1819)^2 = 1.2\%$. This is why there is essentially no difference between the corrected mean thermal dissipation rates computed from the mean and instantaneous thermal diffusivities.

As discussed in Chapter 3, if the thermal diffusivity effects are included, then the apparent thermal dissipation from a shot-noise limited measurement will scale as $(T/T_{air})^{4.74}$. This indicates that temperature has an even larger impact on thermal dissipation measurement than the mean-squared gradient.

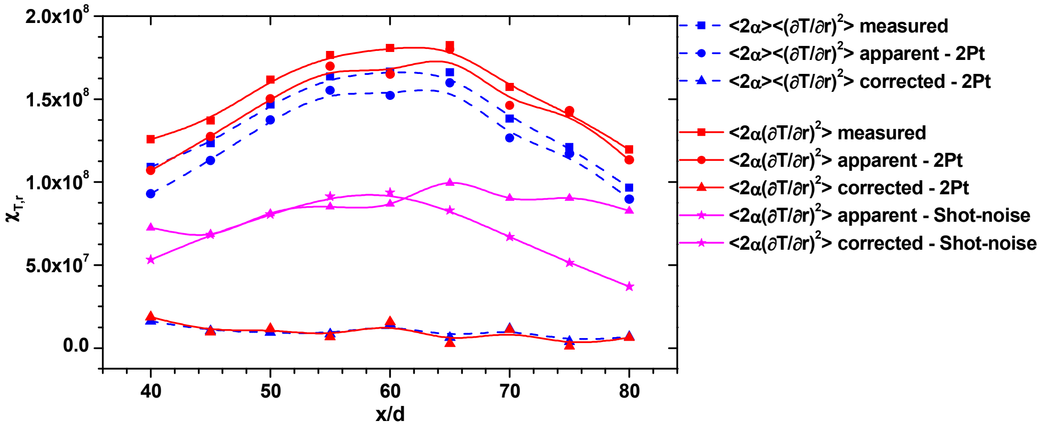

Figure 4.33 Effects of the thermal diffusivity on the measured radial mean scalar dissipation rate

The variation of the corrected centerline mean thermal dissipation is shown in Fig. 4.33 as well. The corrected mean thermal dissipation is seen to be nearly the same from *x/d* = 40 to 80 in the current study. In the paper of Peters and Williams (1983), it is argued that in nonreacting round jets the mean scalar dissipation rate should scale as $\overline{\chi} \propto \left(\overline{\xi}/\lambda_B\right)^2$, where $\overline{\xi}$ is the mean mixture fraction and $\overline{\xi} \propto x$ in round jets and $\lambda_B \propto \delta\, Re_\delta^{-3/4} \propto x$ (since $\delta \propto x$ and Re_δ is constant), then we have $\overline{\chi} \propto x^{-4}$. Although the measurements are not all consistent, the highly resolved dissipation data of Dowling and Dimotakis (1990) seem to validate this scaling law in nonreacting jets.

The corrected thermal dissipation results shown in Fig. 4.33 indicate that the dissipation is approximately constant with downstream distance, and so it clearly does not follow the same scaling as the mixture fraction. This means that either the underlying scalar dissipation decay is different in jet flames or the thermal dissipation does not reflect the underlying scalar dissipation. Once again, however, since we are using only the radial component to compute the dissipation (because it is resolved over a wider range), we cannot rule out the possibility that non-isotropy of the dissipation scales could account for the trend seen in Fig. 4.33. This seems unlikely however, because any laminarization that would occur near the stoichiometric flame tip should favor the axial temperature gradient and thus reduce the dissipation based only on the radial-gradient.

One thing to note is that from the jet exit to a location somewhat upstream of the stoichiometric flame length (near *x/d* = 60), the factor $dT/d\xi$ should be approximately constant, and so the thermal dissipation should exhibit the $\left(x/d\right)^{-4}$

scaling if the scalar dissipation does. We can explore this further by considering the scaling of the thermal dissipation. As above, it can be argued that the thermal dissipation rate along the jet flame centerline will scale as $\overline{\chi_T} \propto \alpha\left(\overline{T_{rms}}/\lambda_B\right)^2$. Table 4.1 shows that the local Reynolds number is approximately constant from $x/d = 40$ to 60, and so the Batchelor scale should scale the same as in a nonreacting jet, i.e., $\lambda_B \propto \delta\, Re_\delta^{-3/4} \propto x$. If we make the approximation that $\overline{T_{rms}}$ is approximately constant (which is really only true for locations upstream of the point of maximum temperature), and we make the further approximation that $\alpha \propto \left(\overline{T_C}\right)^{1.8} \propto x^{1.8}$, then we find $\overline{\chi_T} \propto \alpha\left(\overline{T_{rms}}/\lambda_B\right)^2 \propto x^{-0.2}$. The current corrected data are approximately consistent with this weak dependence of the dissipation on x. It is important to note that the uncorrected thermal dissipation data exhibit a linear increase with downstream distance, which is difficult to justify based on known scaling laws.

4.6 SUMMARY

The newly developed high-repetition rate (10 kHz) laser Rayleigh scattering facility was used to study the temperature fluctuations, power spectra, gradients and thermal dissipation rate characteristics of a nonpremixed turbulent jet flame at a Reynolds number of 15,200. The flame studied here is similar to the TNF simple jet flame DLR_A. The radial temperature gradients are measured by a two-point technique, whereas the axial gradient is measured from the temperature time-series combined with Taylor's hypothesis.

Axial mean and *rms* temperature profiles along the centerline from downstream distances *x/d* = 40 to 80, radial mean and *rms* temperature profiles at

$x/d = 40$, 60 and 80 were compared with both the SANDIA and DLR datasets and showed good agreement.

Spatial/temporal resolution and noise issues were carefully considered in this study. The Batchelor scale was first estimated by using the scaling laws developed for non-reacting turbulent jet flows, but with a local Reynolds number that was reduced in magnitude owing to heat release. The second method of calculating Batchelor scale was based on the “turbulence Reynolds number”. In this case the integral length scale was inferred from the integral time scale computed from the auto-correlation function of the fluctuating temperature. These two methods showed good agreement in the estimated/calculated Batchelor scale. This suggests that the proposed estimation method does work for Batchelor scale estimation under flame conditions.

It was found that the ratio of the integral length scale, l, to the outer length scale, δ, is close to that measured in non-reacting jets ($l/\delta = 0.226$). This agreement suggests that the temperature fluctuation, gradient and spectra do reflect the underlying turbulence under flame conditions.

The temperature power spectra along the jet centerline exhibit only a small inertial subrange due to the low local Reynolds number ($Re_\delta = 2{,}500$), although a larger inertial subrange is present in the spectra at off-centerline locations. Scaling the frequency by the estimated Batchelor scale improves the collapse of the dissipation region of the spectra, which also implies that the estimated Batchelor scale is correct.

The resulting two-point time-series measurements in a turbulent flame show that the probability density functions (PDF) of the thermal dissipation are shown to deviate from lognormal in the low dissipation portion of the distribution when only one component of the gradient is used. In contrast, nearly lognormal distributions are obtained along the centerline when both axial and radial components are included.

The apparent mean-squared gradient due to noise was estimated by the power-spectra and two-point redundant techniques. For the apparent and corrected mean-squared gradients, axial profiles along the centerline, and radial profiles at *x/d* = 60 and 80 showed good agreement by both correction techniques. Both techniques showed that for the conditions studied, noise tends to dominate the measured thermal dissipation.

To further assure the validity of these two correction techniques, the apparent dissipation rate was also estimated by the procedure proposed in Chapter 3 for the ideal shot-noise limited case. The apparent dissipation estimated will be the best (minimum) that could be attained in an actual experiment. Even for this ideal case, the estimated apparent dissipation rate is still about 50% of the measured mean scalar dissipation rate, which supports that validity of the PSD and two-point correction techniques.

The corrected radial thermal dissipation profiles were found to be approximately constant when normalized by $\left(T_{rms}/\lambda_B\right)^2$. This is in contrast to the uncorrected profiles that did not scale as $\left(T_{rms}/\lambda_B\right)^2$, especially at *x/d* = 60. Classical turbulence theory shows that the mean scalar dissipation rate should scale as $\left(T_{rms}/\lambda_T\right)^2$, and since $\lambda_T \propto \lambda_B$ (since Re_δ is constant), then it is only the corrected profiles that follow the expected scaling.

These results show that reporting mean thermal dissipation data without correcting for the apparent dissipation due to noise effects, can lead to incorrect magnitudes of dissipation as well as incorrect trends. When comparing scalar dissipation rate from numerical simulations with experimental data, close attention should be paid to how noise affects the measured values.

Chapter 5 Conclusions

5.1 DEVELOPMENT OF THE HIGH REPETITION RATE LASER RAYLEIGH SYSTEM

One of the major objectives of this work was to develop a high-repetition rate laser diagnostics system for point measurements of temperature in turbulent flames. The system included a diode-pumped Nd:YAG laser, multiple photomultiplier tubes with a multi-channel high voltage power supply system, multi-channel data acquisition system, and a custom-designed low f-number optical collection system. Furthermore, a new particle-free co-flowing jet flame facility was developed, which consisted of a concentric jet surrounded by a co-flow, a two-dimensional linear translation system and the fuel supply and metering system. A LabVIEW program was developed to control and synchronize the whole experiment. This unique facility was used to make two-point time-resolved measurements of the temperature fluctuations in a turbulent nonpremixed jet flame.

5.2 SCALAR DISSIPATION MEASUREMENT MODEL

A major goal of this work was to make high quality measurements of the temperature fluctuations and thermal dissipation. Thermal dissipation measurements are very challenging because they require that resolution and noise effects be carefully considered. Toward this end, a model was developed that considered several submodels related to the measurement, post-processing and calculation of the dissipation.

The measurement sub-model focused on the resolution and noise effects in scalar dissipation experiments. The resolution was modeled as a convolution process and quantified by the Line-Spread-Function (*LSF*). The *LSF* was used instead of the Point-Spread-Function (*PSF*) because the gradient calculation by the two-point technique was essentially a 1-D technique. The noise was modeled as an additive source that induces an apparent dissipation or bias error in the measured scalar dissipation measurement. The sub-model showed that different noise levels will lead to different resolution-error curves in the measured mean scalar dissipation rate. These results are an extension to the work of Mi and Nathan (2003), who investigated the effect of probe resolution, in what is in effect the noise-free limit, on the mean scalar dissipation.

The post-processing sub-model considered the effect of post-processing filters, e.g. averaging, smoothing, low-pass filters, etc. Combining the effects of measurement and post-processing, it was found that if the noise offset in the measured scalar dissipation can be corrected, or the SNR is so high that noise is not important in the dissipation measurement, the correlated resolution and noise issue is reduced to a resolution issue only. In this case, the analysis by Mi and Nathan (2003) for the probe resolution and model for flow imaging experiments proposed by Wang and Clemens (2004) can be applied.

The gradient sub-model takes into account effects of differentiation stencils, e.g. first-order forward/backward and second-order central differencing. The first order forward/backward differencing is essentially a high-pass filter and the central difference is a band-pass filter. These stencils are very important for time-series experiments, especially when using the time-derivative and Taylor's hypothesis to infer the spatial gradients. The post-processing filter and the differentiation stencil will jointly determine the final shape of the scalar and gradient spectrum and hence the measured mean scalar dissipation rate. Therefore, to design or apply the post-processing filters, the differentiation stencil must be considered as well.

The dissipation sub-model mainly considered the effect of temperature fluctuations on the computation of the thermal diffusivity. In reacting flows, where high temperature fluctuations are present, the uncertainty in the diffusivity may be even more important than the uncertainty in the squared gradient term in the scalar dissipation expression.

A result of the model is that the difference signal-to-noise ratio (*DSNR*) is considered more important for dissipation measurements than the traditional SNR. The *DSNR* relates the *rms* temperature difference between the two probes to the *rms* noise. Since accurate dissipation measurements require that the probes be so closely spaced that the temperature difference is small, obtaining sufficiently high *DSNR* is challenging in most experiments.

Two noise correction techniques were developed to correct for the apparent dissipation in the measured mean scalar dissipation. The first technique was an extension of the *PSD* correction procedure proposed by Renfro et al. (1999, 2000). After correcting for the noise floor in the PSD, further correction procedures for the apparent dissipation were developed. The second method is the two-point redundant technique. By separating and overlapping the two sampling points, the measured and apparent dissipation can be measured directly. Subtracting the apparent dissipation rate from the measured dissipation rate will give the corrected dissipation rate. Procedures to implement these techniques were developed as well. For 1-D line-imaging experiments, a binning-pixel technique was also proposed although not implemented in this study.

For the laser Rayleigh scattering technique, the apparent dissipation (bias error) at any measurement location can be scaled by using the apparent dissipation value measured in ambient air together with the shot-noise limited assumption. This noise estimation procedure can be used to determine the minimum apparent dissipation rate that can be obtained in an actual experiment, and is useful when designing experiments that seek to measure dissipation rates.

5.3 TWO-POINT HIGH REPETITION TEMPERATURE AND THERMAL DISSIPATION MEASUREMENT IN A NON-PREMIXED TURBULENT JET FLAME

The newly developed high-repetition rate (10 kHz) laser Rayleigh scattering facility was used to study the temperature fluctuations, power spectra, gradients and thermal dissipation rate characteristics of a nonpremixed turbulent jet flame at a Reynolds number of 15,200. The flame studied here is similar to the TNF simple jet flame (DLR_A). The radial temperature gradients were measured by a two-point technique, whereas the axial gradient was measured from the temperature time-series combined with Taylor's hypothesis.

Axial mean and *rms* temperature profiles along the centerline from downstream distances *x/d* = 40 to 80, radial mean and *rms* temperature profiles at *x/d* = 40, 60 and 80 were compared with both the SANDIA and DLR datasets and showed good agreement.

One objective of this work is to identify a means of determining the Batchelor scale in turbulent nonpremixed jet flames. The Batchelor scale was first estimated by using non-reacting jet scaling laws and a local Reynolds number that reflected the enhanced kinematic viscosity owing to heat release. This estimate was compared to a second method of calculating the Batchelor scale based on the "turbulence Reynolds number", which is based on the integral length scale (inferred from the integral time scale from the autocorrelation function of the fluctuating temperature) and the *rms* velocity. The two methods showed good agreement between the estimated and calculated Batchelor scale.

The ratio of the integral length scale (l), inferred from the temperature autocorrelation function, to the outer length scale (δ) is close to that of non-reacting jets (l/δ = 0.226). This agreement suggests that the temperature fluctuations, gradients and spectra do reflect the underlying turbulence under flame conditions.

The temperature power spectra along the jet centerline exhibit only a small inertial subrange, which is probably because of the low local Reynolds number (Re_δ = 2,500) of the jet flames. However, a larger inertial subrange is present in the spectra at off-centerline locations. Scaling the frequency by the estimated Batchelor scale improves the collapse of the dissipation region of the spectra, which strongly suggests that the Batchelor scale is being properly estimated.

The resulting two-point time-resolved measurements in a turbulent flame show that the probability density functions (PDF) of the thermal dissipation are shown to deviate from lognormal in the low dissipation portion of the distribution when only one component of the gradient is used. In contrast, nearly lognormal distributions are obtained along the centerline when both axial and radial components are included.

Extensive work was conducted to determine the apparent dissipation that contaminated the mean dissipation measurements. This was accomplished by using both the power-spectra and two-point redundant techniques. For the apparent and corrected squared gradients, axial profiles along the centerline, and radial profiles at $x/d = 60$ and 80 showed good agreement by both correction techniques. These two techniques can therefore serve as a cross-check on each other, and the experiments can be considered to be self-consistent in this sense. Both techniques showed significant apparent dissipation or bias in the measured thermal dissipation rate.

To further assure the validity of these two correction techniques, the apparent dissipation rate was also estimated by the procedure proposed in Chapter 3 for the ideal shot-noise limited case. The apparent dissipation estimated represents the best (i.e., minimum) apparent dissipation possible in a real experiment. Even for this ideal case, the estimated apparent dissipation rate was quite large (about 50% of the measured mean scalar dissipation rate), which supports the large correction indicated by the power-spectra and two-point-redundant techniques. The correction procedure was further validated by scaling the corrected and uncorrected mean dissipation by the expected scaling factor of $\left(T_{rms}/\lambda_B\right)^2$. This normalization showed that the corrected mean dissipation profiles scaled as expected, whereas the uncorrected profiles did not. This result offers additional support for the validity of the correction procedure and emphasizes the importance of correcting mean dissipation data if accurate measurements are to be obtained.

At all three downstream locations *x/d* = 40, 60 and 80, the corrected radial profiles of the mean thermal dissipation exhibit a peak off the centerline, whereas the uncorrected profiles exhibit a peak on centerline. The mean dissipation is expected to scale as $(T_{rms})^2$, and since the temperature fluctuations peak off-centerline, this is further evidence that the corrected dissipation profiles are correct.

These results clearly indicate that noise has a significant effect on mean dissipation measurements, but it may be possible to correct for this effect by using the power-spectra and two-point-redundant techniques. Furthermore, it is clear from these results that accurate mean dissipation measurements are extremely difficult to make and most previous measurements of this type, in both reacting and non-reacting flows, are likely contaminated by substantial apparent dissipation.

5.4 FUTURE WORK

The current work was mainly focused on how to get accurate thermal dissipation rate measurements in a turbulent non-premixed jet flame by a careful consideration of issues like resolution, noise and the correlation between them. The techniques and results developed here suggest additional work in this facility that should be done in the future.

The analysis shows the importance of having very high SNR (actually, *DSNR*) and so the experiment should be modified to improve the signals as much as possible. First, some hardware improvements can be made for the current two-point high repetition rate laser Rayleigh scattering system. For example, a high quantum efficiency (40%) PMT (from Hamamatsu) can be used to replace the current one, which has a quantum efficiency of 16%. Furthermore, the detection channel should be divided into two separate channels and each channel given its own collection optics (rather than using the beam cube splitter). The combination of these two improvements will increase the signal by a factor of five.

Provided the *DSNR* is sufficiently high, it may be desirable to make even higher spatial resolution measurements; the slit width can be reduced to 100 μm to give a corresponding spatial resolution in the flow of 150 μm. At the same time, the laser beam diameter should also be reduced to about 150 μm. This can be achieved by expanding the beam before focusing it into the test section.

As argued previously, it may be possible to use the thermal dissipation rate as a proxy for investigating characteristics of the scalar dissipation rate, which is notoriously hard to measure. The thermal and scalar dissipation are related through a state relationship, but this relationship has not been studied in detail. For spatial locations where the fuel combination will always be on the fuel-lean or fuel-rich side, it may be possible to directly infer the scalar dissipation from the thermal dissipation. For example, at axial locations that are past the stoichiometric flame length, the mixture will be on the fuel-lean side. Owing to the small scalar dissipation there, Raman scattering techniques will have significant difficulties in measuring the dissipation accurately. Since the temperature fluctuations are potentially affected by combustion chemistry as well as the underlying turbulence, it is suggested that this work be pursued through a close collaboration with combustion modelers.

References

International Workshop on Measurement and Computation of Turbulent Nonpremixed Flames (TNF), http://www.ca.sandia.gov/TNF/

Software tools for calculation of "Transport Properties" and "Chemical Equilibrium" at http://grashof.engr.colostate.edu/tools/

Coherent Inc., "CORONA Laser User Manual", 2000.

Hamamatsu Co., "Phtomultiplier Tubes: Basics and Applications", 1994.

Antonia, R.A. and Mi, J., "Temperature dissipation in a turbulent round jet", *J. Fluid Mech*., Vol. 250, pp. 531-551, 1993.

Barlow, R.S., "Comparison of Measured and Modeled Scalar Dissipation: Progress and Challenges", 7th International Workshop on Measurement and Computation of Turbulent Nonpremixed Flames, Chicago, IL, July 22-24, 2004.

Barlow, R.S. and Karpetis, A.N., "Scalar Length Scales and Spatial Averaging Effects in Turbulent Piloted Methane/Air Jet Flames", *Proc. Comb. Inst.*, Vol. 30, to be published, 2004.

Barlow, R.S. and Karpetis, A.N., "Measurements of Scalar Dissipation", 6th International Workshop on Measurement and Computation of Turbulent Nonpremixed Flames, Sapporo, Japan, July 18-20, 2002.

Batchelor, G.K., "Small-scale variation of convected quantities like temperature in a turbulent fluid. Part 1. General discussion and the case of small conductivity", *J. Fluid Mech.*, Vol. 5, pp. 113-71, 1959.

Becker, H.A. and Yamazaki, S., "Entrainment, momentum flux and temperature in vertical free turbulent jet diffusion flames", *Combust. Flame*, Vol. 33, pp. 123-149, 1978.

Bergmann V., Meier, W., Wolff, D. and Stricker, W., "Application of spontaneous Raman and Rayleigh scattering and 2D LIF for the characterization of a turbulent CH4/H2/N2 jet diffusion flame", *Appl. Phys. B*, Vol. 66, pp. 489-502, 1998.

Bernard, P.S. and Wallace, J.M., “Turbulent Flow: Analysis, Measurement, and Prediction”, Hoboken, N.J.: Wiley, 2002.

Bilger, R.W., “The Structure of Diffusion Flames”, *Combst. Sci. and Tech.*, Vol. 13, pp. 155-170, 1976.

Bilger, R.W., “The Structure of Turbulent Nonpremixed Flames”, *Proc. Combust. Inst.*, Vol. 22, pp.475-488, 1988.

Bilger, R.W., “Future progress in turbulent combustion research”, *Prog. Energy Combust. Sci.*, Vol. 26, pp. 367-380, 2000.

Boyer, L. and Queiroz, M., “Temperature Dissipation Measurements in a Lifted Turbulent Diffusion Flame”, *Combust. Sci. and Tech.*, Vol. 79, pp. 1-34, 1991.

Bray, K.N.C., “The Challenge of Turbulent Combustion”, *Proc. Combust. Inst.*, Vol. 26, pp.1-26, 1996.

Brockhinke, A., Andresen, P. and Kohse-Hoinghaus, K., “Contribution to The Analysis of Temporal and Spatial Structures Near The Lift-Off Region of A Turbulent Hydrogen Diffusion Flame”, *Proc. Combust. Inst.*, Vol. 26, pp.153-159, 1996.

Brockhinke, A., Haufe, S. and Kohse-Hoinghaus, K., “Structural Properties of Lifted Hydrogen Jet Flames Measured by Laser Spectroscopic Techniques”, *Combust. Flame*, Vol. 121, pp.367-377, 2000.

Buch, K.A. and Dahm, W.J.A., “Experimental study of the fine-scale structure of conserved scalar mixing in turbulent shear flows, Part 1. Sc>>1”, *J. Fluid Mech.*, Vol. 317, pp. 21-71, 1996.

Buch, K.A. and Dahm, W.J.A., "Experimental study of the fine scale structure of conserved scalar mixing in turbulent shear flows, Part 2. Sc $\approx$ 1", *J. Fluid Mech.*, Vol. 364, pp. 1-29, 1998.

Caldeira-Pires, A. and Heitor, M.V., “Temperature and Related Statistics in Turbulent Jet Flames”, *Exp. Fluids*, Vol. 24, pp. 118-129, 1998

Chapman, D. R. “Computational aerodynamics development and outlook”, *AIAA J.*, Vol. 17, pp. 1293-1313, 1979.

Chen, C.J. and Rodi, W., “Vertical turbulent buoyant jets: a review of experimental data”, Oxford: Pergamon Press, 1980.

Chen, Y-C and Mansour, M., “Measurements of Scalar Dissipation in Turbulent Hydrogen Diffusion Flames and Some Implications on Combustion Modeling”, *Combust. Sci. Tech.*, Vol. 126, pp.291-313, 1997.

Clemens, N.T., “Flow Imaging”, In *Encyclopedia of Imaging Science and Technology*, John Wiley and Sons, New York, pp. 390-419, 2002.

Dahm, W.J.A. and Southerland, K.B., “Experimental assessment of Taylor’s hypothesis and its applicability to dissipation estimates in turbulent flows”, *Phys. Fluids A*, Vol. 9, No. 7, pp. 2101-2107, 1997.

Dibble, R.W. and Hollenbach, R.E., “Laser Rayleigh thermometry in turbulent flames”, *Proc. Combust. Inst.*, Vol. 18, pp. 1489-1499, 1980.

Dibble, R.W., Kollmann, W. and Schefer, R.W., “Measurements and predictions of scalar dissipation in turbulent jet flames”, *Proc. Combust. Inst.*, Vol. 20, pp. 345-352, 1984.

Dibble, R.W., Masri, A.R. and Bilger, R.W., “The Spontaneous Raman Scattering Technique Applied to Nonpremixed Flames of Methane”, *Combust. Flame* Vol. 67, pp. 189-198, 1987.

Dimotakis, P.E., “The mixing transition in turbulent flows”, *J. Fluid Mech.*, Vol. 409, pp. 69-98, 2000.

Dowling, D.R., “The estimated scalar dissipation rate in gas-phase turbulent jets”, *Phys. Fluids A*, Vol. 3, pp 2229-2246, 1991; Erratum in *Phys. Fluids A*, Vol. 4, pp 453, 1992.

Dowling, D.R. and Dimotakis, P.E., “Similarity of the concentration field of gas-phase turbulent jets”, *J. Fluid Mech.*, Vol. 218, pp. 109-141, 1990.

Effelsberg, E. and Peters, N., “Scalar Dissipation rates in Turbulent Jets and Jet Diffusion Flames”, *Proc. Combust. Inst.*, Vol. 22, pp. 693-700, 1988.

Everest, D.A., Driscoll, J.F., Dahm, W.J.A. and Feikema, D.A., “Images of the Temperature Field and temperature Gradients to Quantify Mixing Rates within a Non-Premixed Turbulent Flame”, *Combust. Flame*, Vol. 101, pp. 58-68, 1995.

Ferrao, P., Heitor, M.V. and Salle, R., "On the Accuracy of Scalar Dissipation Measurements by Laser Rayleigh Scattering", 10th International Symposium on Turbulence, Heat and Mass Transfer, Lisbon, Portugal, 2000.

Fielding, J., Schaffer, A.M. and Long, M.B., "Three-Scalar Imaging in Turbulent Non-premixed Flames of Methane", *Proc. Combust. Inst.*, Vol. 27, pp.1007-1014, 1998.

Fielding, J., Frank, J.H., Kaiser, S.A., Smooke, M.D. and Long, M.B, "Polarized/Depolarizad Rayleigh Scattering for Determining Fuel Concentrations in Flames", *Proc. Combust. Inst.*, Vol. 29, pp. 2703-2709, 2002.

Fourguette, D.C., Zurn, R.M. and Long, M.B., "Two-Dimensional Rayleigh Thermometry in a Turbulent Nonpremixed Methane-Hydrogen Flame", *Combst. Sci. and Tech.*, Vol. 44, pp. 307-317, 1986.

Frank, J.H., Kaiser, S.A. and Long, M.B., "Reaction-Rate, Mixture-Fraction, and Temperature Imaging in Turbulent Methane/Air Jet Flames", *Proc. Combust. Inst.*, Vol. 29, pp.2687-2694, 2002.

Friehe, C.A., Van Atta, C.W. and Gibson, C.H., "Jet turbulence: dissipation rate measurements and correlations", NATO Advisory Group for Aerospace Research and Development, Paper AGARD-CP-93, 1971.

Gaskey, S., Vacus, P., David, R., Villermaux, J. and Andre, J. C., "A Method for the Study of Turbulent Mixing Using Fluorescence Spectroscopy", *Exp. Fluids*, Vol. 9, pp. 137–147, 1990.

Geyer, D., Kempf, A., Dreizler, A. and Janicka, J., "Scalar Dissipation Rates in Isothermal and Reactive Turbulent Opposed-Jets: 1D-Raman/Rayleigh Experiments Supported by LES", *Proc. Comb. Inst.*, Vol. 30, to be published, 2004.

Geyer, D., "Noise effect on the scalar dissipation", 7th International Workshop on Measurement and Computation of Turbulent Nonpremixed Flames, Chicago, IL, July 22-24, 2004.

Gladnick, P.G., LaRue, J.C. and Samuelsen, G.S., "Anisotropy in the Near-Field of a Turbulent Diffusion Flame", in *Heat Transfer in Combustion Systems* (eds. B. Farouk, W.L. Grosshandler, D.G. Lilly and C. Presser) HTD vol. 142, pp. 33-40, ASME, New York, 1990.

Gurvich, A.S. and Yaglom, A.M., "Breakdown of Eddies and Probability Distributions for Small-Scale Turbulence", *Phys. Fluids* 10 (Suppl.) pt. II, S59-S65, 1967.

Kaiser, S.A., Long, M.B. and Frank, J.H., "Multi-Scalar Imaging in Argon-Diluted Jet Flames", 7th International Workshop on Measurement and Computation of Turbulent Nonpremixed Flames, Chicago, IL, July 22-24, 2004.

Karpetis, A.N. and Barlow, R.S., "Measurements of Scalar Dissipation in a turbulent Piloted Methane/Air Jet Flame", *Proc. Combust. Inst.*, Vol. 29, pp.1929-1936, 2002.

Kelman, J.B. and Masri, A.R., "Quantitative technique for imaging mixture fraction, temperature, and the hydroxyl radical in turbulent diffusion flames", *App. Optics*, Vol. 36, pp. 3506-3514, 1997.

Libby, P.A., "Introduction to turbulence", Washington, D.C.: Taylor & Francis, 1996

Lockwood, F.C. and Moneib, H.A., "Fluctuating Temperature Measurements in a Heated Round Free Jet", *Combst. Sci. and Tech.*, Vol. 22, pp. 63-81, 1980.

Masri, A.R., Dibble, R.W. and Barlow, R.S., "The structure of turbulent nonpremixed flames revealed by Raman-Rayleigh-LIF measurements", *Prog. Energy Combust. Sci.*, Vol. 22, pp. 307-362, 1996.

Meier, W., Barlow, R.S., Chen, Y.-L., and Chen, J.-Y., "Raman/Rayleigh/LIF Measurements in a Turbulent CH4/H2/N2 Jet Diffusion Flame: Experimental Techniques and Turbulence-Chemistry Interaction", *Combust. Flame*, Vol. 123, pp. 326-343, 2000.

Mi, J. and Antonia, R.A., "Corrections to Taylor's hypothesis in a turbulent circular jet", *Phy. Fluids A*, Vol. 6, No. 4, pp. 1548-1552, 1994a.

Mi, J. and Antonia, R.A., "Some Checks of Taylor's Hypothesis in a Slightly Heated Turbulent Circular Jet", *Exp. Thermal Fluid Sci.*, Vol. 8, pp. 328-335, 1994b.

Mi, J. and Nathan, G.J., "The influence of probe resolution on the measurement of a passive scalar and its derivatives", *Exp. Fluids*, Vol. 34, pp. 687-696, 2003.

Miles, R.B., Lempert, W.R. and Forkey, J.N., “Laser Rayleigh scattering”, *Meas. Sci. Technol.*, Vol. 12, pp. R33-R51, 2001

Miller, P.L. and Dimotakis, P.E., “Reynolds number dependence of scalar fluctuations in a high Schmidt number turbulent jet”, *Phys. Fluids A*, Vol. 3, pp. 1156–1163, 1991.

Miller, P.L. and Dimotakis, P.E., “Measurements of Scalar Power Spectra in High Schmidt Number Turbulent Jets”, *J. Fluid Mech.*, Vol. 308, pp.129-146, 1996.

Molina, R., Nunez, J., Cortijo, F.J. and Mateos, J., “Image Restoration in Astronomy: A Bayesian Perspective”, *IEEE Signal Processing Magazine*, Vol. 18, No. 2, pp.11-29, 2001.

Muniz, L. and Mungal, M.G., “Effects of Heat Release and Buoyance on Flow Structure and Entrainment in Turbulent Nonpremixed Flames”, *Combust. Flame*, Vol. 126, pp. 1402-1420, 2001.

Namazian, M, Scheffer, R.W. and Kelly, J., “Scalar Dissipation Measurements in the Developing Region of a Jet”, *Combust. Flame*, Vol. 74, pp. 147-160, 1988.

Nandula, S.P., Brown, T.M. and Pitz, R.W. “Measurements of Scalar Dissipation in The Reaction Zones of Turbulent Nonpremixed H2 Air Flames”, *Combust. Flame*, Vol. 99, 775-783, 1994.

Oppenheim, A.V., Schafer, R.W., and Buck, J.R., “Discrete-time signal processing”, 2nd Edition, Upper Saddle River, N.J.: Prentice Hall, 1999.

Peters, N. and Donnerhack, S., “Structure and Similarity of Nitric Oxide Production in Turbulent Diffusion Flames”, *Proc. Comb. Inst.*, Vol. 18, pp. 33-42, 1981.

Peters, N. and Williams, F.A., “Liftoff Characteristics of Turbulent Diffusion”, *AIAA J.*, Vol. 21, No. 3, pp. 423-429, 1983.

Peters, N., “Laminar Diffusion Flamelet Models in Non-Premixed Turbulent Combustion”, *Prog. Energy Combust. Sci.*, Vol. 10, pp. 319-339, 1984.

Peters, N., and GÖtgens, J., “Scaling of Buoyant Turbulent Jet Diffusion Flames,” *Combust. Flame*, Vol. 85, pp. 206-214, 1991.

Peters, N., “Turbulent Combustion”, New York: Cambridge University Press, 2000.

Pitts, W. M., “Resolution Requirements for Scalar Dissipation Measurements in Turbulent Jets and Flames”, Third International Workshop on Measurement and Computation of Turbulent Nonpremixed Flames, Boulder, 1998.

Pitts, W.M., Richards, C.D., and Levenson, M. S., “Large- and small-scale structures and their interactions in an axisymmetric jet”, NIST Report NISTIR-639, 1999.

Pope, S.B., “Turbulent Flows”, Cambridge University Press, New York, 2000.

Renfro, M. W., King, G. B., and Laurendeau, N. M., “Quantitative hydroxyl-concentration time-series measurements in turbulent nonpremixed flames”, *App. Opt.*, Vol. 38, pp. 4596-4608, 1999.

Renfro, M.W., Gore, J.P., King, G.B., and Laurendeau, N.M., “Self-similarity of measured hydroxyl concentration temporal statistics in turbulent nonpremixed jet flames”, *AIAA J.*, Vol. 38, pp. 1230-1236, 2000.

Raguraman, J., King, G.B., Laurendeau, N.M. and Renfro, M.W., “Hydroxyl and Rayleigh Scattering Time-Series Measurements in Turbulent Non-premixed H2/CH4/N2-Air Jet Flames”, *Proceedings of the 2004 Spring Technical Meeting of the Central States Section of The Combustion Institute*, Austin, TX, 2004.

Schneider, Ch., Dreizler, A., Janicka, J. and Hassel, E.P., “Flow field measurements of stable and locally extinguishing hydrocarbon-fuelled jet flames”, *Combust. Flame*, Vol. 135, pp. 185-190, 2003.

Smith, W.J., “Modern Optical Engineering”, New York : McGraw-Hill, 2000.

Stårner, S.H., Bilger, R.W., Long, M.B., Frank, J.H. and Marran, D.F., “Scalar Dissipation Measurements in Turbulent Jet Diffusion Flames of Air Diluted Methane and Hydrogen”, *Combust. Sci. Tech.*, Vol. 129, pp.141-163, 1997.

Stricker, W.P., “Measurement of temperature in Laboratory Flames and Practical Devices”, in *Applied Combustion Diagnostics*, Editor Kohse-Höinghaus, K. and Jeffries, J., Taylor and Francis: 2002.

Su, L.K., and Clemens, N.T., "Planar measurements of the full three-dimensional scalar dissipation rate in gas-phase turbulent flows", *Exp. Fluids*, Vol. 27, No. 2, pp. 507-521, 1999.

Su, L.K., and Clemens, N.T., "The Structure of Fine-Scale Scalar Mixing in Gas-Phase Planar Turbulent Jets", *J. Fluid Mech.*, Vol. 488, pp. 1-29, 2003.

Sutton, J.A. and Driscoll J.F., "Scalar Dissipation Rate Measurements in Flames: A Method to Improve Spatial Resolution by Using Nitric Oxide PLIF", *Proc. Combust. Inst.*, Vol. 29, pp.2727-2734, 2002.

Tacina, K.M. and Dahm, W.J.A., "Effects of heat release on turbulent shear flows. Part 1: A general equivalence principle for nonbuoyant flows and its application to turbulent jet flames", *J. Fluid Mech.*, Vol. 415, pp. 23-44, 2000.

Tennekes, H. and Lumley J.L., "A first course in turbulence", MIT Press, Cambridge, MA, 1972.

Vervisch, L. and Poinsot, T., "Direct Numerical Simulation of Non-Premixed Turbulent Flames", *Annu. Rev. Fluid Mech.*, Vol. 30, pp. 655-691, 1998.

Tsurikov, M. S., "Experimental investigation of the fine scale structure in turbulent gas-phase jet flows", Ph.D dissertation, The University of Texas at Austin, 2002.

Wang, G.H. and Clemens, N.T., "Effects of Imaging System Blur on Measurements of Flow Scalars and Scalar-Gradients", *Exp Fluids*, Vol. 37, No. 2, pp. 194-205, 2004.

Wang, G.H., Clemens, N.T. and Philip, P.L., "High-Repetition Rate Measurements of Temperature and Thermal Dissipation in a Nonpremixed Turbulent Jet Flame", *Proc. Comb. Inst.*, Vol. 30, to be published, 2004.

Williams, F.A., "The role of theory in combustion science", *Proc. Combust. Inst.*, Vol. 24, pp.1-17, 1992.

Wygnanski, I., and Fielder, H., "Some measurements in the self-preserving jet", *J. Fluid Mech.*, Vol. 38, pp.577-612, 1969.

Wyngaard, J.C., "Measurement of small-scale turbulence structure with hot wires", *J. Sci. Instrum.*, Vol.1, pp.1105-1108, 1968.

Wyngaard, J.C. ,“Spatial resolution of the vorticity meter and other hot-wire arrays”, *J. Sci. Instrum.*, Vol.2, pp.983-987, 1969.

Wyngaard, J.C., “Spatial resolution of a resistance wire temperature sensor”, *Phys. Fluids*, Vol.14, pp.2052-2054, 1971.

Yariv, A., “Optical Electronics”, 4th Edition, Philadelphia: Saunders College Pub., 1991.

Zhao F-Q and Hiroyasu, H., “The applications of laser Rayleigh scattering to combustion diagnostics”, *Prog. Energy Combust. Sci.*, Vol. 19, pp. 447-85, 1993.

Vita

Guanghua Wang was born on May 2, 1972, in DanDong, LiaoNiong, P.R. China. In September 1991, he enrolled at Beijing University of Aeronautic and Astronautics (BUAA, BeiHang University now), Beijing, P.R. China, with a major in jet propulsion. He earned the degree of Bachelor of Science from BUAA in July 1995, graduating with excellent student award. In September 1995 he entered the Graduate School of the Beijing University of Aeronautic and Astronautics, Beijing, P.R. China, with a major in jet propulsion. He earned the degree of Master of Science from BUAA in March 1998, graduating with excellent thesis award. In April 1998 he joined Beijing Aircraft Maintenance and Engineering Co. (AMECO Beijing) as a test cell engineer. He was trained for testing, performance analyzing and trouble shooting of major airline jet engines. In January 2000 he entered the graduate school of the University of Texas at Austin with a major in aerospace engineering.

Permanent address: ShanXia Jie, ZhenXing Qu, DanDong, LiaoNing,
P.R. China, 118000

This dissertation was typed by the author.